Dissertation

submitted to the
Combined Faculties for the Natural Sciences
and for Mathematics
of the Ruprecht Karl University of Heidelberg, Germany
for the degree of
Doctor of Natural Sciences

Put forward by

Philip Maurice Trapp

Born in: Gießen, Germany

Oral examination: 19.07.2022

Novel Methods for the Reduction of Systematic and Statistical Measurement Deviations and Spatial Resolution Optimization in X-Ray Computed Tomography

Referees: Prof. Dr. Peter Bachert

Prof. Dr. Marc Kachelrieß

Novel Methods for the Reduction of Systematic and Statistical Measurement Deviations and Spatial Resolution Optimization in X-Ray Computed Tomography

Systematic and statistical measurement deviations, as well as insufficient spatial resolution of the image data, can severely degrade the image quality in x-ray computed tomography (CT) and thus limit the application of CT for medical and industrial purposes. This dissertation therefore deals with the reduction of such measurement deviations under the aspect of simultaneously optimal spatial resolution of the CT datasets. The empirical scatter correction (ESC) is presented as an algorithm that effectively reduces systematic measurement deviations due to scattered photons without specific prior knowledge about the measured object, the CT system, or acquisition parameters. Furthermore, this work proposes the frequency split dual energy computed tomography (FSDECT), a method for CT systems with two x-ray tubes that reduces systematic measurement deviations due to the polychromatic x-ray spectrum and the energy-dependent attenuation behavior of matter. Compared to existing dual energy computed tomography (DECT) methods for reducing systematic measurement deviations, the resulting fusion volume dataset has an increased spatial resolution. The feasibility of reducing systematic measurement deviations in CT using novel energy-selective detectors is also reviewed in this work and possible benefits compared to non-energy-selective detectors are discussed. To reduce statistical measurement deviations, which negatively affect the reproducibility of measurement results in addition to a decrease of image quality, a guided bilateral filter is proposed. By improving the image quality with the correction methods presented in this dissertation, internal features of a sample workpiece can be measured with high repeatability using CT measurements, which is not possible without these methods due to excessive measurement deviations.

Neue Verfahren zur Reduktion systematischer und statistischer Messabweichungen und räumlichen Auflösungsoptimierung in der Röntgencomputertomographie

Systematische und statistische Messabweichungen sowie eine unzureichende räumliche Auflösung der Bilddaten können die Bildqualität in der Röntgencomputertomographie (CT) stark reduzieren und somit die Anwendung für medizinische und industrielle Zwecke einschränken. Diese Dissertation behandelt deshalb die Reduktion derartiger Messabweichungen unter dem Gesichtspunkt gleichzeitig optimaler räumlicher Auflösung der CT-Datensätze. Mit der empirischen Streustrahlkorrektur (ESC) wird ein Algorithmus präsentiert, der ohne spezifisches Vorwissen über das Messobjekt, das CT-System, oder Aufnahmeparameter, systematische Messabweichungen durch gestreute Photonen effektiv reduziert. Darüber hinaus wird in dieser Arbeit mit der frequenzteilenden Zweispektren-CT (FSDECT) ein Verfahren für CT-Systeme mit zwei Röntgenröhren vorgestellt, welches systematische Messabweichungen aufgrund des polychromatischen Röntgenspektrums und des nicht-linearen Abschwächungsverhaltens von Materie reduziert. Verglichen mit bestehenden Zweispektren-CT-Verfahren zur Reduktion systematischer Abweichungen hat der so gewonnene Fusionsvolumendatensatz eine erhöhte räumliche Auflösung. Im Rahmen dieser Arbeit wird außerdem die Möglichkeit zur Reduktion systematischer Messabweichungen in der CT mittels neuartiger energieselektiver Detektoren überprüft und mögliche Vorteile gegenüber nicht-energieselektiven Detektoren erörtert. Zur Reduktion von statistischen Messabweichungen, die neben der Bildqualität die Reproduzierbarkeit von Messergebnissen negativ beeinflussen, wird das Verfahren des gesteuerten Bilateralfilters vorgeschlagen. Durch die Erhöhung der Bildqualität mit den in dieser Dissertation vorgestellten Korrekturverfahren können innenliegende Merkmale eines Testwerkstückes mit hoher Wiederholpräzision mittels CT gemessen werden, was ohne diese Verfahren aufgrund zu starker Messabweichungen nicht möglich ist.

Contents

List of Acronyms

AM . . . . . Artifact mask

ASGs . . . . . Antiscatter grids

BF . . . . . Bilateral filter

CBCT . . . . . Cone-beam computed tomography

CNR . . . . . Contrast-to-noise-ratio

CT . . . . . Computed tomography

DECT . . . . . Dual energy computed tomography

EI . . . . . Energy-integrating

EID . . . . . Energy-integrating detector

EPDL . . . . . Evaluated photon data library

ESC . . . . . Empirical scatter correction

ESF . . . . . Edge spread function

FBP . . . . . Filtered backprojection

FDK . . . . . Feldkamp Davis Kress

FOM . . . . . Field of measurement

FSDECT . . . . . Frequency split dual energy computed tomography

FWHM . . . . . Full width at half maximum

gBF . . . . . Guided bilateral filter

HF . . . . . Homogeneity factor

HU . . . . . Hounsfield units

ibESC . . . . . Image-based empirical scatter correction

LSF . . . . . Line spread function

MAE . . . . . Mean absolute error

MSCT . . . . . Multislice computed tomography

MSE . . . . . Mean squared error

MTF . . . . . Modulation transfer function

PBT . . . . . Polybutylenterephthalat

PC . . . . . Photon-counting

PCCT . . . . . Photon-counting computed tomography

PCD . . . . . Photon-counting detector

PSF . . . . . Point spread function

ROI . . . . . Region of interest

SNR . . . . . Signal-to-noise-ratio

SPR . . . . . Scatter-to-primary-ratio

SRDM . . . . . Semirealistic detector model

STL . . . . . Stereolithography

TEPs . . . . . Total endoprostheses

UHR . . . . . Ultra high resolution

List of Figures

List of Tables

1 Introduction

When Wilhelm Conrad Röntgen discovered a new type of electromagnetic radiation in 1895, which is absorbed by matter to different extents depending on material, density and transmission length and which he called x-rays [1], the scientific community immediately realized the significance of this discovery and, in particular, its usefulness for medical applications, so that Röntgen was awarded the first Nobel Prize in Physics in 1901. Sixteen years later, the Austrian mathematician Johann Radon published a method for solving the inverse problem of reconstructing a function from its line integrals [2], which corresponds approximately to the problem of reconstructing volume information from x-ray projections of different acquisition angles. This laid the theoretical foundation for x-ray CT, which describes a method for computing local attenuation information in a body from x-ray images taken from different directions. However, since numerous computational operations must be performed for the reconstruction of CT volume data, requiring a computer for efficient computation, it took further decades until the technical realization of a commercially available CT device, which was first developed in 1972 by Sir Godfrey Hounsfield and distributed by the company Electric and Musical Industries (EMI). Together with Allan McLeod Cormack, who provided theoretical foundations for CT, Hounsfield was awarded the Nobel Prize in Physiology or Medicine in 1979. Unsurprisingly, x-ray CT quickly established itself as one of the most important imaging modalities in radiology, where it still plays a very important role today due to its quantitative imaging of the interior of the body, as well as short acquisition times and very high detail resolutions. In 2018, for example, 145 CT exams were performed per 1000 inhabitants in Germany alone [3].

The potential of x-ray computed tomography for nondestructive evaluation of workpieces was recognized as early as the early 1980s [4]–[6] and CT thus made its way into quality assurance processes for workpiece inspection and flaw detection. In particular, the emergence of x-ray flat panel detectors in the late 1990s [7], which together with specialized reconstruction algorithms [8] allow a much larger measurement volume, led to an increase in the use of CT in industrial applications. Then, in 2005, the first commercially available coordinate measuring machine with computed tomography sensor [6], [9] was released. Due to a fully calibrated measuring volume, dimensions of scanned workpieces can be determined in this CT application and thus the manufacturing quality of the workpiece can be checked within certain tolerances. An advantage of the CT sensor compared to tactile or optical sensors is the high number of features that can simultaneously be recorded by CT [10] and the possibility to non-destructively deter-

mine also internal and thus difficult accessible dimensions. Therefore, the metrological application of CT is already an established method for quality assurance, especially in the plastic injection molding industry, the automotive industry, as well as the medical engineering sector and consumer goods industries, and it is expected that the market share of coordinate measuring machines with CT sensor will continue to grow [11].

A major problem in CT are systematic measurement deviations, which are called artifacts in CT and which have a strong negative influence on the image quality (cf. Fig. 1.1) and thus make diagnoses using medical CT data or inspections using industrial CT data difficult or completely impossible. Moreover, these measurement deviations are known to distort the dimensions of workpiece features determined by CT measurements [12]–[14]. Artifacts arise in CT volume data when the linear relationship between measured projection values and intersection lengths of the measured object, which is required by typical analytical reconstruction methods, is undermined by physical effects in the CT measurement, or sampling criteria are not met, or the solution space of the used reconstruction algorithm is ambiguous [15], [16]. The mentioned physical effects correspond to systematic measurement deviations caused by the polychromatic x-ray spectrum, scattered radiation, signal height differences of the detector pixels, or complete absorption of the x-ray radiation (photon starvation), just to name a few. A good overview of artifacts in CT is provided by reference [17]. A large part of these systematic measurement deviations occurs increasingly for measured objects that strongly absorb x-rays. This is the case for dense matter with high atomic number, which is why artifacts are especially pronounced for measurements of metal objects, or objects containing metals. In medical applications, this can be the case, for example, in CT measurements of patients with metallic implants. Accordingly, established solution approaches for such systematic measurement deviations exist in medical imaging [18]–[20]. However, these methods reach their limits when the proportion of metals in the measured object is very high and are therefore of limited use in industrial CT applications [21], where metals may make up a large part or even the entire workpiece.

A commonly used option in industrial CT to measure substantial objects that are difficult to penetrate with x-rays is to use high photon energies for the measurement. This is advantageous, as it may lead to an increased transmission of x-rays and can lead to a reduction of systematic measurement deviations (see Fig. 1.1). However, this method is associated with the problem that x-ray tubes, which allow correspondingly high photon energies, are often operated with large focal spot sizes in order to be able to effectively transport any heat generated away from the target and prevent damage to the CT system. Thus, this negatively affects another feature of image quality, namely the structural resolution of the volume data obtained by the CT measurement, which is evident in the close-ups of Fig. 1.1. This may be an exclusion criterion for applications with strict structural resolution or tolerance requirements.

Existing correction methods for systematic measurement deviations in industrial CT applications can basically be divided into hardware-based methods [22]–[24], where modifications are made to the CT device or individual components, and software-based methods, which in turn can be divided into iterative methods [25], [26] and pre- and postcorrection methods [21], [27]–[33], depending on whether the correction is iteratively

incorporated into the CT reconstruction process or is applied before or after the CT reconstruction on the acquired datasets. One problem in industrial CT is often a lack of prior knowledge about the workpiece under investigation or the measuring system. In contrast to medical CT applications, in which the measurement object is always the human body, the material composition of workpieces is often not known a priori, especially if the CT quality assurance process is not integrated into the production of the workpiece. In addition, industrial CT devices often differ greatly from each other depending on the target application, and the characteristics of individual components, some of which are not manufactured by the CT manufacturer itself, such as x-ray tubes or detectors, are not fully known, which makes it difficult to use a correction procedure that requires precise prior knowledge of the measurement system. The scan trajectories and acquisition parameters may strongly differ in industrial CT, as well, and there are usually no fixed scan protocols, such as they are implemented for clinical CT systems.

For the correction of scatter artifacts, methods like Monte Carlo simulations or linear Boltzmann transport equation solvers, which try to exactly reproduce the physical process of photon scattering, are considered to be the gold standard [34]–[40] besides novel learning-based methods, which require a sufficiently trained neural network as a basis [27], [41]–[51]. Monte Carlo and Boltzman transport equation methods strongly rely on prior knowledge of the scanned object, such as material and density distribution, as well as the measurement system and acquisition parameters for accurate correction results [52], however. Therefore, after discussing the fundamental working principle of CT and the theoretical background of some of the main characteristics of CT in chapter 2, a novel method is presented that can reduce systematic measurement deviations due to scattered photons without specific prior knowledge about the measured object, the measurement system, or the acquisition parameters in chapter 3 of this thesis. The method presented here corresponds to a software-based precorrection method that incorporates an iterative optimization scheme and it reduces scatter artifacts based on measured projection data and a reconstruction algorithm alone, without prior knowledge, reference measurements, training data, or hardware modifications that typically increase measurement effort and can even lead to reduced image quality under unfavorable measurement conditions [53]–[56].

In chapter 4 of this thesis a novel method for the reduction of systematic measurement deviations due to the polychromatic x-ray spectrum is presented. This method is based on the fusion of CT datasets acquired with two x-ray tubes of different designs, which differ both in the size of the focal spot, i.e., their achievable maximum spatial resolution, and in the maximum tube voltage and tube power, i.e., their achievable penetration and artifact content of the CT datasets. The principle of using CT datasets acquired with different x-ray spectra to reduce beam hardening and metal artifacts has been known and is well studied in clinical CT for some time [57]–[59]. However, combining the advantages of different x-ray tube designs in a single process is a novelty. The goal of the data fusion presented in chapter 4 is therefore to generate a fusion CT data set with reduced scatter and beam hardening artifacts without having to accept the loss of spatial resolution typical for high power x-ray tubes with large focal spots (cf. Fig. 1.1).

Novel energy-resolving detectors allow the acquisition of spectral datasets for a single

CT scan of an object using the same x-ray tube parameters and prefiltration [20], [60]–[62]. Chapter 5 of this dissertation examines, if spectral data using an energy resolving detector instead of different tube spectra can reduce the amount of systematic measurement deviations in a CT measurement, as well, and discusses potential benefits compared to conventional dual energy CT approaches.

As some of the aforementioned methods for the reduction of systematic measurement deviations may lead to an increase of statistical measurement deviations, this issue is addressed in chapter 6 of this dissertation. In this chapter, a novel method is discussed that uses CT datasets with different properties in terms of artifact content and noise levels, e.g. different combinations of spectral CT datasets, to produce an artifact-reduced low-noise CT volume by a guided filter operation. The guidance in this filtering process by means of another aligned CT volume of the measured object with favourable noise characteristics thereby guarantees that edges, hence the structural resolution, are preserved. Compared to existing edge-preserving filter-based noise reduction methods [63]–[68], the method proposed here is optimized, but not limited, for the use case on artifact-reduced spectral CT data combinations, which is demonstrated using spectral CT data acquired with an energy resolving detector and spectral CT data acquired with different x-ray tubes at different x-ray spectra.

Even though the focus of this thesis is to increase the image quality of industrial CT measurements, the transfer to medical applicability is often not far, as will be shown in the individual chapters of this thesis.

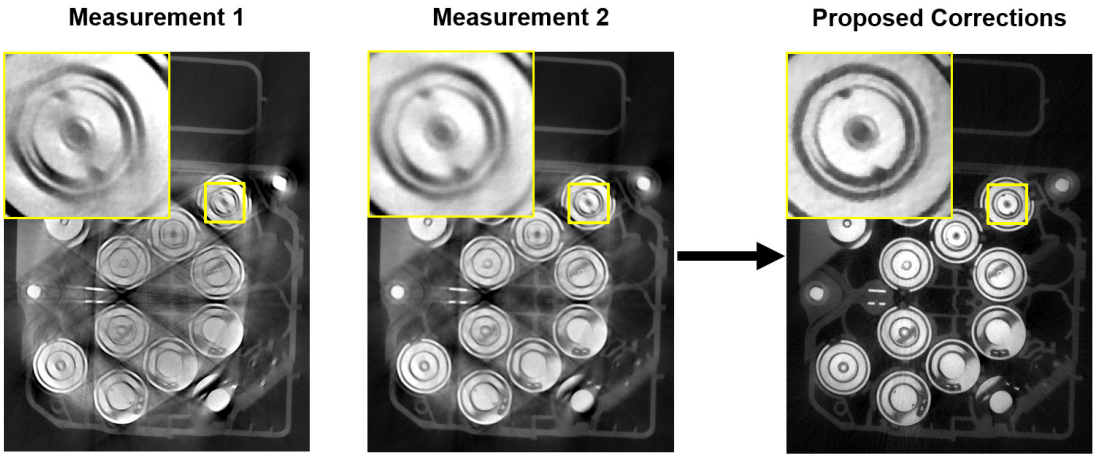

Figure 1.1: CT images for two measurements of an automotive control device and for a corrected dataset. While the dataset on the left corresponds to a measurement using an x-ray tube with a small focal spot and moderate photon energies, the dataset in the middle corresponds to a measurement using an x-ray tube with a large focal spot and high photon energies. Both datasets exhibit a high amount of systematic measurement deviations with measurement one showing even higher deviations. The dataset shown on the right, which was corrected with the algorithms proposed in this dissertation that partially use information of both measurements, shows a reduced amount of systematic measurement deviations. The close-ups furthermore emphasize the different spatial resolution of the datasets. The corrected data have a spatial resolution that is comparable to that of the initial dataset with the higher spatial resolution (measurement one).

2 Fundamentals

2.1 X-Ray Imaging and X-Ray Computed Tomography

X-ray computed tomography is based on the idea of taking radiographs under different angles of view and transferring the obtained information numerically into a three-dimensional volume dataset. The setup of a typical industrial cone-beam computed tomography (CBCT) system is depicted in Fig. 2.1. The procedure of a CT measurement begins with the generation of x-rays in the x-ray tube. Subsequently, the generated x-ray photons pass through matter (prefilter and object) and impinge on the x-ray detector, which typically consists of numerous detector elements, so-called detector pixels in lateral and longitudinal direction. Radiographs are then taken at different rotation angles α. Devices such as the one shown in Fig. 2.1, where x-rays are emitted and detected in a pyramid shape, are referred to as cone-beam CTs. Basically, the geometry of such a CBCT system is unambiguously defined by the vectors $\boldsymbol{s}(\alpha)$, $\boldsymbol{o}(\alpha)$, $\boldsymbol{u}(\alpha)$, and $\boldsymbol{v}(\alpha)$ for each rotation angle α. Whilst $\boldsymbol{s}(\alpha)$ points from the origin of coordinates, which typically corresponds to the isocenter of rotation, to the position of the focal spot of the x-ray tube, $\boldsymbol{o}(\alpha)$ points to the center of the first detector pixel. The vectors $\boldsymbol{u}(\alpha)$ and $\boldsymbol{v}(\alpha)$ have the same magnitude as the pixel dimension in lateral and longitudinal direction and define the detector plane. In highly accurate industrial CBCT systems, the object is usually rotated on a rotary table to obtain radiographs at different angles α instead of a physical movement of the x-ray tube and the detector. This is done because the distance of the object to the focal spot and the detector, which determines the optical magnification (cf. Sec. 2.2), can easily be adjusted by moving the rotary stage towards or away from the x-ray tube and the typically lead shielded CBCT device can be designed relatively compact. Thus, the rotation of the souv-vectors is performed virtually by an object rotation in these setups. In medical CBCT systems, such as those used for image-guided radiotherapy or interventional CT, the x-ray tube and the detector are in fact rotated around the patient, who is placed in the isocenter of this rotation. For ideal circle scan trajectories, the focus-detector distance R_{FD}, the focus-isocenter distance R_{F}, and the isocenter-detector distance R_{D} stay constant throughout the entire rotary movement. Clinical diagnostic CT devices show more differences to the setup in Fig. 2.1. Similar to medical CBCT devices, the x-ray tube and detector rotate around the patient. This rotation operates at very high velocities, however, and the ring tunnel in which the tube and detector rotate is called the gantry

in these CTs. Instead of flat detectors, diagnostic CTs use detectors which are curved around the focal spot of the x-ray tube with a comparatively small longitudinal coverage. However, even these curved detectors nowadays consist of multiple detector rows of up to 320 detector pixels [69], which is why modern diagnostic CT systems are also referred to as multislice computed tomography (MSCT). When short scan times are required instead of high measurement accuracies and adjustable magnification settings, computer tomographs with gantry-based designs are also used in industrial applications [70].

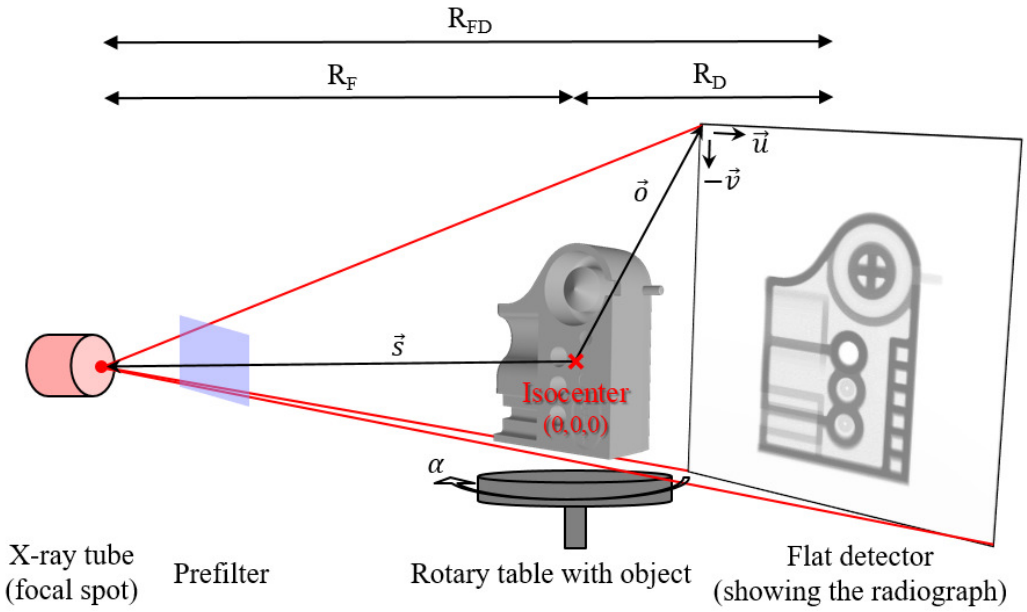

Figure 2.1: Setup of a typical industrial CBCT scanner. X-rays are generated at the focal spot in the x-ray tube and pass through matter in the form of a prefilter and the scanned object before being converted into an electrical signal at the detector, which results in an x-ray image of the object. The geometry of the CT is defined by the ***souv*** -vectors. The rotary table rotates the object around the isocenter of rotation by the angle α.

Following the logical flow of a CT measurement from the generation of the x-ray radiation to the volume reconstruction and the generation of the measurement point cloud, the technical components of a CT, the associated physical effects of a CT measurement, and specific algorithms for CT rawdata processing are explained in the following.

2.1.1 Generation of X-Rays

By definition, x-rays describe electromagnetic radiation with wavelengths of about 10^{-8} m to 10^{-12} m [71] (about 100 eV to 1 MeV) produced by the interaction of fast

charged particles, usually electrons, with matter. As shown in Fig. 2.1, in conventional CT scanners x-rays are generated in x-ray tubes. The basic working principle is the same for all common types of x-ray tubes since the discovery of x-rays at the end of the 19th century. A cathode, usually made of thoriated tungsten with a high melting point at roughly 3683 K, is heated to approximately 2400 K [16] in order to release electrons by thermionic emission. The electrons thus released are accelerated in an electric field generated by applying a voltage between the cathode and an anode, the so-called tube voltage U_B. Due to this acceleration, the electrons acquire the kinetic energy $E_\mathrm{kin} = e\,U_\mathrm{B}$, where $e = 1.602176634 \cdot 10^{-19}\,\mathrm{C}$ corresponds to the elementary charge. When these electrons hit a target, they will lose their kinetic energy and this energy loss results in the release of electromagnetic radiation, the x-rays, for energy conservation reasons. Such x-rays can be generated by two different physical processes, and depending on the process of generation, one speaks of characteristic x-rays or bremsstrahlung.

Characteristic x-rays are caused by inelastic Coulomb interactions between the accelerated free electrons and the bound electrons of the target material atoms. The collision process transfers energy from the free electron to the bound electron and thereby ionizes the atom. The vacancy in the electron orbital is then filled with a weaker bound electron from the atom and a photon with a discrete energy equal to the difference in the binding energies of the involved energetic states is released. Relating to the electron shell model, the released x-ray photons are labeled with the letters of the ionized shell (K, L, M, etc.) and a Greek index encodes the filling of this electron hole by an electron from the neighboring shell (α), the shell after next (β), and so on. Thus, a K_α photon results, for example, from an ionization of a K-shell electron and a transition of an L-shell electron to the resulting vacancy in the K-shell, while a K_β photon is produced by the refilling of the K-shell vacancy with an electron from the M-shell.

Bremsstrahlung, on the other hand, describes the process of x-ray generation by deflection of the free high-energy electrons in the electric field of the nucleus of a target material atom. Following the law of conservation of energy, the associated loss of energy by this deflection is compensated by the emission of photons. In contrast to characteristic x-rays, the x-rays generated by bremsstrahlung processes have continuous energies and the maximum energy obtained by this process is given when the whole kinetic energy of an electron is transferred into a single x-ray photon:

$$E_{\gamma,\mathrm{max}} = E_\mathrm{kin} = e\,U_\mathrm{B} \tag{2.1}$$

Characteristic x-rays and bremsstrahlung are always found superimposed in the x-ray spectrum of an x-ray tube. Even though the fraction of characteristic x-rays increases for increasing tube voltages, the fraction is still as low as 10% for a relatively high tube voltage of $U_\mathrm{B} = 250\,\mathrm{kV}$ given a target material of tungsten [72] and the continuous bremsstrahlung typically dominates the x-ray spectrum (cf. Fig. 2.3). According to Kramers' law [73], the intensity distribution of the bremsstrahlung in photons per

second can be approximated by [74]

$$N(E) \propto I_e \, Z \left(\frac{E_{\gamma,\max}}{E} - 1 \right), \tag{2.2}$$

where I_e denotes the electron current in electrons per second and Z the atomic number of the target material. The electron current in SI units corresponds to the so-called tube current I of the x-ray tube. Following the above equation, the intensity distribution of the generated x-ray bremsstrahlung is hence approximately proportional to the tube current I, the atomic number Z of the target material and the tube voltage U_B, which implicitly controls $E_{\gamma,\max}$ following Eq. (2.1). The efficiency for converting the kinetic energy of electrons into x-ray photons is proportional to the atomic number Z and tube voltage U_B, as well, and is only about 1% [75]. The remaining energy is converted to heat. Therefore, the target material must be very heat resistant. This is why tungsten is often used as target material, since it has a high melting point at 3695 K [76] combined with a relatively high atomic number of $Z = 74$.

Besides the intensity of the x-ray radiation and the maximum energy of the emitted photons, the size of the focal spot plays a major role in x-ray imaging because it corresponds to one of the limiting factors of the achievable spatial resolution of the CT system (cf. Sec. 2.2). Typically x-ray tubes are classified by the size of the focal spot into minifocus, microfocus and nanofocus tubes with focals spot sizes around one millimeter, few micrometers, and several hundred nanometers, respectively. To better distinguish conceptually from microfocus tubes, the less frequently used term macrofocus tube is used in this work for a type of x-ray tube with a focal spot size of about one millimeter. The technical differences of these two types of x-ray tubes are discussed in the following.

i.) Macrofocus X-Ray Tubes

A scheme of a macrofocus x-ray tube is given on the left side of Fig. 2.2. The construction is basically the same as already discussed above: a cathode emits electrons which are accelerated to the anode by applying a tube voltage U_B where x-ray photons are generated. In addition to the basic setup, the electrons emitted at the cathode pass through a grid cap, also known as Wehnelt cylinder. This component has a negative potential with respect to the cathode and is used to focus the electron beam and control its intensity [75], e.g. by applying a very high bias voltage U_G on the grid cap, the x-ray tube can be switched off almost immediately. Whilst a higher bias voltage may lead to a more focused electron beam it also leads to a decreased beam current, however, resulting in a trade-off between focal spot size and electron beam intensity. Often two operating modes are provided for macrofocus x-ray tubes, which allow different focal spot sizes at different tube powers $P = U_\mathrm{B} \, I$ [15]. For the x-ray tube shown in Fig. 2.2, the anode itself corresponds to the target, which is tapered with an anode angle φ. Not quite accurately, one speaks of reflection targets for such tapered targets because the usable fraction of the x-ray radiation corresponds to more or less perpendicularly emitted photons. This target construction type allows for a direct cooling and therefore high tube powers can be achieved. Another benefit of this target design is that depending

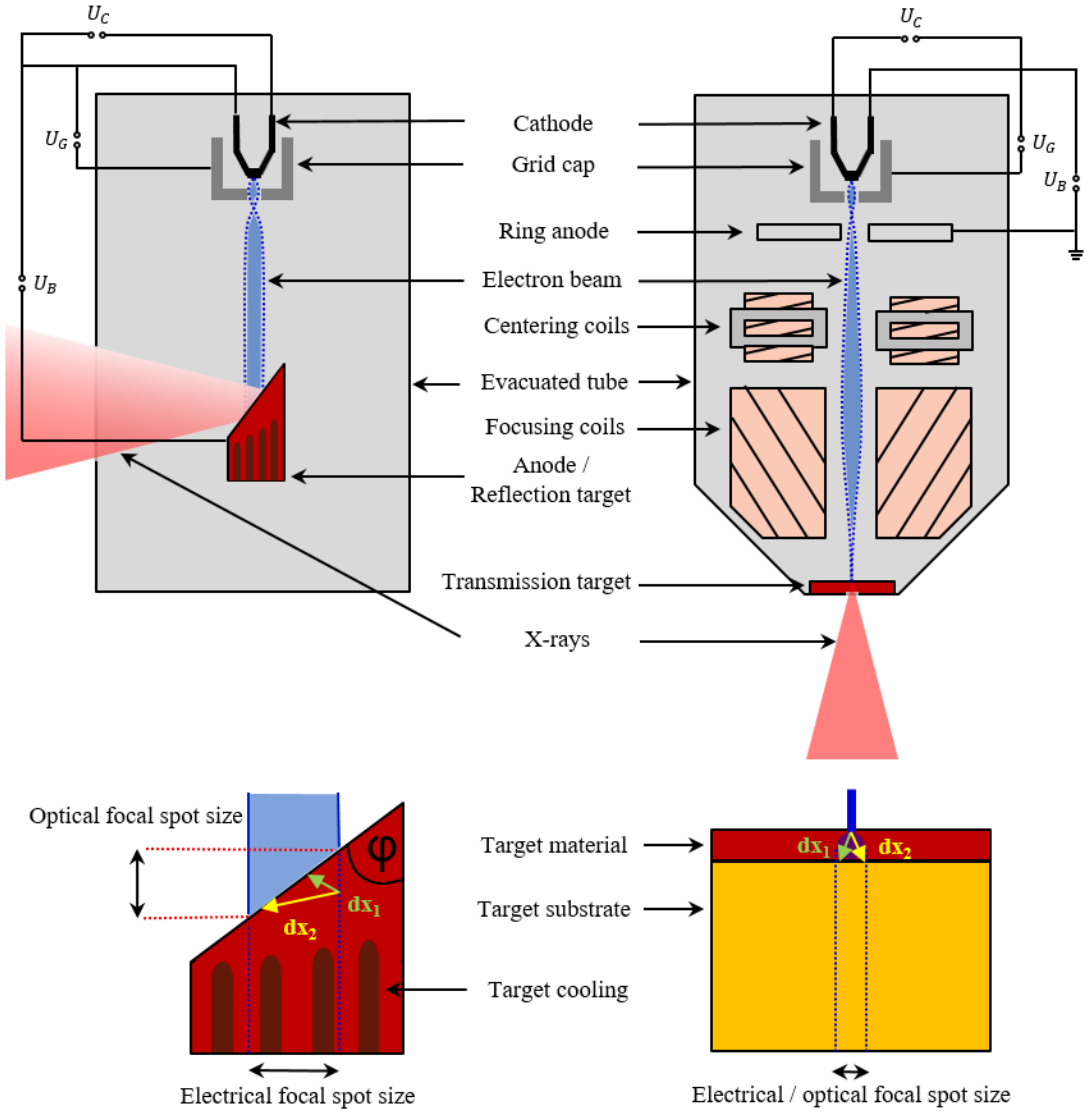

Figure 2.2: On the left side of this figure a scheme of a macrofocus tube with a reflection target is shown. On the right side, a microfocus tube with a transmission target is depicted. The figures on the bottom show a close-up of each target type. For one arbitrary photon emission location in the target, dx_1 and dx_2 depict the different intersection lengths a photon has with the target material depending on its emission angle, which leads to the heel effect in reflection targets [77].

on the anode angle φ, the optical focal spot size is smaller than the electrical focal spot size, which can be seen in the close-up of the reflection target in Fig. 2.2. However, the same illustration shows that the intersection length of generated x-rays within the target

material differs for different emission angles ($dx_1 < dx_2$), which results in unwanted inhomogeneities of the intensity and energy distributions (cf. Sec. 2.1.2), known as the heel effect [77]. X-ray tubes with stationary targets, as the one shown in the figure here, can be operated up to tube powers of 10 kW [78] at focal spot sizes of about one millimeter [75]. In diagnostic CTs, where tube powers may exceed 100 kW to enable very short acquisition times, rotating anodes are used to effectively dissipate the heat [15]. Bipolar reflection tubes[1], where the cathode is at a negative high voltage and the anode is at a positive high voltage, can generate tube voltages of up to 600 kV and thus photon energies of up to 600 keV [80] are achievable.

Exemplary tube spectra for an x-ray tube with a tungsten reflection target and an anode angle of $\varphi = 12°$ modelled with the semi-empirical model of Tucker et al. [81] for tube voltages ranging from 80 to 140 kV are shown in Fig. 2.3.

ii.) Microfocus X-Ray Tubes

On the right side of Fig. 2.2 a sketch of a microfocus x-ray tube is shown. There are several major differences in this tube design compared to that of the macrofocus tube. Firstly, the anode is designed as ring anode and is separated from the target. Then there is a combination of coil components. The centering coils are used to control the position of the electron beam on the target. Even though it is not explicitly shown on the left side of Fig. 2.2 for the macrofocus tube, such centering coils are not unique to microfocus tubes. In fact many diagnostic CT scanners with macrofocus tubes use this type of electromagnets to rapidly move the focal spot position in a CT acquisition to improve the sampling rate, a method known as flying focal spot (FFS) technique [82], [83]. Macrofocus tubes in industrial CT scanners typically do not offer this feature, though. The focusing coils are typical for microfocus tubes and can not be found in macrofocus tubes. These coils act as magnetic lenses and focus the electron beam. This way very small electron beam diameters can be achieved at the target position leading to focal spot sizes in the micrometer range [75]. However, due to the very high energy density at the focal spot, the tube power in microfocus tubes is limited for thermal reasons.

Instead of a reflection target, a transmission target is used in the microfocus tube in Fig. 2.2. As can be seen in the close-up of the target in this illustration, a transmission target consists of a very thin layer of a few micrometers of the actual target material, which is attached to a thicker substrate layer [84]. The substrate must be stable enough to withstand the pressure difference between the vacuum in the tube and the surrounding atmosphere and have a high thermal conductivity so that heat can be dissipated well from the target. In addition, it should have a low density and atomic number so that it does not contribute significantly to the generation of x-ray radiation and the previously generated x-ray quanta are absorbed to a lesser extent (cf. Sec. 2.1.2), which is why crystalline carbon (diamond) is a well-suited substrate material. The thin target layer ensures that the focal spot size is limited to a few micrometers in

[1]There are unipolar and bipolar x-ray tube designs. In unipolar x-ray tubes a negative high voltage is applied to the cathode and the anode is at ground potential [79].

depth dimension. Even though many microfocus tubes are also equipped with reflection targets (see [85]), transmission targets provide some advantages. The heel effect is not a problem for transmission targets because the intersection lengths of the generated photons with the thin target layer are very small and relatively similar in each spatial direction. Furthermore, higher geometric magnifications (cf. Sec. 2.2) can be achieved with transmission targets because the focal spot is located closer to the outer side of the tube window compared to reflection targets, so that the object can be scanned closer to the focal spot. Moreover, the very thin target results in a smaller focal spot size at higher photon fluxes [86]. On the other hand, a disadvantage of transmission targets is their limited heat dissipation capacity, since cooling can not be integrated into the thin layer of the target material.

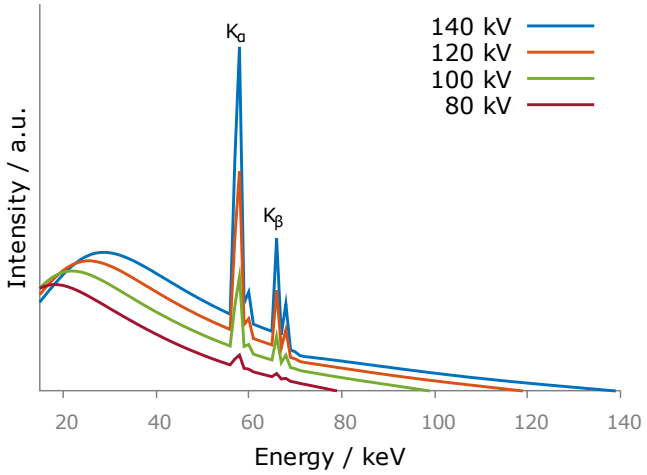

Figure 2.3: Simulated x-ray spectra emitted by an x-ray tube with a tungsten reflection target for different tube voltages. Each spectrum is normalized with respect to the integrated signal of the 140 kV spectrum.

2.1.2 Photon Matter Interactions

As soon as x-ray radiation penetrates matter, the initial intensity I_0 of the radiation is attenuated. The associated loss of radiation intensity is exponential and the remaining intensity $I(d)$ after passing an object of thickness d is described by the Lambert-Beer law:

$$I(d) = I_0\, e^{-\mu\, d} \tag{2.3}$$

The variable μ in this equation corresponds to the linear attenuation coefficient. This coefficient includes all interactions of electromagnetic radiation with matter in the relevant energy range and depends on the chemical composition of the material, its density ρ and the energy $E_\gamma = E$ of the radiation. Generalizing the Lambert-Beer law

with respect to inhomogeneous objects and photon energies E yields

$$I(E, d) = I_0 \, e^{-\int_0^d \mu(\lambda, E) \, d\lambda}. \tag{2.4}$$

In the energy range of x-ray photons used for medical and industrial CT applications, which typically varies between $\mathcal{O}(10\,\mathrm{keV})$ and $\mathcal{O}(100\,\mathrm{keV})$, there are three interactions of electromagnetic radiation with matter that are relevant: coherent scattering (Rayleigh and Thomson scattering), photoelectric absorption, and incoherent scattering due to the Compton effect. The attenuation coefficient $\mu(E)$ therefore corresponds to a superposition of these effects

$$\mu(E) = \mu_\mathrm{R}(E) + \mu_\mathrm{P}(E) + \mu_\mathrm{C}(E), \tag{2.5}$$

where each individual linear attenuation coefficient term can also be formulated with respect to the cross section σ of such an interaction [16]

$$\mu_\mathrm{R/P/C}(E) = \frac{\rho \, N_\mathrm{A}}{A} \, \sigma_\mathrm{R/P/C}(E) \tag{2.6}$$

with ρ being the density of the material, $N_\mathrm{A} = 6.02214076 \cdot 10^{23}\,\mathrm{mol}^{-1}$ the Avogadro constant, and A the atomic weight of the material. The different attenuating effects and their dependence on the photon energies and the material of the attenuator are described in more detail the following.

i.) Rayleigh Scattering

Rayleigh scattering describes the process in which electrons bound in the atom or molecule are excited to dipole oscillations by an incident photon and a photon of the same energy is emitted at a certain scattering angle. The cross section of this process is given by [87]

$$\sigma_\mathrm{R}(E) \propto \frac{\omega^4}{(\omega_0^2 - \omega^2)^2 + \omega^2 \, \gamma^2}, \tag{2.7}$$

where $\omega = 2\,\pi\,E/h$ describes the photon's angular frequency, ω_0 the eigenfrequency of the bound electron on which scattering occurs and γ the damping factor of the oscillation. The eigenfrequency of the bound electrons is typically much lower than the frequency of x-ray radiation. A corresponding coherent scattering process with $\omega \gg \omega_0$, which is also obtained in the limit of free or weakly bound electrons, is called Thomson scattering. According to Eq. (2.7), the cross section for such an interaction approaches a constant value in this case. In reality, the underlying scattering process not only involves a single electron, but all Z electrons of the atom. Furthermore, interference effects occur because the wavelength of high energetic radiation, such as x-rays, is not small compared to the atom size any more. These effects are described by so-called atomic form factors which can be calculated if the electron density distribution of the atom is known. It can be observed that due to these effects, the cross section for coherent

scattering in x-ray imaging decreases for increasing photon energies and grows with the atomic number Z of the atom [88]. As in clinical and industrial CT applications the relevant photon energies are relatively high and the energy deposited in the dipole oscillation in order to be released in a coherently scattered photon is limited by the fact that ionization or excitation of the atom must be avoided, other photon matter interactions, namely the photoelectric and Compton effect, are dominating.

ii.) Photoelectric Effect

The photoelectric effect is based on the absorption of an x-ray photon by a bound electron. This absorption process can only take place if the energy of the photon is at least as high as the binding energy of the electron $E \geq E_\mathrm{b}$. If the photon energy exceeds the binding energy of the electron, this energy difference is transferred to the now free electron in form of kinetic energy $E_\mathrm{kin,e} = E - E_\mathrm{b}$. An exact calculation of the effective cross section for photoelectric interactions is difficult, since in principle the quantum mechanical analysis of the wave function of the entire electron shell is required. However, a formula of the photo effect cross section can be approximated by only considering the cross section for K-shell electrons, which have the largest part of the total cross section of this interaction anyway [89], [90]:

$$\sigma_\mathrm{P}(E) \propto \begin{cases} \frac{Z^5}{E^{7/2}} & \text{for } E > E_\mathrm{b}(K) \\ \frac{Z^5}{E} & \text{for } E \gg E_\mathrm{b}(K) \end{cases} \tag{2.8}$$

Photoelectric absorption is thus especially pronounced in high-Z materials at relatively low photon energies E.

iii.) Compton Scattering

The Compton effect corresponds to an incoherent scattering process in which a photon collides with a quasi-free or weakly bound electron and is scattered under an angle ϑ after this collision. Thereby, the photon transfers part of its energy to the electron. Assuming a free electron, the energy of the photon after the collision can be calculated by following energy and momentum conservation laws. As a consequence, the photon energy after the collision is given by:

$$E' = \frac{E}{1 + \frac{E}{m_\mathrm{e}\,c^2}(1 - cos(\vartheta))} \tag{2.9}$$

The cross section of scattering interactions of photons with free electrons by means of the Compton effect can be calculated by integrating the differential cross section given by the Klein-Nishina formula [91], which yields [92]

$$\sigma_\mathrm{C,KN}(E) \propto \frac{1+\alpha}{\alpha^2}\left(\frac{2\,(1+\alpha)}{1+2\,\alpha} - \frac{\ln(1+2\,\alpha)}{\alpha}\right) + \frac{\ln(1+2\,\alpha)}{2\,\alpha} - \frac{1+3\,\alpha}{(1+2\,\alpha)^2}, \tag{2.10}$$

where $\alpha = \frac{E}{m_\mathrm{e}\,c^2}$ corresponds to the fraction of the photon energy and the rest energy of the electron. For scattering events at bound electrons in the atom, the Klein-Nishina

formula requires a modification. This modification is typically accounted for by a so-called incoherent scattering function. When this incoherent scattering function is considered, the cross section for Compton scattering is approximately proportional to the Klein-Nishina cross section multiplied with the atomic number Z [92]:

$$\sigma_{\mathrm{C}}(E) \approx Z\,\sigma_{\mathrm{C,KN}}(E) \tag{2.11}$$

According to the above equations the cross section for Compton scattering grows with the atomic number Z and whilst approaching a constant value for $E \ll m_{\mathrm{e}}\,c^2$, it decreases for very large photon energies $E \gg m_{\mathrm{e}}\,c^2$ according to $\sigma_{\mathrm{C}}(E) \propto Z/E$. Compared to the photoelectric effect, the energy limit of $m_{\mathrm{e}}\,c^2$ is much higher than typical binding energies E_{b} of attenuator atoms, which is why the Compton effect shows a relatively small energy dependence for the energy range that is relevant for CT compared to the photo effect. As a result, the Compton effect cross section exceeds that of the photoelectric effect for high photon energies. In contrast to Rayleigh scattering, where the supplied energy must not lead to ionization or excitation of the atom, restraining this scattering process to rather low energies, this restriction does not play a role for Compton scattering, which is why Compton scattering corresponds to the dominating x-ray matter interaction for high photon energies in CT [93]. For the same reason, Rayleigh scattering is strongly forward directed for photons in the x-ray energy range, while Compton scattering is more isotropically distributed [93], [94].

Figure 2.4 shows how the total attenuation coefficient is composed of the attenuation coefficients for the photo effect, Rayleigh and Compton scattering for two exemplary materials aluminum and tin. Whilst aluminum corresponds to a characteristic workpiece material in industrial CT measurements, tin corresponds to a typical prefilter material. The role of the prefilter is discussed in the following.

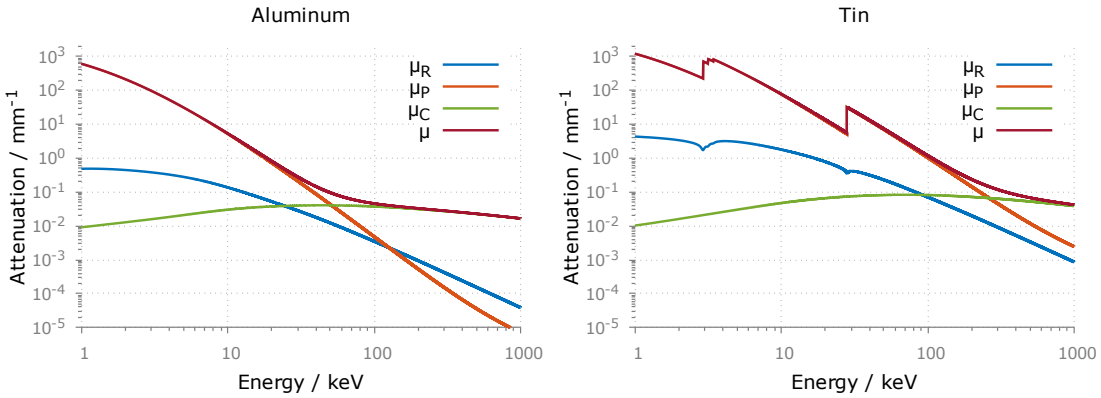

Figure 2.4: Left: energy dependent attenuation coefficients due to Rayleigh scattering (μ_{R}), photoelectric effect (μ_{P}), Compton scattering (μ_{C}), and the resulting total attenuation (μ, see Eq. (2.5)) in aluminum ($Z = 13$, $\rho = 2.7\,\mathrm{g\,cm^{-3}}$). Right: similar depiction for tin ($Z = 50$, $\rho = 7.27\,\mathrm{g\,cm^{-3}}$) as attenuator. Data taken from [95].

2.1.3 Prefiltration and Object Attenuation

As the x-ray photons generated in the x-ray tube are not monochromatic but a polychromatic tube spectrum $w_\mathrm{t}(E)$ is emitted and the attenuation coefficient depends on the photon energies (cf. Figs. 2.3 and 2.4), this must be taken into account when considering x-ray attenuation. It can be seen in Fig. 2.1 that the x-rays usually first pass a so-called prefilter before any interaction with the scanned object occurs. The prefilter typically corresponds to a homogeneous material of a constant thickness. Due to the energy-dependent attenuation behaviour of matter described above, the prefilter leads to an overall reduction of the photon flux arriving at the object and detector and also changes the energy distribution of the spectrum.

By adding a prefilter of thickness d_f with an attenuation of $\mu_\mathrm{f}(E)$ to the CT setup, the energy spectrum of transmitted photons is given by

$$\begin{aligned} w_\mathrm{p}(E) &= \kappa(E)\, w_\mathrm{t}(E), \\ \kappa(E) &= e^{-\mu_\mathrm{f}(E)\, d_\mathrm{f}} \end{aligned} \tag{2.12}$$

where $\kappa(E)$ corresponds to the attenuation caused by the prefilter and $w_\mathrm{t}(E)$ describes the above mentioned unattenuated x-ray spectrum emitted by the x-ray tube.

Using the 140 kV tube spectrum shown in Fig. 2.3, Fig. 2.5 depicts the impact of a tin prefilter of different thickness on this emission spectrum. The figure shows that the prefilter changes the shape of the x-ray spectrum by reducing the photon flux predominantly in low-energy regions. This results in a reduced width of the spectrum and a shift of its mean energy towards higher energies. Furthermore, it can be seen that for a relatively small filter thickness of 0.5 mm there is a peak of the transmitted spectrum between 20 keV up to almost 30 keV and at slightly higher energies the transmission is completely suppressed again. This is due to the attenuation peak of tin at approximately 29 keV (see Fig. 2.4), which corresponds to the binding energy of K-shell electrons in tin. Beyond this energy, photoelectric absorption can also occur for K-shell electrons, which is why the attenuation peaks at this energy. One refers to such an attenuation edge as K-edge of the respective material. For thicker prefilters the effect of the tin K-edge can not be observed any more for the here considered spectrum. Besides the influence of the K-edge on the transmitted spectrum, this figure also illustrates the non-linear attenuation behavior of x-ray radiation with increasing absorber thickness, as whilst the prefilter thickness is increased linearly, the integrated intensities of the spectra decrease non-linearly.

The reasons for using a prefilter in a CT system are manifold. As shown above, the interaction probability of x-ray photons with matter decreases rapidly for increasing photon energies. Therefore, nearly all low-energy photons would be absorbed in a patient or object where they would deploy dose[2] without transferring any information to the x-ray detector. Furthermore, prefiltration reduces the polychromaticity of the spectrum and shifts its center energy towards higher energies. This way systematic

[2] Dose is defined as the locally absorbed radiation energy per unit mass [96] and is associated with potential health risks for patients for ionizing x-ray radiation.

deviations that occur in CT due to the polychromatic nature of the x-ray spectrum, which are discussed in more detail in section 2.3.2, can be reduced. Moreover, x-ray detectors have a limited dynamic range and prefilters avoid a saturation of the measured signals.

Besides the here described prefilters of homogeneous thickness, filters with inhomogeneous thicknesses are also used, especially in clinical CT setups. Prominent examples are bowtie filters, which have this name due to their shape. They are used to produce a more homogeneous dose for typical patient anatomies. Wedge filters, on the other hand, counteract the intensity gradient and spectral shift due to the heel effect mentioned in section 2.1.1 [15].

According to the Lambert-Beer law (Eq. (2.4)) the x-ray intensities after passing through a prefilter and an inhomogeneous object of size d are thus described by

$$I(d) = \int dE\, w_\mathrm{p}(E)\, e^{-\int_0^d \mu(\lambda,E)\, d\lambda}. \tag{2.13}$$

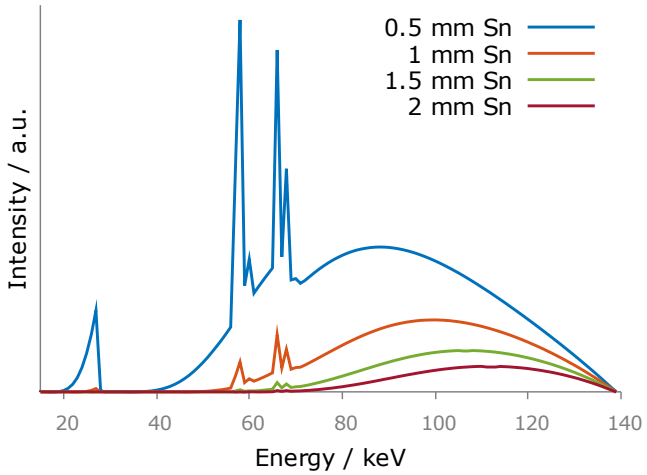

Figure 2.5: X-ray spectra after having passed different thicknesses of tin for the 140 kV tube spectrum from Fig. 2.3. Each spectrum is normalized with respect to the integrated signal of the unattenuated 140 kV spectrum.

2.1.4 Detection of X-Rays

In order to be able to further process the transmission information given by equation (2.13), the x-rays must be converted into an electrical signal at an x-ray detector and digitized. Since the energy stored in the x-rays must be deposited in the detector for this purpose, the detection of the x-rays is also based on the absorption mechanisms discussed above. In this context, the efficiency of the detection process corresponds to the fraction of the energy stored in the radiation that is deposited in the detector via absorption processes. Therefore, similar to the absorption in the prefilter and object,

the detection efficiency depends primarily on the attenuation coefficient of the detector material μ_{D}, the thickness of the effective detection layer d_{D}, and the radiation energy E. Assuming that the total energy of the x-ray photons interacting with the detection layer is completely absorbed, the detection efficiency η can be formulated as follows:

$$\eta(E) = 1 - e^{-\mu_{\mathrm{D}}(E)\, d_{\mathrm{D}}} \tag{2.14}$$

It should be noted that this formula is only an approximation because, as already explained, the energy of x-rays is not completely absorbed by every kind of photon-matter interactions. Photons interacting by the Rayleigh or Compton effect do not deposit any or only a part of their energy in the detector. Therefore, the above formula generally leads to an overestimation of the detection efficiency. Even if the detection process can be mapped more precisely [97], for the sake of simplicity, formula (2.14) is used here.

To calculate the detected signal S, the detector efficiency must be integrated into the Lambert-Beer law. With formula (2.13) one therefore obtains for the detected signal

$$S(d) = \int dE\, w_{\mathrm{p}}(E)\, \eta(E)\, \epsilon\, e^{-\int_0^d \mu(\lambda,E)\, d\lambda}, \tag{2.15}$$

where ϵ corresponds to a scaling factor that depends on the detection technology (see i.) and ii.)):

$$\epsilon \propto \begin{cases} E & \text{for indirect converting detectors} \\ 1 & \text{for direct converting detectors} \end{cases} \tag{2.16}$$

The transmission $\tau(d)$ can now be calculated by normalizing this signal with the signal which is not attenuated by the object:

$$\tau(d) = \frac{\int dE\, w_{\mathrm{p}}(E)\, \eta(E)\, \epsilon\, e^{-\int_0^d \mu(\lambda,E)\, d\lambda}}{\int dE\, w_{\mathrm{p}}(E)\, \eta(E)\, \epsilon} \tag{2.17}$$

By defining the normalized detected spectrum

$$\begin{aligned} w(E) &= \frac{w_{\mathrm{p}}(E)\, \eta(E)\, \epsilon}{\int dE\, w_{\mathrm{p}}(E)\, \eta(E)\, \epsilon}, \\ \int dE\, w(E) &= 1, \end{aligned} \tag{2.18}$$

equation (2.17) becomes

$$\tau(d) = \int dE\, w(E)\, e^{-\int_0^d \mu(\lambda,E)\, d\lambda}. \tag{2.19}$$

Besides the detection efficiency, the dynamic range of a detector also plays an important role. The dynamic range is defined by the range of the largest detectable signal from which the detector signal saturates and the smallest detectable signal which

exceeds the background noise of the detector [15]. Accordingly, the dynamic range is determined by the frame rate and the background noise of the detector.

Nowadays, there are two detection technologies used in CT which differ fundamentally in the detection mechanisms of x-rays: indirect converting detectors and direct converting detectors. Both technologies are described in more detail in the following and the respective detection process is exemplified in Fig. 2.6.

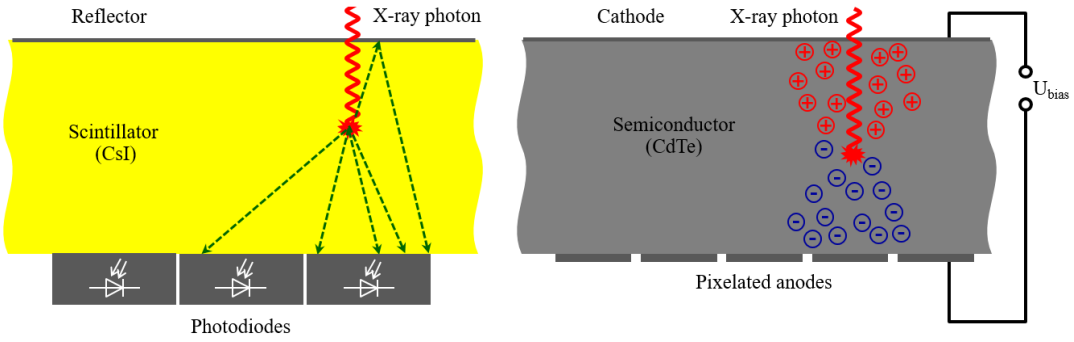

Figure 2.6: Illustrations of an indirect converting detector (left) and a direct converting detector (right).

i.) Indirect Converting Detectors

In indirect converting detectors, the detector signal is obtained by a two-phase process: first, x-ray photons are converted into optical photons in a scintillator. The optical photons thus produced then generate an electrical signal in a photodiode (cf. Fig. 2.6).

As the x-ray quantum passes through the scintillator, it generates a large number of electron-hole pairs proportional to its energy. These react with the activation centers of the crystal, which undergo energetic relaxation and thereby emit optical photons [15]. The optical photons must then be directed to the photodiode. The requirements for the scintillator material are therefore given by a high conversion rate of x-ray photons into optical light with a good light transmission at the same time. While for flat detectors used in CBCT often thallium or sodium doped cesium iodide (CsI:Tl or CsI:Na) is used as scintillator material due to its crystalline microstructure that acts as a light guide [98], terbium doped gadolinium oxysulfide $Gd_2O_2S : Tb$ (also GOS:Tb) is typically used in curved detectors for MSCT due to the fast decay time of the light signal [15]. Each detector element, or detector pixel, is equipped with a photodiode which converts the optical photons into an electrical signal [16].

Since the decay time of the signal in this conversion process is up to 10 µs [99], which is too slow to distinguish individual photons at typical CT photon fluxes, the signal of the individual photons, which is proportional to their energy, is summed by the detection process. Therefore, one refers to this type of detector as energy-integrating detector (EID).

ii.) Direct Converting Detectors

In contrast to the two-phase conversion process in indirect converting detectors, in a direct converting detector the x-ray photon is converted into electron-hole pairs in a semiconductor and thereby induces a measurable electric signal without an intermediate step. The semiconductor material in direct converting x-ray detectors is usually cadmium telluride (CdTe) or cadmium zinc telluride (CdZnTe) [62], [100] because these materials effectively absorb x-rays even at high photon energies due to their comparatively high density (e.g. $\rho = 5.85\,\mathrm{g\,cm^{-3}}$ for CdTe [101]). A high voltage, called bias voltage U_{bias} of about 500 V [102], is applied between the cathode attached to the detector surface and the pixelated anode located behind the semiconductor layer. Electrons and holes therefore move along the electric field to the anode and cathode, respectively (cf. Fig. 2.6). Thereby they generate a measurable current in the pixelated anode. These pixels are each connected to application-specific integrated circuits (ASICs), in which the signal is first amplified and shaped. In addition, the ASIC contains digital-to-analog converters (DAC), N pulse height comparators and N counters, where the number of thresholds N depends on the manufacturer and ranges from 2 to 8 [62]. If the measured signal height exceeds any of the N set thresholds, the corresponding counter registers an event. By subtracting the counts registered in the counter for the adjacent, higher threshold, the number of detected events in the considered signal height interval is obtained. The DAC allows fine-tuning of the threshold values. Since the number of generated electron-hole pairs and the associated signal height in the ASIC is proportional to the energy of the detected x-ray photon, the adjusted threshold values correspond to energy thresholds that allow to assign a photon energy to the measured counts. As the signal pulse duration is only several nanoseconds for direct converting detectors [103], single impinging photons can be differentiated and ideally each measured photon count can be assigned with the energy of the photon which induced the signal. This type of detector is therefore also referred to as photon-counting detector (PCD).

The slow establishment of PCDs for commercial use in CT, besides their high price, is mainly due to various perturbing effects that play a role in such semiconductor detectors: impinging x-ray photons may interact with the semiconductor materials via Compton scattering or photoelectric effect, which can lead to the emission of secondary fluorescent photons (K-escape). Both of these processes can lead to a transfer of energies to other neighboring detector pixels. A similar effect is caused by charge sharing [104]. Charge sharing corresponds to the detection of a charge cloud, which is generated in the semiconductor by a single photon of a certain energy, by two or more distinct pixels. Each of these pixels then receives a signal that corresponds to that generated by photons of lower energies. This effect is caused by diffusion and Coulomb repulsion of the generated charges within the semiconductor. Some photon-counting (PC) detectors can mitigate charge sharing and fluorescence effects by using so-called charge summing circuits [105], in which neighboring pixels detect coincidences to reconstruct the correct charge at a pixel. Other signal disturbances in PC detectors are caused by semiconductor impurities (charge trapping), multiplicity of counts for high photon fluxes (pulse pileup), or the decrease of charge collection efficiency due

to polarization effects in the semiconductor material. Reference [62] provides a good overview of the mentioned perturbation effects.

Nevertheless, the direct converting detector technology offers several advantages compared to indirect converting detection methods that are relevant to CT, such as energy-resolved measurements, better measurement statistics, and smaller detector pixels [51], [60], [61]. Therefore, this technology will likely play a larger role in x-ray CT imaging in the future and the first commercially available MSCT system with direct converting detector technology has been released in 2021.

2.1.5 X-Ray Computed Tomography Reconstruction

After explaining the setup of a CT and discussing the individual components of the measurement process including their underlying physical processes, this section deals with the reconstruction of the acquired transmission signals into a CT volume. The theoretical background to the reconstruction presented in the following represents a rough overview rather than a complete elaboration. For a more detailed consideration, please refer to the relevant literature [15], [16], [106].

To recover object information in form of the attenuation coefficients μ from transmission information, the Lambert-Beer law (Eq. (2.3)) states that the measured x-ray intensities must be normalized and logarithmized. According to equation (2.19), this means that the so-called projection value which is to be reconstructed is given by:

$$q(d) = -\ln(\tau(d)) = -\ln\left(\int dE\, w(E)\, e^{-\int_0^d \mu(\lambda,E)\, d\lambda}\right) \tag{2.20}$$

It should be noted that the normalization of the measured x-ray intensities in this formula is implicitly given by the use of the detected spectrum $\omega(E)$ normalized with respect to the unattenuated x-ray spectrum.

i.) Filtered Backprojection

The filtered backprojection (FBP) is the standard method for analytical image reconstruction. In this section, FBP is derived for parallel beam geometries (cf. Fig. 2.7). The FBP is based on the assumption that the measured projection values are linearly related to line integrals over the attenuation coefficients. Thus, for an one-dimensional linear detector, a projection value at detector position ξ and rotation angle ϑ is given by:

$$p(\vartheta, \xi) = \int_{-\infty}^{\infty} \mu(\xi, \eta)\, d\eta \tag{2.21}$$

Such a projection of a function along a line integral is mathematically referred to as an x-ray transform, which in the two-dimensional case presented here corresponds to the so-called Radon transform. The assumption that the measured projection value corresponds to a line integral over the linear attenuation coefficients is incorrect for polychromatic tube spectra as used in CT, where the actual measured projection value

q is given by equation (2.20). Neglecting the polychromatic x-ray spectrum and the non-linear energy dependency of the transmission of x-rays in the reconstruction of the projection data, expressed by the ambiguity of equation (2.21) and (2.20), results in systematic deviations in the reconstructed CT volume, which are described in more detail in section 2.3.2.

With the definition of the ray position $\xi = x\cos\vartheta + y\sin\vartheta$ and its normal $\eta = -x\sin\vartheta + y\cos\vartheta$, equation (2.21) can be expressed as

$$p(\vartheta,\xi) = \int_{-\infty}^{\infty}\int_{-\infty}^{\infty} f(x,y)\,\delta(x\cos\vartheta + y\sin\vartheta - \xi)\,dx\,dy\,, \tag{2.22}$$

(see Fig. 2.7), where δ corresponds to the Dirac delta function and $f(x,y) = \mu(\xi(x,y),\eta(x,y))$ is the object function in the non-moving inertial system.

To convert the above equation according to the object function $f(x,y)$ in spatial domain, one makes use of the Fourier slice theorem. This theorem states that the one-dimensional Fourier transform of a projection in parallel beam geometry with respect to its sampling parameter ξ at an angle ϑ is equal to a radial line of the two-dimensional Fourier transform of the desired object function in polar coordinates along this angle [15]

$$\mathcal{F}_{1,\xi}\,p(\vartheta,\rho) = \mathcal{F}_2\,f(\rho\cos\vartheta,\rho\sin\vartheta)\,. \tag{2.23}$$

The filtered backprojection can thus be formulated as:

$$\begin{aligned}
f(x,y) &= \mathcal{F}_2^{-1}\,\mathcal{F}_2\,f(x,y)\\
&= \int_{-\infty}^{\infty}\int_{-\infty}^{\infty} \mathcal{F}_2\,f(u,v)\,e^{2\pi i\,(x\,u+y\,v)}\,du\,dv\\
&= \int_{0}^{\pi}\int_{-\infty}^{\infty} \mathcal{F}_2\,f(\rho\cos\vartheta,\rho\sin\vartheta)\,e^{2\pi i\,\rho\,(x\cos\vartheta+y\sin\vartheta)}\,|\rho|\,d\rho\,d\vartheta\\
&= \int_{0}^{\pi}\int_{-\infty}^{\infty} \mathcal{F}_{1,\xi}\,p(\vartheta,\rho)\,e^{2\pi i\,\rho\,(x\cos\vartheta+y\sin\vartheta)}\,|\rho|\,d\rho\,d\vartheta\\
&= \int_{0}^{\pi}\int_{-\infty}^{\infty}\int_{-\infty}^{\infty} p(\vartheta,\xi)\,e^{-2\pi i\,\rho\,\xi}\,d\xi\,e^{2\pi i\,\rho\,(x\cos\vartheta+y\sin\vartheta)}\,|\rho|\,d\rho\,d\vartheta\\
&= \int_{0}^{\pi}\int_{-\infty}^{\infty} p(\vartheta,\xi)\int_{-\infty}^{\infty} e^{2\pi i\,\rho\,(x\cos\vartheta+y\sin\vartheta-\xi)}\,|\rho|\,d\rho\,d\xi\,d\vartheta\\
&= \int_{0}^{\pi}\int_{-\infty}^{\infty} p(\vartheta,\xi)k(x\cos\vartheta + y\sin\vartheta - \xi)\,d\xi\,d\vartheta\\
&= \underbrace{\int_{0}^{\pi} \underbrace{(p*k)}_{\text{filtering}}(\vartheta, x\cos\vartheta + y\sin\vartheta)\,d\vartheta}_{\text{backprojection}}
\end{aligned} \tag{2.24}$$

Here, the reconstruction kernel

$$k(\xi) = \int_{-\infty}^{\infty} |\rho|\,e^{2\pi i\,\rho\,\xi}\,d\rho = -\frac{1}{2\,\pi^2\,\xi^2} \tag{2.25}$$

was used in the second-last step and the convolution definition

$$(f * g)(x) = f(x) * g(x) = \int f(t)\, g(x - t)\, dt \tag{2.26}$$

was used in the last step. The reconstruction kernel from Eq. (2.25) is commonly known as ramp-filter because of its shape in Fourier space. In the transition to polar coordinates in the third step it was taken into account that the Fourier transform of projections in parallel beam geometry in an angular interval of $[0, \pi[$ cover the complete two-dimensional Fourier space of the object function. This means at the same time that for a reconstruction of the full image information an angular sampling of at least 180° must be given in the case of parallel beam geometries. According to equation (2.24), the filtered backprojection thus corresponds to a two-step process in which the projection values are first convolved and then integrated along the curve $\xi = x\cos\vartheta + y\sin\vartheta$ within a 180 degree interval for the different rotation steps ϑ.

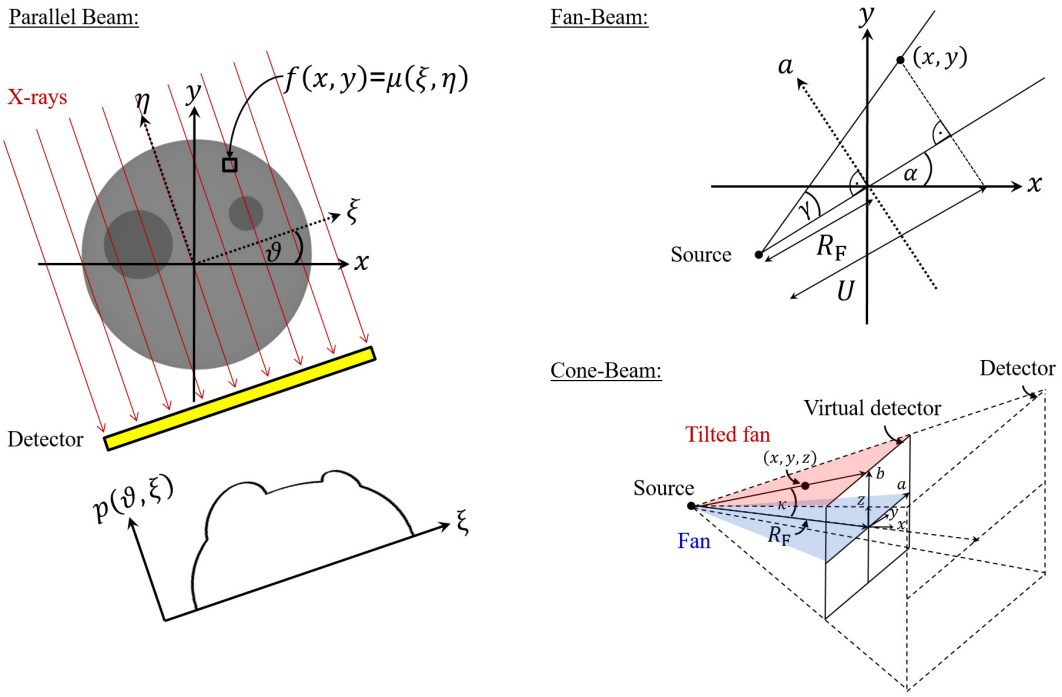

Figure 2.7: Schematic illustration of a parallel beam geometry with a corresponding projection p parameterized by the distance ξ and the angle ϑ (left) and illustrations of the fan-beam (top right) and cone-beam geometries (bottom right) after [107] and [108] with the rotation angle α, the fan angle γ, the cone angle κ, and the virtual detector coordinates a and b.

ii.) Cone-Beam Reconstruction using Filtered Backprojection

The parallel beam geometry used to derive the FBP in the previous section simplifies the analysis of the CT reconstruction but is not relevant for modern CT systems. In the case of CBCT with flat detectors, which is shown in Fig. 2.1 and which is mainly treated in this work, some modifications to the FBP for parallel beam geometries have to be made in order to properly reconstruct this data. A very common reconstruction scheme for CBCT circle scan projection data is the algorithm by Feldkamp, Davis and Kress [8], commonly referred to as Feldkamp Davis Kress (FDK) algorithm.

The illustrations on the right side of Fig. 2.7 show the cone-beam geometry and its parameterization, which is used for the mathematical formulation of the FDK algorithm. Ray directions are defined by the projection angle α, the fan angle γ and the cone angle κ. To simplify the mathematical description, the geometry is defined with respect to a virtual detector in the isocenter of rotation with coordinates given by a and b. To adapt the FBP to the divergent beam geometries of cone-beam projections, it is necessary to weight the projections depending on fan and cone angles prior to filtering [107]:

$$\tilde{p}(\alpha, a, b) = \Bigg(\underbrace{\frac{R_\mathrm{F}}{\sqrt{R_\mathrm{F}^2 + a^2 + b^2}}}_{\cos\gamma\cos\kappa} \, p(\alpha, a, b) \Bigg) * k(a) \tag{2.27}$$

Although the projections are two-dimensional, the convolution in the FDK algorithm is performed only in the lateral direction, analogous to Eq. (2.24). The backprojection of the weighted and filtered projections into the three-dimensional object function $f(x, y, z)$ is then performed as

$$f_\mathrm{FDK}(x, y, z) = \frac{1}{2} \int_0^{2\,\pi} \frac{R_\mathrm{F}^2}{U(x, y, z)^2} \, \tilde{p}(\alpha, a(x, y, \alpha), b(x, y, z, \alpha)) \, d\alpha \tag{2.28}$$

with the functions

$$\begin{aligned} a(x, y, \alpha) &= R_\mathrm{F} \, \frac{-x \sin\alpha + y \cos\alpha}{R_\mathrm{F} + x \cos\alpha + y \sin\alpha} \,, \\ b(x, y, z, \alpha) &= z \, \frac{R_\mathrm{F}}{R_\mathrm{F} + x \cos\alpha + y \sin\alpha} \,, \\ U(x, y, \alpha) &= R_\mathrm{F} + x \cos\alpha + y \sin\alpha \,. \end{aligned} \tag{2.29}$$

Unlike the FBP for parallel beam (see above) or fan-beam geometries (cf. [15], [16], [107], [108]) the FDK algorithm corresponds only to an approximate solution for a three-dimensional filtered backprojection. This is due to the Tuy condition [109], which states that an exact solution for an object point to be reconstructed only exists if the source trajectory passes through the plane of this object point at least once. This condition is fulfilled for a CBCT circle scan only for the central plane (midplane). For all other planes, the solution space of the FBP is ambiguous, which results in systematic measurement deviations known as cone-beam artifacts. These deviations increase with

larger cone angles, which is why this effect must be taken into account in the design of CBCT devices and the respective measurement task.

The reconstructed object function $f_{\mathrm{FDK}}(x, y, z)$ forms an object volume that contains the linear attenuation coefficients $\mu(x, y, z)$ (cf. Fig. 2.7). In CT, both the detection of x-ray transmission and the reconstruction into an object volume correspond to a discrete process. Whilst the x-ray intensities are measured at discrete detector elements, the detector pixels, the volume is sampled on a discrete three-dimensional grid of so-called voxels (volumetric pixels). Images of two-dimensional slices through this discretized volume are usually referred to as CT images. Typically, to reconstruct a voxel, the intersection point of a beam originating from the source and crossing the center of the voxel is calculated on the detector and the projection value is interpolated from the discrete detector signal and then filtered backprojected (voxel-driven backprojection) [15].

iii.) Hounsfield Units

In clinical CT applications, the CT image is typically rescaled to CT values, also called Hounsfield units (HU), named after the developer of the first CT device, Sir Godfrey Hounsfield. This unit is defined such that water (H_2O), which is the major component of human body tissue, has a value of 0 HU and air has a value of -1000 HU. Thus, for the conversion of the attenuation coefficient $\mu(x, y, z)$ to CT values, the following equation is applied:

$$\mathrm{CT}(x, y, z) = \frac{\mu(x, y, z) - \mu_{\mathrm{H_2O}}}{\mu_{\mathrm{H_2O}}} \cdot 1000\,\mathrm{HU} \tag{2.30}$$

Rescaling the gray values using the above equation leads to a better quantitative comparability of CT images in CT for medical imaging, since the water-equivalent soft tissue is represented with the same values despite possible differences in the used spectrum. However, this does not mean that any given material will be represented the same way for different tube spectra by a rescaling using equation (2.30). In particular, strongly absorbing materials such as contrast agents, bones, or metals, still show large differences for different spectra after this two-point calibration due to the non-linear energy dependency of the attenuation coefficients.

Because of the higher susceptibility to systematic measurement deviations, such as the above-mentioned inadequacy of the CBCT reconstruction methods or an increased signal due to scattered x-ray photons, which are explained in more detail in section 2.3.3, Hounsfield units have a lower importance in CBCT and some manufacturers of CBCT devices completely omit a rescaling of the CT images. In particular in industrial CT, due to the large variation of workpiece materials and mostly large differences to the attenuation of water, the use of Hounsfield units is atypical. However, sometimes a rescaling of gray values to CT values is useful for industrial CT measurements, as well. Since there are usually predominant materials other than water in workpieces, it makes sense to perform this rescaling of gray values for industrial CT applications with reference to the predominant material in the volume. Therefore, the gray value

of a reference material μ_{Ref} is used instead of $\mu_{\text{H}_2\text{O}}$ in Eq. (2.30) for the gray value conversion to CT values in industrial CT.

2.1.6 Metrological Evaluation

Often, the reconstruction into a volume described above is not yet the final step of the CT measurement process. In particular, in the metrological application of industrial CT, it is necessary to be able to draw conclusions about surface points and surface transitions on the basis of the volume information in order to be able to determine dimensions on the workpiece. For the metrological evaluation of a CT measurement, the reconstructed volume must first be segmented and then the coordinates of surface points must be determined, based on which measures can be calculated. The individual steps are explained in more detail below.

i.) Volume Segmentation

Segmentation is used to separate a CT volume into different segments that are semantically related. While in industrial CT especially the segmentation into different material or density regions plays a role, in medical CT the segmentation of anatomical and pathological tissue structures as well as the delineation of pathological substructures is of particular interest [110]. The three-dimensional classification information obtained by segmentation can then be used to determine surfaces or plan surgical interventions or radiation treatments. Methodologically, segmentation approaches can be distinguished between pixel-oriented, edge-oriented, region-oriented, learning-based, model-based and texture-based methods [111].

In threshold-based segmentations, which belong to the pixel-oriented methods and probably correspond to the simplest segmentation approaches, the volume is divided into N segments $M(x, y, z)$ by $N-1$ thresholds S_i and each voxel is assigned to exactly one of these segments depending on its gray value $\mu(x, y, z)$:

$$M(\mu(x,y,z),x,y,z) = \begin{cases} 0 & \text{if } \mu(x,y,z) < S_0 \\ 1 & \text{if } S_0 \leq \mu(x,y,z) < S_1 \\ & \vdots \\ N-1 & \text{if } \mu(x,y,z) \geq S_{N-2} \end{cases} \tag{2.31}$$

Of great importance in threshold-based segmentation are the exact values of the thresholds and, consequently, their calculation rules. In general, for segmenting a CT volume, globally, locally or dynamically determined threshold values can be used. A simple but error-prone method for the threshold determination of two-material volume data identifies the average of the difference of the highest and lowest gray values as the segmentation threshold (cf. Fig. 2.8). The same principle can be applied to a histogram-based calculation method by defining the threshold by the mean between two local maxima of the gray value distribution. A more sophisticated way for determining segmentation thresholds is given by Otsu's method [112]. This method sets the $N-1$

thresholds such that the gray values within a segment have a minimum variance, while the variance between the different segments is maximal, however.

For edge-oriented segmentations, edge detection operators are typically applied to the volume data [111]. An example of an edge-oriented segmentation is represented by the watershed transformation algorithm [113]. A somewhat outdated discussion of other segmentation algorithms and methods can be found in [110]. Current research is mainly focusing on learning-based segmentation methods [114]–[117].

ii.) Determination of Boundary Surface Points

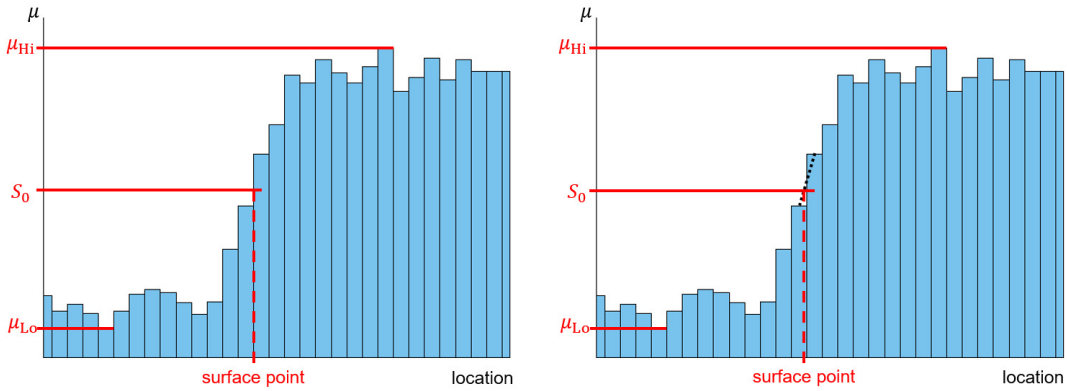

Figure 2.8: Determination of a surface point without subvoxeling (left) and with subvoxeling (right).

In principle, a fully segmented CT volume can already directly be used to determine surface points at a boundary surface between different materials to generate a measuring point cloud. However, the accuracy of the measuring point cloud determined this way is limited by the size of the sampling elements, i.e. the segmented voxels. In coordinate metrology, subvoxel-accurate algorithms, or subpixel-accurate algorithms in the two-dimensional case, are therefore preferred for determining the measurement points [118], [119]. These algorithms are applied directly on a gray-scale image or volume and provide the location of the edge transition based on a previously determined threshold value with an accuracy smaller than the size of the sampling elements. A simple example for subvoxel-accurate computation of boundary surface points is shown in Fig. 2.8. In this case, the edge location is obtained by linearly interpolating the voxel positions for the voxels enclosing the threshold. The marching cubes algorithm [120] corresponds to the most common method for generating isosurfaces for individual material transitions for three-dimensional CT volume data. The surface points are thereby represented in the form of a polygonal mesh. By using material probability maps, surface points for different materials in multi-material CT volume data can be generated with subvoxel precision [121]. Compared to voxel- or pixel-accurate surface point determinations, such subvoxel or subpixel methods can improve the accuracy of the acquired measuring

points by a factor of about ten [122]. Based on the coordinates of the boundary surface points, dimensions can be determined or features of the measured workpiece can be extracted, which is described below.

iii.) Geometry Elements

Geometry elements of a measured workpiece can be determined on the basis of the computed measuring point cloud or a subset of these points. These geometry elements represent mathematical regular geometries on the workpiece surface or at material transitions. Two-dimensional examples of geometry elements would be circles or ellipses and three-dimensional examples would be spheres or cylinders. A workpiece can be composed of a variety of different geometry elements and each workpiece can metrologically be fully described by the set of all geometry elements it contains. The mathematical formulation for the calculation of a geometry element as a fitting curve for the measuring points $t := (t_i)_{i=1,\dots,N}$ is:

$$||t - \psi(x)|| = \min_{y \in \mathbb{R}} ||t - \psi(y)|| \tag{2.32}$$

Here $\psi(x) := \psi(x_j)_{j=1,\dots,M}$ describes the model function for the geometry element to be calculated with the parameters $x_j \in \mathbb{R}$. According to the above equation, depending on the norm that is used, different methods exist to calculate a geometry element as a fitting curve for the measuring points. Common fitting curves represent for example least squares fitting curves ($||.||_2$), minimum zone fitting curves ($||.||_\infty$), or minimum inscribed or enveloping curves [123]. The choice of the right fitting curve used for the calculation of the geometry element depends on the specification of the workpiece component and can therefore differ for different measurement tasks. For calculations of form deviations, the fitting curves to be used are determined by the respective ISO or DIN standard [123], [124].

2.2 Spatial Resolution in X-Ray Computed Tomography

The achievable spatial resolution of the image data corresponds to one of the key characteristics of a CT system. It determines both the size of the smallest structures that can be resolved and the precision of dimensional measurements, thus limiting the measurement tasks that can be solved using CT.

2.2.1 Structural Resolution

The term structural resolution refers to the smallest distance between two object points that can still be distinguished in an image. This distance does not automatically correspond to the smallest object point distance, since the mapping of an object point $f(x, y)$ into an image point $b(x, y)$ is distorted in a certain way by the impulse response of the imaging system. The impulse response of an imaging system for point objects is referred to as the point spread function (PSF). In the case of two-dimensional spatial

signals, such as those represented by x-ray projections or CT images, the following formula describes the relation between object and image point:

$$b(x,y) = (f * \mathrm{PSF})(x,y) = (f * \mathrm{PSF}_{\mathrm{Source}} * \mathrm{PSF}_{\mathrm{Detector}} * \mathrm{PSF}_{\mathrm{Algorithm}})(x,y) \quad (2.33)$$

Thus, the PSF of an image acquired with x-ray optics can be described by the combination of the impulse responses of x-ray tube and x-ray detector and algorithmic modifications of the signal, such as filtering. One way to quantify the structural resolution of a CT system is given by the full width at half maximum (FWHM) of its PSF.

An alternative definition of structural resolution can be obtained using transfer functions. A transfer function describes how a certain property of an input signal is transferred by the system into the output signal. The modulation transfer function (MTF) plays a special role for imaging systems. It describes the transfer of contrasts by the imaging system and is defined by the quotient of image contrast C_{I} and object contrast C_{O} depending on the spatial frequencies k_x and k_y:

$$\mathrm{MTF}(k_x,k_y) = \frac{C_{\mathrm{I}}}{C_{\mathrm{O}}} \quad (2.34)$$

It can be shown that the MTF corresponds to the absolute value of the two-dimensional Fourier transform of the PSF [125]:

$$\mathrm{MTF}(k_x,k_y) = \left| \int_{-\infty}^{\infty} \int_{-\infty}^{\infty} \mathrm{PSF}(x,y) e^{-2\,\pi\,i\,(x\,k_x + y\,k_y)} dx\,dy \right| = |(\mathcal{F}_2\,\mathrm{PSF}(x,y))| \quad (2.35)$$

In this representation, the MTF resembles a two-dimensional function. Practically, however, the MTF is often represented by an one-dimensional profile of this distribution, which passes through the origin of the frequency space. Such an one-dimensional MTF profile can be obtained using the line spread function (LSF), which describes the imaging of an infinitesimally thin slit through the system. If a slit along the y-axis is considered, the LSF is defined by

$$\mathrm{LSF}(x) = \int_{-\infty}^{\infty} \mathrm{PSF}(x,y)\,dy \quad (2.36)$$

and the profile of the MTF is then obtained by computing the absolute value of the Fourier transform of the LSF:

$$\mathrm{MTF}(k_x) = |(\mathcal{F}_1\,\mathrm{LSF}(x))| \quad (2.37)$$

Since the measurement of an infinitesimally thin slit is practically not feasible, use is made of the edge spread function (ESF) and its relation to the LSF. The ESF corresponds to the impulse response of the system for an object edge. Such an edge transition can be found at a certain position in almost any sample. A differentiation of the ESF yields the LSF:

$$\mathrm{LSF}(x) = \frac{d}{dx}\mathrm{ESF}(x) \quad (2.38)$$

Thus, the typical procedure for determining an MTF curve consists of measuring a line profile orthogonal to an edge (ESF) in an image, differentiating this line profile to obtain the LSF, and then performing a Fourier transform, which, expressed as a formula, yields

$$\mathrm{ESF}(x) \xrightarrow{\frac{d}{dx}} \mathrm{LSF}(x) \xrightarrow{\mathcal{F}_1} \mathrm{MTF}(k_x)\,. \tag{2.39}$$

For a rotationally symmetric PSF, i.e.

$$\begin{aligned} \mathrm{PSF}(r,\vartheta) &= \mathrm{PSF}(x,y) \quad \forall\vartheta \\ r^2 &= x^2 + y^2 \end{aligned} \tag{2.40}$$

the LSF is equal to the Abel transform of the PSF [126] and is the same for any angle ϑ of the line input. Thus, the ESF is also the same for an arbitrary edge orientation and an MTF profile $\mathrm{MTF}(k)$ can be determined using

$$\mathrm{ESF}(r,\vartheta) \xrightarrow{\frac{d}{dr}} \mathrm{LSF}(r,\vartheta) \xrightarrow{\mathcal{F}_1} \mathrm{MTF}(k)\,. \tag{2.41}$$

for any orientation of the edge under consideration.

Usually, the structural resolution of a CT system is defined using a scalar value from the MTF instead of the whole curve, e.g., the MTF at 10% contrast transfer [15], [127].

Analogous to the PSF, the MTF can also be divided into different parts corresponding to different elements of the x-ray optics and algorithmic modifications. Unlike in equation (2.33), however, the MTF of the total system corresponds to a multiplication of the individual contributions and not to a convolution, since the MTF corresponds to the Fourier transform of the PSF. Thus, the MTF of the CT system is given by:

$$\mathrm{MTF}(k)_{\mathrm{CT}} = \underbrace{\mathrm{MTF}\,(k)_{\mathrm{Source}} \cdot \mathrm{MTF}\,(k)_{\mathrm{Detector}}}_{\text{Imaging hardware}} \cdot \mathrm{MTF}(k)_{\mathrm{Algorithm}} \tag{2.42}$$

The algorithmically determined part of the MTF in the above equation is defined, potentially among other algorithmic modifications of the signal, by the convolution kernel and interpolation method used for filtered backprojection. Using a linear interpolation scheme between the sampling values of the detector pixels and the Ramachandran and Lakshminarayanan [128] filter, which corresponds to a discrete form of the ramp filter from section 2.1.5, this term gives [16]

$$\mathrm{MTF}(k)_{\mathrm{Algorithm}} = |\mathrm{sinc}(du\,k)|^2, \tag{2.43}$$

where du corresponds to the pixel size. If additional image filters are used, they have to be considered accordingly in the term $\mathrm{MTF}(k)_{\mathrm{Algorithm}}$.

The factors of the MTF in Eq. (2.42) given by the x-ray tube and x-ray detector are strongly depending on the CT geometry that is being used [129]. The geometric magnification describes the optical magnification of an x-ray projection by the use of divergent beams as they occur in fan- or cone-beam geometries and is given by

$$M = \frac{R_{\mathrm{FD}}}{R_{\mathrm{F}}}\,, \tag{2.44}$$

where R_{FD} and R_{F} correspond to the focus-detector and focus-isocenter distance (cf. Fig. 2.1). In general, the spatial resolution of a CT measurement is essentially limited by the used hardware and, depending on the geometric magnification, the limitations of the spatial resolution are more likely to be on the detector side, the x-ray tube side, or evenly distributed. Therefore, it makes sense to adapt the MTF of the x-ray source to that of the detector, for example by using higher tube powers or a reduced focusing current, in order to increase the photon flux and thus the measurement signal or to spare the target [129]. Conversely, it is of course also possible to adjust the MTF of the detector to that of the x-ray source by binning the pixels in order to increase the signal on the respective pixels without having to accept losses in spatial resolution.

2.2.2 Metrological Resolution

In addition to the structural resolution, another parameter is considered to be a core parameter for spatial resolution, especially in the metrological application of x-ray computed tomography, as well as other optics in general: the metrological resolution. The metrological resolution defines the possible step size when determining the position of a structure in the image. Consequently, there is a high correlation between the metrological resolution and the structural resolution. However, the metrological resolution is often significantly higher than the structural resolution of a system due to the subpixeling or subvoxeling techniques mentioned previously (see Sec. 2.1.6). Since the focus of this work is to increase the image quality of CT volume data and not, for example, on improving subvoxeling algorithms, in the following the structural resolution will be used as a measure for the spatial resolution of a CT dataset and the terms resolution, spatial resolution and structural resolution will be used as synonyms for the structural resolution of the image data.

2.3 Measurement Deviations in X-Ray Computed Tomography

The spatial resolution discussed above corresponds to an important feature of image quality in x-ray computed tomography. Another important factor for an optimal quality of a CT dataset is to keep disturbances due to various measurement deviations as low as possible. In addition to statistical measurement deviations, which occur as a random deviation of the measured value from the expectation in every measurement, there are a number of systematic measurement deviations in CT measurements, which sometimes significantly degrade the image quality. In CT imaging, these measurement deviations are also referred to as artifacts. Statistical and systematic measurement deviations depend on the measurement system, the properties of the measured object, and the acquisition parameters and they can greatly reduce the diagnostic value of CT image data and can severely falsify volume segmentations and associated dimensional determinations or make them completely impossible.

Statistical and some of the most prominent systematic measurement deviations occurring in CT measurements are described below. Among the systematic measurement

deviations, beam hardening and scatter artifacts are discussed with a particular focus, as methods to reduce these artifacts are presented within the scope of this work.

2.3.1 Statistical Measurement Deviations

Statistical measurement deviations occur in every measurement and thus each CT scan and the signal measured in each detector pixel deviates from the expectation value of the signal due to such statistical deviations, resulting in noisy measurement data. This noise can be divided into two effects: Quantum noise and electronic noise. While the quantum noise, which occurs due to the stochastic interactions in the emission and absorption or scattering processes of the x-ray quanta, is characterized by a correlation with the used amount of x-ray quanta and thus the x-ray intensities, the electronic noise, which results from thermal noise of the electrical signal in the detection process, is independent of the irradiated x-ray intensity. In CT, however, one usually only considers quantum noise, since even for measurements with extremely low x-ray intensities the electronic noise plays a rather minor role compared to the quantum noise of the detected photons [130].

The number of detected x-ray photons follows a Poisson distribution [15], [16]. Thus, the variance of the number of detected x-ray photons is equal to its expectation value $\langle N \rangle$:

$$\sigma_N^2 = \langle N \rangle \tag{2.45}$$

In order to determine the noise in the reconstructed CT volume from this, the influence of logarithmizing, as well as filtering and backprojection, must be taken into account. Since the noise of the x-ray intensities in the detector pixel depends on the number of transmitted photons, which in turn is defined in particular by the shape and composition of the scanned object, the derivation of an analytical expression for the noise in the CT image is not trivial. Using a ramp filter and using the simplifying assumption of a homogeneous cylindrical object, the noise of the central image pixel is [16]

$$\sigma_\mathrm{f}^2 \propto \frac{1}{N_\mathrm{a} \langle N_0 \rangle \, du^3} \,, \tag{2.46}$$

where N_a corresponds to the number of projections in the CT scan, $\langle N_0 \rangle$ represents the average number of transmitted x-ray photons of the central beam, and du describes the detector pixel size. Consequently, the image noise decreases with more projections, a higher photon count, and larger detector pixels, which is quite intuitive, since all these parameters improve the statistics of the cumulative signal.

An important measure for quantifying image quality with regard to statistical measurement deviations is given by the signal-to-noise-ratio (SNR). The SNR is defined by the quotient of the mean value and standard deviation of a signal:

$$\mathrm{SNR} = \frac{\mu}{\sigma} \tag{2.47}$$

With the above equations it can be easily understood that the SNR for CT measurements increases proportionally to the square root of the transmitted photons. Therefore,

doubling the SNR can be achieved by quadrupling the number of x-ray quanta, which can be achieved, for example, by increasing the measurement time by a factor of four. In CT volume data, the SNR is usually evaluated in a homogeneous region of interest (ROI) of the material or tissue of interest.

In order to distinguish anatomical structures from different tissue types or to accurately determine interfaces between materials, a high contrast is required in addition to a high SNR. Therefore, the contrast-to-noise-ratio (CNR) is often specified in CT datasets, which puts contrast and noise in different material areas in relation to each other:

$$\mathrm{CNR} = \frac{|\mu_1 - \mu_2|}{\sqrt{\sigma_1^2 + \sigma_2^2}} \tag{2.48}$$

The CNR can be calculated similarly to the SNR using ROIs in the CT image, where instead of one ROI, two ROIs are needed in two different material regions.

2.3.2 Systematic Measurement Deviations due to Polychromatic X-Ray Radiation

One source of systematic deviations in CT is the combination of the polychromatic x-ray spectrum and the energy-dependent attenuation of x-rays in matter. While low-energy photons have a high interaction probability with matter, this interaction probability decreases for increasing photon energies (see Sec. 2.1.2). As a result, the mean energy of the polychromatic x-ray spectrum shifts toward higher energies as it passes through the measured object (cf. Fig. 2.5), which has the effect of a reduced attenuation of x-rays at greater penetration depths in the object. Compared to the monochromatic projection values p, which correspond to the line integral of the linear attenuation coefficients μ (Eq. (2.21)) and can theoretically be transferred error-free into an object image by the filtered backprojection according to equation (2.24), the actually reconstructed polychromatic projection values q (Eq. (2.20)) thus show systematic deviations towards lower values. The exact size of these deviations depends on the x-ray spectrum as well as on the penetration lengths and material composition of the measured object. In CT imaging, the image artifacts generated by these systematic deviations are referred to as beam hardening artifacts, which is terminologically based on the increase of the mean energy of the x-ray spectrum, which is also referred to as hardening of the spectrum.

Figure 2.9 shows a graphical illustration of the effect of beam hardening and the resulting artifacts in the reconstructed volume using simulated tomography of a compressor wheel. The high-energy portion of the x-rays is shown in this figure as a blue bar whose strength barely decreases, while the red bar, representing the low-energy x-ray portion, almost completely disappears when the object is penetrated. As can be seen in the figure, beam hardening artifacts lead to brighter peripheral areas with simultaneously dark interior areas in the reconstructed volume. This type of image artifact is referred to as cupping. Another typical appearance of beam hardening artifacts consists of dark streaks connecting strongly absorbing structures in the transmission direction. This type of image artifact is referred to as streak artifact. The deviations due to beam hardening

artifacts can lead to severe discrepancies of the gray values and can significantly reduce the image contrast in certain areas, which may partially make structures in the CT images unrecognizable. In addition, surface information calculated from the volume data is distorted, which is expressed, for example, by incorrect surface positions [13] or holes in the surface model, as can be seen in Figure 2.9.

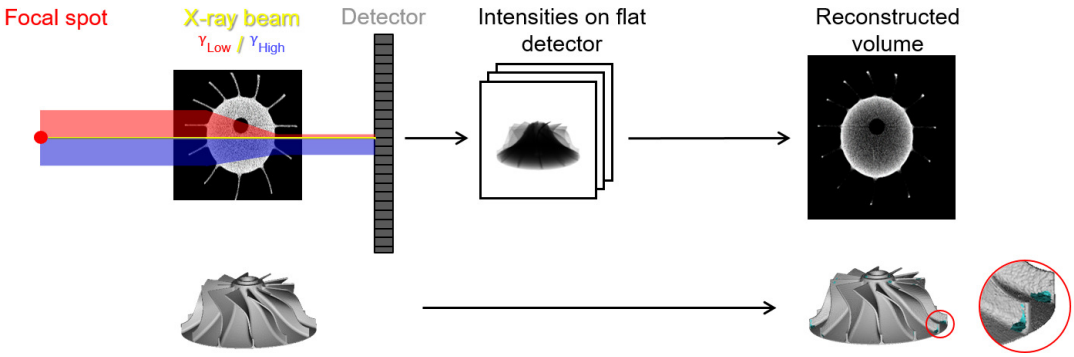

Figure 2.9: Schematic illustration of measurement deviations due to the polychromatic x-ray spectrum for a tomography of a compressor wheel. The upper row shows on an exemplary axial volume slice how high (blue) and low energetic components (red) of the x-ray beam are attenuated differently within the object and how this affects the reconstructed volume. In the lower part of this figure the surface models are shown from volume data without these deviations (left) and data with beam hardening artifacts (right).

2.3.3 Systematic Measurement Deviations due to Scattered Radiation

Another systematic deviation that may strongly reduce the image quality in CT, is caused by scattered and subsequently detected x-ray photons in a measurement. According to section 2.1.2, two photon matter interactions lead to scattering events of x-ray photons: Rayleigh and Compton scattering. In particular, scattering plays a major role for high-energy x-ray photons, since Compton scattering corresponds to the dominant photon matter interaction for high photon energies in the x-ray energy range used for CT. Although the cross-section of Rayleigh scattering for the photon energies relevant in CT is comparatively small (cf. Fig. 2.4), the fact that Rayleigh scattering is strongly forward directed means that the probability of the scattered photon hitting the detector is relatively high. Therefore, Rayleigh scattering should not be disregarded when considering scattered radiation in CT [94]. After all, a problem due to scattered x-ray photons arises in CT imaging only when the scattered photon hits a detector pixel and generates a disturbance signal there. If scattered photons hit detector pixels that are used to reconstruct image areas other than the photons original beam path, this results in a non-linear distortion of the intensity profile of the transmitted x-rays. Due to the scatter-induced signal I_S the reconstructed projection value is no longer given by

equation (2.20), but is described by

$$q = -\ln(\underbrace{I_\mathrm{P}}_{\text{Primary}} + \underbrace{I_\mathrm{S}}_{\text{Scatter}}) = -\ln\left(\int dE\, w(E)\, e^{-\int \mu(\boldsymbol{s}+\lambda\boldsymbol{t},E)\, d\lambda} + I_\mathrm{S}\right) \tag{2.49}$$

where I_P is used here for the transmitted unscattered x-ray intensities instead of τ from equation (2.20), since one generally classifies the measured x-ray intensities into primary and scatter components. This deviation of the measured projection values results in image artifacts in the reconstructed volume, which are commonly known as scatter artifacts in CT. According to the above equation, scattered radiation leads to an increase of the measured x-ray intensities similar to beam hardening, although the underlying physical effects are completely different. In contrast to beam hardening, however, scattered radiation corresponds to a low-frequency signal in intensity domain[3].

Using the same object on which the effect of beam hardening was shown before, Fig. 2.10 schematically shows a scattering process. Furthermore, simulated primary and scatter intensities are demonstrated for a flat detector, and a CT image and surface model of the reconstructed volume with scatter artifacts are shown. Qualitatively, the resulting image artifacts due to scattered radiation are similar to those due to beam hardening, although there are differences in detail. As can be seen in the figure, cupping also occurs due to scattered radiation. Streak artifacts can be observed, as well. Similar to beam hardening, scattered radiation can also lead to such a strong reduction of the image contrast that structures in the image become unrecognizable. It should be noted, however, that in the case of scatter artifacts, it is not so much the absolute value of the measurement deviation I_S that is decisive for the strength of the image artifacts, but rather the relative proportion of scatter intensities, the so-called scatter-to-primary-ratio (SPR):

$$\mathrm{SPR} = \frac{I_\mathrm{S}}{I_\mathrm{P}} \tag{2.50}$$

In local areas of high attenuation the SPR may easily yield values larger than one.

Even though scatter artifacts may occur in any CT scan and geometry, CBCT is particularly prone to this type of artifacts because scattered radiation from two spatial directions affects the measurement result.

Besides scattered radiation induced by the object, which is referred to as object scatter, there are other sources of scatter signals in a CT system, such as the tube housing and collimator [131], the prefilter [132], or the x-ray detector itself or its enclosure [133]. Even though these types of scatter may have different intensities or distributions compared to object scatter, they are conceptually equivalent to the artifacts described above.

[3] It should be noted that the scattered radiation signal has a low spatial frequency only in intensity domain, thus before the logarithmization of the projection.

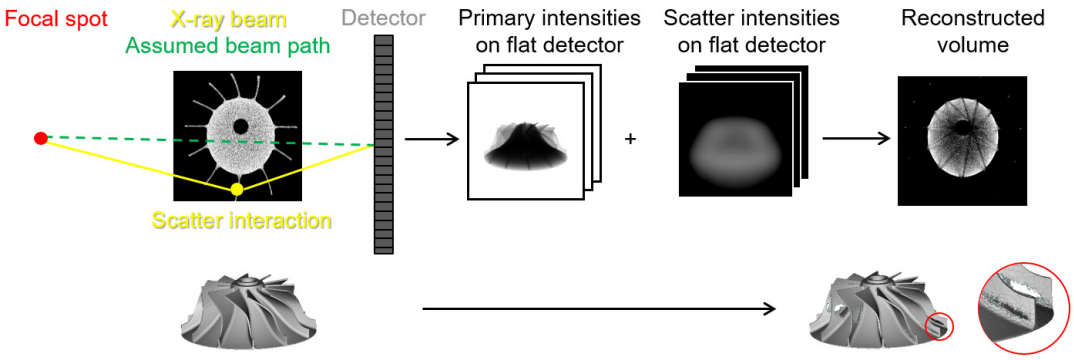

Figure 2.10: Schematic illustration of measurement deviations due to scattered x-ray photons for a tomography of a compressor wheel. Whilst in the upper part of this figure the process of scattering, resulting scatter and primary intensities on a flat detector, and the effects of scattered radiation on CT volume data are exemplarily shown, the lower part of this figure shows the effects of scatter artifacts on the surface models generated from such volume data.

2.3.4 Other Systematic Measurement Deviations

i.) Partial Volume Effect

Systematic measurement deviations may also arise due to the sampling of a continuous signal function with discrete x-ray detector elements. Such deviations may occur if the object structure changes within the width of the discrete detector element. Due to the logarithmization of the measured x-ray intensities, the projection value for a detector pixel covering an object edge is not linearly related to the part of the edge that the projection of the edge covers on the detector pixel. As such a linearity of the projection value is assumed in the reconstruction, this results in systematic measurement deviations in the reconstructed image, which are expressed by streaks along the reconstruction path of such an inconsistent projection value. One refers to this kind of systematic measurement deviation as linear or non-linear partial volume artifacts. The strength of these artifacts depends on the change in the projection signal due to the object edge and is therefore more pronounced for highly attenuating object edges.

ii.) Metal Artifacts

Especially in clinical CT the term metal artifacts is often used to refer to measurement deviations in the CT images caused by metals in the examined patient. Metal artifacts are, however, not an independent source of measurement deviations but rather reflect a combination of the aforementioned beam hardening, scatter, and partial volume artifacts and noise. These deviations are very distinct for highly attenuating objects in a measurement, such as metals, because such objects induce considerable spectral

shifts, cause a low photon statistics at high SPRs, and typically consist of sharp, highly attenuating edges. Sometimes the attenuation by metallic objects can be so high that no radiation reaches the detector at all. In this case one speaks of photon starvation. The missing projection data must then be interpolated, which also results in image artifacts.

iii.) Further Systematic Measurement Deviations

Other systematic measurement deviations can be caused by the distinct components of a CT system. For example, electrons scattered in the target material of the x-ray tube provide radiation components emitted outside the focal spot of the tube, so-called off-focal radiation, which produces further deviations from ideal x-ray imaging. Also the x-ray detector can cause systematic measurement deviations. If not properly corrected, transmission errors of the detector pixels generate ring-shaped sham structures in the reconstructed image, so-called ring artifacts. Furthermore, if the decay time of the light signal in indirect converting detectors is too large, this detector afterglow effect causes artifacts, as well. Even an imprecise rotary stage causes artifacts in CT imaging, since the motion during acquisition blurs x-ray projections and reconstructed volume data.

For further systematic measurement deviations references [15], [16] and [17] provide a good overview.

2.4 Dual Energy X-Ray Computed Tomography

Having discussed the setup of a CT system and the physical interactions associated with a CT measurement, as well as the various influences on image quality, a special measurement method, dual energy computed tomography (DECT), will be introduced and motivated at this point.

As described in the previous chapters, CT is used to reconstruct linear attenuation coefficients μ of an object. The attenuation coefficient depends on the material and density of the object in the respective image region (cf. Eq. (2.6)). For example, different materials with different densities may have the same gray value in a CT image. The primary goal of DECT is to resolve this ambiguity and obtain information about the exact material distributions and concentrations in a volume. However, as will be shown below, DECT can also be used to reduce systematic measurement errors due to the polychromatic x-ray spectrum. To achieve this, DECT takes advantage of the different energy dependence of the photon-matter interactions mainly involved in CT, the photoelectric effect and the Compton effect. The mass attenuation coefficient $\mu(E)/\rho$ can be decomposed into Compton and photoelectric interactions according to equations (2.5) and (2.6) neglecting Rayleigh scattering, which hardly contributes to the total attenuation [134]. Analogously, the mass attenuation coefficient of any material can be formulated as a linear combination of two so-called basis materials [135] assuming that the energy lies above the K-edge of the material

$$\frac{\mu(E)}{\rho} = a_1 \frac{\mu_1(E)}{\rho_1} + a_2 \frac{\mu_2(E)}{\rho_2}\,, \tag{2.51}$$

where $a_{1/2}$ describe weighting coefficients of the basis materials. Since DECT intends to compute two unknowns, the corresponding proportions of the basis materials in a respective voxel, two independent pieces of information must be available for each data point. Therefore, in DECT the same sample is measured twice with two different tube spectra, allowing equation (2.51) to be resolved according to the respective proportions of the basis materials.

For projection values of a sample consisting of two materials with the respective intersection lengths l_1 and l_2 and which otherwise differ only in their recording spectra, the following formulas hold true when scattered radiation is neglected:

$$\begin{aligned} q_{\mathrm{L}} &= -\ln\left(\int dE\, w_{\mathrm{L}}(E)\, e^{-\int \mu(\boldsymbol{s}+\lambda\,\boldsymbol{t},E)\,d\lambda}\right) = -\ln\left(\int dE\, w_{\mathrm{L}}(E)\, e^{-\mu_1(E)\,l_1-\mu_2(E)\,l_2}\right) \\ q_{\mathrm{H}} &= -\ln\left(\int dE\, w_{\mathrm{H}}(E)\, e^{-\int \mu(\boldsymbol{s}+\lambda\,\boldsymbol{t},E)\,d\lambda}\right) = -\ln\left(\int dE\, w_{\mathrm{H}}(E)\, e^{-\mu_1(E)\,l_1-\mu_2(E)\,l_2}\right) \end{aligned} \tag{2.52}$$

In these equations, $w_{\mathrm{L}}(E)$ represents a normalized low-energy spectrum and $w_{\mathrm{H}}(E)$ represents a normalized high-energy spectrum. To obtain the material intersection lengths l_1 and l_2 from the measured projection values q_{L} and q_{H}, Eq. (2.52) can be inverted by the polynomial representation [59]

$$l_i(q_{\mathrm{L}}, q_{\mathrm{H}}) = \sum_{m,n} c_{imn}\, q_{\mathrm{L}}^m\, q_{\mathrm{H}}^n\,. \tag{2.53}$$

The coefficients c_{imn} of this polynomial may be determined, for example, by calibration measurements [136].

Analogously, the projection values $q_{\mathrm{H,L}}$ can be mapped by a polynomial via the material intersection lengths l_1 and l_2

$$q_{\mathrm{j}}(l_1, l_2) = \sum_{m,n} k_{jmn}\, l_1^m\, l_2^n\,, \tag{2.54}$$

where the linear terms of this series expansion correspond to beam hardening artifact-free data and the nonlinear terms are responsible for beam hardening artifacts [58]. By reconstructing the monochromatic projection value

$$p = \mu_1(E_0)\, l_1 + \mu_2(E_0)\, l_2 \tag{2.55}$$

calculated from the material intersection lengths l_1 and l_2 for the basis materials μ_1 and μ_2 at a certain energy E_0, one obtains volume data which are per se free of beam hardening artifacts. CT images generated in this way are referred to as virtual monochromatic images. Alternatively, any linear combination of the two summands from Eq. (2.55) or each individual basis material projection value can be reconstructed to obtain artifact-free basis material images.

2.4.1 Image-Based Dual Energy X-Ray Computed Tomography

The combination of two spectral CT datasets for generating virtual monochromatic images or material decomposition is also possible in image domain. However, in image domain combinations typically correspond to linear operations of the volume data acquired with a low-energy spectrum f_{L} and a high-energy spectrum f_{H}. Therefore, for the mixed image holds [137]

$$f_{\mathrm{DECT}}(x,y,z) = \alpha\, f_{\mathrm{L}}(x,y,z) + (1-\alpha)\, f_{\mathrm{H}}(x,y,z)\,, \tag{2.56}$$

where α corresponds to the linear weighting factor, also called blending factor, which can be determined for material decomposition, for example, by calibration measurements. Hence, combinations of spectral data as proposed by Eq. (2.56) are also known as alpha blending.

Besides material decomposition, Eq. (2.56) can be used for image quality improvements, as well. Depending on the choice of the linear blending factor α the fusion volume $f_{\mathrm{DECT}}(x,y,z)$ may have different properties regarding image quality. For $\alpha \in (0,1)$ it is possible to create noise-reduced or CNR-maximized fusion volumes and setting $\alpha < 0$ can lead to a reduction of beam hardening artifacts in the fusion volume, which is described below.

i.) Pseudo-Monochromatic Imaging

Since image reconstruction corresponds to a linear process, the linear combination according to Eq. (2.56) is equivalent to a linear combination of the dual-energy projection data q_{L} and q_{H} with a subsequent reconstruction. According to equation (2.54), q_{L} and q_{H} can be expressed by a polynomial series expansion of the material intersection lengths l_i, where the nonlinear terms of this series are responsible for beam hardening. By a suitable choice of the blending factor α it is therefore possible to minimize the influence of these terms and thus to reduce beam hardening artifacts in the image [59]. With this technique, also known as alpha blending, not only beam hardening artifacts but also scatter artifacts can be partially concealed. Thus, linear blending using Eq. (2.56) can also be used to reduce metal artifacts [58]. However, this method provides artifact-reduced data only for a certain value of α, which, as mentioned above, is at values less than zero, and beam hardening-free CT images cannot be generated at arbitrary monochromatic energies, as is the case with rawdata-based virtual monochromatic imaging. Therefore, this method is also referred to as pseudo-monochromatic imaging [58]. The optimal choice of the blending factor for pseudo-monochromatic imaging cannot be described analytically. Since it is only one optimization parameter, optimization can relatively simply be done by visual inspection. Alternatively, optimization algorithms in combination with properly chosen cost functions, such as a locally defined total variation [58] or the mean squared error (MSE) with respect to a homogeneous segmentation, can allow an automatic determination of the optimization parameter α.

Even though the pseudo-monochromatic imaging described above is only an approximate solution for the theoretically exact rawdata-based polynomial combination in

Eq. (2.53) and therefore theoretically worse performance for the reduction of beam hardening artifacts is to be expected, it is nevertheless frequently used in DECT. One reason for this is that theoretically accurate rawdata-based data fusion is not necessarily superior in practical applications after all [138] and the calibration with respect to multiple parameters and their optimization poses a more difficult problem than the single parameter calibration and optimization performed in pseudo-monochromatic imaging. Another reason is that for some measurement methods for obtaining dual-energy data, the rawdata coverage required for Eq. (2.53) is not provided. In particular, this is the case for dual source systems in which a pair of tubes and detectors simultaneously acquires approximately orthogonal projection data in a gantry setup. Dual source systems offer the advantage that the spectral separation in such systems is usually very good due to the possible use of different voltages and prefiltration at both x-ray tubes, and a good spectral separation of the data is advantageous for the methods described above [139]. In industrial DECT one therefore usually performs sequential scans of the workpiece with different spectra.

However, as mentioned above, pseudo-monochromatic imaging has the disadvantage that beam hardening artifacts are reduced only for a certain value of the blending factor $\alpha < 0$. This leads to the fact that the statistical measurement deviations in the volume data, thus the noise in the CT images, are increased for the fusion volume $f_{\mathrm{DECT}}(x, y, z)$ compared to both input images, which also implies decreased CNRs. The reason for this is the negative value of the artifact minimizing linear factor α, given that the noise of the fusion volume $\sigma(f_{\mathrm{DECT}}(x, y, z)) = \sigma(f_{\mathrm{DECT}})$ results from:

$$\sigma(f_{\mathrm{DECT}}) = \sigma(\alpha\, f_{\mathrm{L}} + (1-\alpha)\, f_{\mathrm{H}}) = \sqrt{\alpha^2\, \sigma(f_{\mathrm{L}})^2 + (1-\alpha)^2\, \sigma(f_{\mathrm{H}})^2} \tag{2.57}$$

This equation holds true if the noise in the images f_{L} and f_{H} is not correlated, which is the case for most DECT techniques, especially for sequential scan operation modes.

ii.) Reduction of Statistical Measurement Deviations

From equation (2.57) it is clear that linear blending using Eq. (2.56) can also be used to reduce noise in the combination volume. By minimizing the variance of the combination image $\sigma(f_{\mathrm{DECT}})^2$ with respect to α one obtains:

$$\begin{aligned} \frac{\partial}{\partial \alpha} \sigma(f_{\mathrm{DECT}})^2 &= 2\,\alpha\, \sigma(f_{\mathrm{L}})^2 + 2\,\alpha\, \sigma(f_{\mathrm{H}})^2 - 2\, \sigma(f_{\mathrm{H}})^2 \stackrel{!}{=} 0 \\ \rightarrow \alpha &= \frac{\sigma(f_{\mathrm{H}})^2}{\sigma(f_{\mathrm{L}})^2 + \sigma(f_{\mathrm{H}})^2} \end{aligned} \tag{2.58}$$

The variance in the high and low energy volume data needed to solve for α can be obtained by evaluating the noise in a homogeneous ROI, as described in section 2.3.1.

Similarly, an analytical expression can be found for the blending factor that maximizes the CNR in the combination image

$$\alpha = \frac{C_{\mathrm{L}}/\sigma(f_{\mathrm{L}})^2}{C_{\mathrm{L}}/\sigma(f_{\mathrm{L}})^2 + C_{\mathrm{H}}/\sigma(f_{\mathrm{H}})^2}\,, \tag{2.59}$$

where $C_{\mathrm{H/L}} = |\mu_{\mathrm{H/L},1} - \mu_{\mathrm{H/L},2}|$ denotes the contrast between two materials of high and low energy volumes, respectively. By considering the two equations above, it is also clear that for the blending factor $0 < \alpha < 1$ must hold, so that the DECT volume has a reduced noise level or a maximized CNR.

In summary, DECT allows both, the quantitative analysis of the material composition of the measured object and the optimization of image quality in terms of beam hardening or noise artifacts.

3 Novel Method for the Reduction of Systematic Measurement Deviations in X-Ray Computed Tomography due to Scattered X-Rays using the Empirical Scatter Correction

Scattered radiation induced by Compton or Rayleigh scattering generates a non-linear perturbation signal on the measured primary intensities. This perturbation signal is superimposed by other physical processes that affect the measured intensities, such as beam hardening for instance. In contrast to beam hardening, scattered radiation is a low-frequency artifact in intensity domain, which means that, apart from noise effects, the scatter intensities correspond to a smooth distribution. If, in addition to scattered radiation, beam hardening is to be corrected in a measurement by using spectral information, e.g. by virtual monochromatic or pseudo-monochromatic imaging, it is useful to have already removed the scattered radiation as far as possible from the underlying datasets. Otherwise, the distortion of the measured intensity values induced by scattered photons may interfere with the estimation of the optimization parameters (Eqs. (2.53) and (2.56)) and thus produce a bias on their value. For this reason, the reduction of systematic deviations due to scattered radiation is treated first in this work and takes place before further artifact corrections such as beam hardening correction (Sec. 4 and 5) or noise reduction (Sec. 6).

Because a wide range of measurement objects and acquisition parameters must be covered for industrial CT, the scatter correction method proposed here is intended to provide straightforward and universal applicability. For this purpose, it should fulfill the following conditions:

– No hardware modification of the CT device or additional measurements should

be required; the method should correspond to a software-based post-processing correction method.

- Prior knowledge about the measured object should not be required, i.e. no exact knowledge about material or density shall be necessary. Thus, the correction of the CT measurement is independent of the manufacturing information of the workpiece.
- Prior knowledge about the spectrum and CT system used for the measurement should not be required. This way the correction can universally be used and transferred to less well known CT systems, even if significant information about the measurement like the tube voltage, prefiltration, used detector, etc. are not accessible.
- The method should be usable even in the presence of strong artifacts.
- Preferably, it should be possible to correct not only object scatter but also other artifacts that can be approximated as low-frequency perturbations of the measured intensities. In particular, backscatter from the detector and the detector housing as well as scattered radiation from the collimator or prefilter, if present, should be reduced in addition to object scatter.

Therefore, the empirical scatter correction (ESC) was developed for the reduction of systematic deviations due to scattered radiation. ESC offers a method to efficiently remove low-frequency perturbations, such as scattered radiation, from CBCT scans without prior knowledge and was tested on simulated data, as well as measured CBCT data from various CT systems for clinical and industrial applications. The functional principle of ESC is described in more detail below.

3.1 Material and Methods

3.1.1 Functional Principle of the Empirical Scatter Correction

i.) Basic Idea of the Correction Procedure

The empirical scatter correction approximates the intensities induced by scattered photons within a measured intensity projection $I(u, v, \alpha)$ by a linear combination of different scatter estimates, so-called basis images. To obtain scatter-reduced intensity projections $I_{\mathrm{cor}}(u, v, \alpha)$, this linear combination of basis images $\sum_i c_i \cdot B_i(u, v, \alpha)$ is subtracted from the measured scatter-affected intensities:

$$I(u, v, \alpha)_{\mathrm{cor}} = I(u, v, \alpha) - k_\alpha \sum_i c_i \cdot B_i(u, v, \alpha) \tag{3.1}$$

with

$$k_\alpha = \begin{cases} \min \frac{I(u,v,\alpha)}{\sum_i c_i \cdot B_i(u,v,\alpha)} (1 - \delta) & \text{if } \min \left(I(u, v, \alpha) - \sum_i c_i \cdot B_i(u, v, \alpha) \right) < 0 \\ 1 & \text{else} \end{cases} \tag{3.2}$$

The pixel indices of the flat detector are given by u, v in these equations and α denotes the rotation angle of the respective projection. The factor k_α is used to constrain the scatter estimate to be smaller than the measured intensities for each pixel in each projection for the empirically chosen value of $\delta = 10^{-5}$. Thereby k_α avoids the occurrence of negative intensity values in the corrected data, which would be unphysical. In principle, ESC does not impose any particular restrictions on the the basis images besides that they must be constrained to smooth, low-frequency signals such that they are able to model the low-frequency scatter artifacts that need to be removed sufficiently well. They can either be calculated from the projection data or represented by more or less arbitrary low-frequency signals, such as constant projections. A detailed description on the generation of the basis images, which are used for the ESC results shown here (Sec. 3.2), is given in the following subsection.

The empirical scatter correction algorithm optimizes the the coefficients c_i for a given set of basis images such that the corrected data contain as few scatter artifacts as possible. In contrast to the subtraction of scatter signals, which is physically correctly performed in intensity domain by the equation above, this optimization process takes place in the reconstructed volume, thus in image domain where the artifacts can severely deteriorate the image quality and may inhibit diagnosis, inspections and correct segmentations of CT volumes in medical and industrial CT applications. To do so, the corrected intensities from Eq. (3.1) need to be logarithmized and filtered backprojected. This procedure has the disadvantage to be quite time consuming, especially if an algorithm needs to optimize various parameters in an iterative manner, which involves repeated reconstructions. In order to avoid these long computation times, ESC uses a known trait about the scatter artifacts it needs to model: As the subtraction in Eq. (3.1) is performed in intensity domain, the empirical scatter correction process can be performed on subsampled projections. This is possible because, as mentioned above, scatter is a low-frequency signal in intensity domain and can therefore be estimated on subsampled projections with almost no loss of information.

The first step of the ESC algorithm is therefore given by a bilinear downsampling of the measured projection data. Besides this bilinear downsampling, the number of projections is also reduced to cover only every 2° because the scatter signal is smooth in angular direction, as well. After this, an initial reconstruction of the downsampled projection data is performed. This reconstruction, as well as all reconstructions in the following parameter optimization step are performed using the filtered backprojection algorithm with a smooth reconstruction kernel on a smaller voxel grid, which was done to avoid sampling artifacts and impacts of image noise on the optimization process, and to reduce computation time. This initial reconstruction is then segmented with the algorithm of Otsu [112] to obtain a binary air mask and another binary mask that contains a segmentation of the main material of the scanned object, e.g. soft tissue for a patient or the material of interest in a scanned workpiece. These masks are necessary for the following parameter optimization step.

The parameter optimization corresponds to the actual core process of ESC. In order to find the optimal coefficients c_i to represent the scatter signal with the linear combination of the basis images, a Nelder-Mead algorithm [140] is used. After the coefficients c_i are

initialized at small positive values, the Nelder-Mead downhill simplex algorithm searches for those coefficients that yield the minimal cost function value. For each iteration a reconstruction of the downsampled projection data on the small reconstruction grid is performed. The cost function of the optimization process corresponds to the MSE between the volume, which is linearly weighted with another optimization parameter c_I, and a reference CT value within the previously segmented air and material regions. This reference CT value corresponds to $-1000\,\mathrm{HU}$ per definition for the segmented air regions and to a reasonable CT value for the selected material, e.g. $0\,\mathrm{HU}$ for water-equivalent matter, $55\,\mathrm{HU}$ for muscle tissue [141], or another value that can for instance be determined by a human observer in a relatively artifact free region of the material of interest within the initially reconstructed volume. The volume weighting factor c_I guarantees that in case of faulty calibration of the data or, to be more general, in cases where the CT values are off for some reason, the algorithm automatically accounts for such an offset and does not try to incorporate it in the scatter estimate. This coefficient is initialized near the value of one. ESC thus optimizes the coefficients c_i and c_I such that the reconstruction of the corrected intensities from Eq. (3.1) yields a CT volume with a homogeneous gray value distribution in the previously segmented air and material areas of this volume. To avoid unphysical negative scatter estimates, the coefficients are limited to positive values during the optimization. It was observed that 200 iterations of the Nelder-Mead algorithm with typical inherent parameter values (reflection=1, expansion=2, contraction=compression=1/2) yield sufficient results.

Once the optimization process is finished and the optimal coefficients are found, the final scatter estimate is bilinearly upsampled to the original projection size and missing projections in angular direction are linearly interpolated. Then this ESC scatter estimate is subtracted from the measured intensities as proposed in Eq. (3.1). A reconstruction of the corrected logarithmized intensities yields a scatter artifact-reduced volume.

An overview of the ESC process is given by the pseudocode in algorithm 1. Furthermore, Fig. 3.1 depicts the optimization process schematically.

In principle, the entire ESC process can be performed multiple times. This option provides the benefit that the initial segmentations that are used during the optimization process are improved after the data is scatter-corrected by a first iteration of ESC. One may also consider to perform subsequent iterations with less sparse data, meaning larger projection sizes and voxel grids, in order to target scatter artifacts that lead to spatially rather small distortions in image domain and are therefore missed on a sparser grid. As an approximate solution for the optimization parameters is already found at this point, the number of iterations for the parameter optimization can be reduced accordingly. However, performing ESC more than once negatively affects the computation times, of course. The results shown in section 3.2 are all acquired using a single iteration of the algorithm proposed here.

Algorithm 1 Pseudocode for the empirical scatter correction.

select subset of measured intensities and bilinear downsampling $I_{u,v,\alpha} \rightarrow I'_{u',v',\alpha'}$
initial reconstruction $X^{-1'}(-\ln(I'_{u',v',\alpha'}))$ on a small grid
generate binary soft tissue and air masks M'_{st} and M'_{air} from this reconstruction
compute basis images $B'_{u',v',\alpha',i} = f(I'_{u',v',\alpha'})_i$
for $n = 1$ to 200 **do**
    $k_{\alpha'} = \min(1, \min \frac{I'_{u',v',\alpha'}}{\sum_i c_i \cdot B'_{u',v',\alpha',i}}(1-\delta))$
    $p'_{u',v',\alpha'} = -\ln(I'_{u',v',\alpha'} - k_{\alpha'} \sum_i c_i \cdot B'_{u',v',\alpha',i})$
    $C = (c_{\text{I}}\, X^{-1'}(p') \cdot M'_{\text{st}} - \mu_{\text{target, st}})^2 + (c_{\text{I}}\, X^{-1'}(p') \cdot M'_{\text{air}} - \mu_{\text{target, air}})^2$
    optimize C w.r.t. c_i and c_{I}
end for
upsample basis images and interpolate missing projections $B'_{u',v',\alpha',i} \rightarrow B_{u,v,\alpha,i}$
correct original measured intensities using Eq. ((3.1))
reconstruction $X^{-1}(-\ln(I_{\text{cor},u,v,\alpha}))$

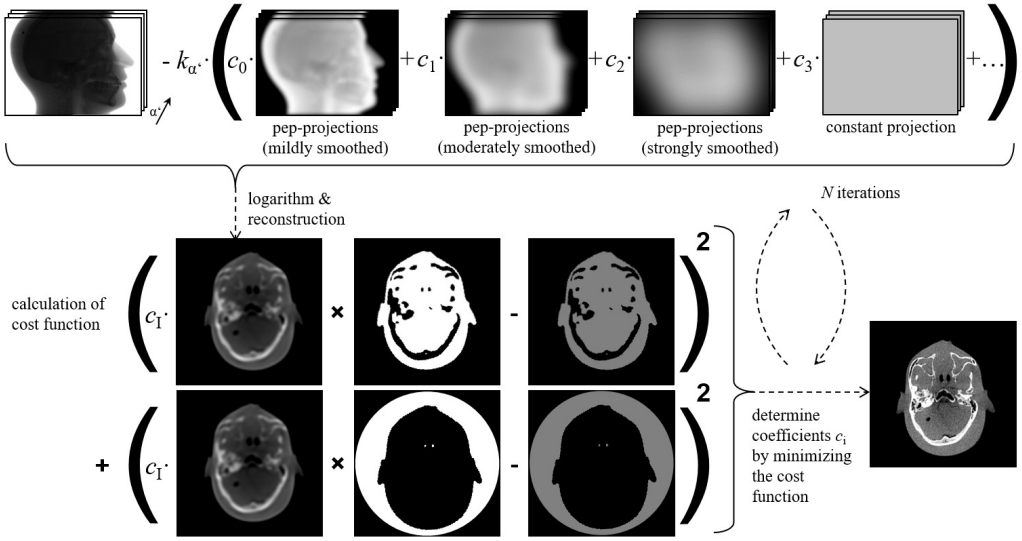

Figure 3.1: Workflow of the ESC scatter estimation on the example of a head phantom scan. Low frequency basis images (see Fig. 3.2) are linearly combined with the coefficients c_i and subtracted from the measured intensities. A cost function value, which is based on an MSE between the weighted air and material regions (here water-equivalent soft tissue) of the reconstructed corrected data and a respective reference gray value, is minimized iteratively by adjusting the coefficients c_i and c_{I} (cf. Alg. 1).

ii.) Scatter Model

As described in the previous section, the empirical scatter correction models the estimate of scatter artifacts and other signals that appear as low-frequency artifacts by a linear superposition of low-frequency basis images. Therefore, it is essential to use basis images which are able to jointly model the disturbing low-frequency intensity perturbations at least to an extent that the quality of the reconstructed data is sufficient.

Because one of the main goals of ESC is to have a scatter correction algorithm that can be used without specific prior knowledge, the basis images can not depend on such information. This excludes for instance sparse Monte Carlo simulations or forward projections of the segmented volumes using spectral information of the measurement. Of course such data can be added to the ESC basis images if sufficient prior information is available but this may not always be the case. This also includes novel learning-based approaches [27], [41] that require a trained model to be available.

Kernel-based scatter estimation approaches [94], [142]–[149] are well established in the field of CT and offer a method to model scatter solely based on the measured projections and mathematical operations on them such as convolutions. Typically these methods require detailed knowledge about the CT system and scan acquisition parameters in order to carefully set various empirical parameters. However, this is not a big problem for ESC. Different kernel-based scatter estimates with different sets of empirical parameters can be used as basis images and the ESC algorithm automatically determines optimal weightings of those to model the scatter in the measurement to be corrected.

The kernel-based model that was chosen to approximate the scatter intensities for ESC is a modification of the so-called pep-model, which was developed by Ohnesorge et al. several years ago [144]. Even though this model was initially proposed for clinical CT scanners with a single detector row, it was shown that it can effectively be used for scatter reduction in CBCT, as well [150]. The basic idea of this model is quite simple and will be briefly explained below.

As explained in section 2.1.2, the attenuation coefficient μ results from three types of interactions of x-ray photons with matter: the photoelectric effect, Rayleigh and Compton scattering. Only the latter two lead to scattering events and are therefore of importance for the scatter estimation. If a discretized volume is considered, the intensity of scattered radiation that emerges from a voxel i of size dl at position l_i in forward direction is therefore proportional to the intensity of x-ray photons at this voxel multiplied with the voxel's attenuation coefficient μ_i, which corresponds to the interaction probability of the photon and matter in this voxel. Expressed in an equation, the forward scatter intensity $dI_{\mathrm{S,\,f},\,i}$ emerging from voxel i can be written as

$$dI_{\mathrm{S,\,f},\,i} = K_{\mathrm{S,\,f}}\,\mu_i\,I_0\,e^{-\int_0^{l_i}\mu(\lambda)\,d\lambda}\,dl, \tag{3.3}$$

where $K_{\mathrm{S,\,f}}$ corresponds to a proportionality factor that here describes the differential scatter cross section for small scatter angles. With no loss of generality, the photoelectric effect and scatter interactions with large diffraction angles, which are included in the

attenuation coefficient μ_i, are compensated for with this proportionality factor $K_{\mathrm{S,\,f}}$. Furthermore, the energy dependence of the scatter interactions is disregarded in this equation. It therefore corresponds to a monochromatic approximation of the scatter intensities, e.g. at the spectrum's center energy. The scatter intensity emerging from voxel i that can be detected at an detector element corresponding to the considered ray behind an object of size L is subsequently given by

$$dI_{\mathrm{S,\,f},\,i} = K_{\mathrm{S,\,f}}\,\mu_i\,I_0\,e^{-\int_0^{l_i}\mu(\lambda)\,d\lambda}\,e^{-\int_{l_i}^{L}\mu(\lambda)\,d\lambda}\,dl. \tag{3.4}$$

Small scattering angles are assumed for the forward scatter here, so that the beam path between scattered and non-scattered photons does not differ in a first approximation. Therefore, this formula facilitates to

$$dI_{\mathrm{S,\,f},\,i} = K_{\mathrm{S,\,f}}\,\mu_i\,I_0\,e^{-\int_0^{L}\mu(\lambda)\,d\lambda}\,dl. \tag{3.5}$$

Integrating Eq. (3.5) over all voxels along the beam path where scatter events may take place results in the forward scatter intensity for this specific beam path:

$$I_{\mathrm{S,\,f}} = K_{\mathrm{S,\,f}}\,I_0\int_0^{L}\mu(\lambda)\,d\lambda\,e^{-\int_0^{L}\mu(\lambda)\,d\lambda} \tag{3.6}$$

This equation describes the weighted product of the measured intensity and the line integral for the considered ray. For a flat detector with pixel indices u, v this equation can thus be rewritten as

$$I(u,v)_{\mathrm{S,\,f}} = K_{\mathrm{S,\,f}}\,I(u,v)_{\mathrm{P}}\,(-\ln(I(u,v)_{\mathrm{P}})) \tag{3.7}$$

where $I(u,v)_{\mathrm{P}}$ depicts the primary intensity, which is approximated by the measured total intensity $I(u,v)$ in this model because the scatter intensity $I(u,v)_{\mathrm{S,\,f}}$ is considered to be negligible compared to the primary intensity. If $-\ln(I(u,v))$ is now identified with the projection value $p(u,v)$, the formula above reads $p(u,v)\,e^{-p(u,v)}$, which is the reason why this model is referred to as pep-model.

When instead of a single ray all rays that reach the detector are incorporated in the model, the total scatter distribution at a pixel must be obtained by a convolution operation on the forward scatter signals at each pixel with a specific scatter kernel. For ESC the total scatter signal is therefore modelled by

$$I(u,v)_{\mathrm{S}} = K(u,v)_{\mathrm{S}} * W(I(u,v))^m\,(-\ln(I(u,v)))^n \tag{3.8}$$

with

$$W(I(u,v)) = \begin{cases} I(u,v) & \text{if } I(u,v) < \epsilon \\ 0 & \text{else} \end{cases} \tag{3.9}$$

where $m\,, n$, and ϵ are empirical parameters that are already proposed in the original model by Ohnesorge et al. [144] for a higher correction accuracy and K_{S} corresponds

to the scatter convolution kernel. ESC simplifies the original model by choosing this kernel to be of truncated, symmetric Gaussian shape with different standard deviations σ. Thus, it reads:

$$K_{\mathrm{S}}(\boldsymbol{r}-\boldsymbol{r}') = e^{-\frac{(\boldsymbol{r}-\boldsymbol{r}')^2}{2\,\sigma^2}} \tag{3.10}$$

For the results presented in section 3.2, nine different pep basis images were used with a different set of parameters m, n, ϵ, and σ. An overview of these basis images is given in Fig. 3.2 for an exemplary projection of a head phantom scan. All nine pep basis image parameter sets were consistently used for the correction of the clinical and industrial datasets in the results section 3.2 without an additional fine-tuning of the parameters m, n, ϵ, and σ. Additionally to those pep basis images, a constant projection is used for the correction of each dataset to model constant offsets of the intensities over the whole detector image. For the correction of patient data that were measured with a shifted detector in a system employing a bowtie filter (see Fig. 3.9), an additional ramp-like basis image is used, which could approximate changes in the scatter signal due to this type of filter. Such a basis image can in principle also be used for the other corrections without bowtie filter but it would not be of any particular help there, which is why it was neglected for these datasets in the following.

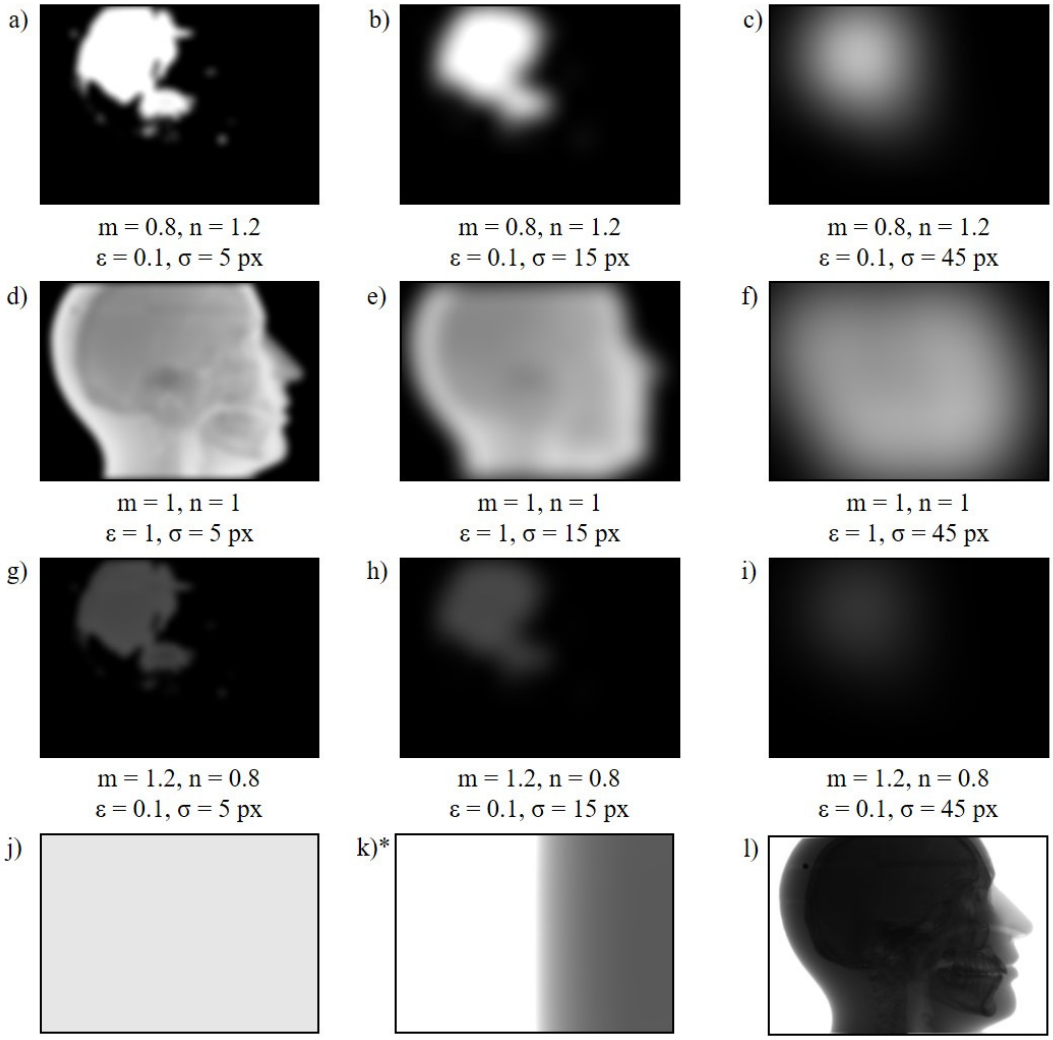

Figure 3.2: For an example projection of a head phantom scan l), the different basis images that were used for the empirical scatter corrections shown in section 3.2 are depicted by the images a)-k). Note that basis image k) is asterisked as it is only used for the correction of the patient data where a bowtie filter is used (see Fig. 3.9). Window a)-k): $C = 0.2$, $W = 0.4$. Window l): $C = 0.5$, $W = 1$.

3.1.2 Reference Method: Image-Based Empirical Scatter Correction

The empirical scatter correction proposed here is a further development of the empirical scatter correction, which was published by Meyer et al. [151]. This method also aims to reduce scatter artifacts based on basis images without precise prior knowledge of the CT scan or the scanned object, and is therefore suitable as a reference to the method presented here. In contrast to the ESC algorithm described above, however, the scatter estimate in Meyer's method is not physically correctly subtracted from the scatter-affected measured intensities in intensity domain. In this method the scatter artifacts are rather approximated by a reconstruction and subsequent linear combination of these scatter estimates in image domain

$$S_i = X^{-1}(s_i) = X^{-1}(-\ln(B_i + I) + \ln(I)), \tag{3.11}$$

where I denotes the measured intensities, i the scatter estimate index, B_i the scatter basis image in intensity domain, and X^{-1} the filtered backprojection operator. By subtracting a linear combination of different scatter estimates S_i from the uncorrected reconstructed volume $X^{-1}(-\ln(I))$, a scatter-corrected volume is generated. This procedure allows an optimization process that takes place purely in image domain. By avoiding iterative reconstructions, this method has an advantageous runtime over the ESC presented here. However, due to the physically incorrect approximation of correcting measurement data only after logarithmization and reconstruction, a lower correction quality is expected, which is also confirmed by the results in section 3.2.

In order to achieve the best possible comparability of the methods, the same basis images B_i and the same cost function were used for corrections with this reference method as for ESC. To avoid confusion with the here proposed ESC, the method from Meyer et al. is from now on referred to as image-based empirical scatter correction (ibESC) in this work.

3.1.3 Simulation Study

To verify how well ESC is suited to correct object scatter artifacts in CBCT, a simulation study was carried out. For this purpose, nearly scatter artifact-free clinical CT volume data[1] of a head, thorax and abdomen CT were forward projected in cone-beam geometry and a Monte Carlo simulation was used to generate realistic scatter signals for the simulated CBCT dataset. The Monte Carlo simulation used for this study came from an in-house library from the division of x-ray imaging and computed tomography at the German Cancer Research Center (DKFZ) [97], [150]. It uses an interpolation of the tabulated values from the evaluated photon data library (EPDL) [95] database to calculate the differential cross sections for scatter interactions and the overall attenuation of the x-ray photons. For the different body regions different anatomy-typical simulation

[1] Clinical CT acquisitions from multi-slice CT scanners typically exhibit a very low amount of scatter artifacts due to a smaller longitudinal coverage of the detectors compared to CBCT and large one- or even two-dimensional anti-scatter grids, which are installed on the detector to avoid the measurement of scattered radiation.

	Head	Thorax (shifted detector)	Thorax (truncated)	Abdomen (shifted detector)	Abdomen (truncated)
R_{FD}	1080 mm	1080 mm	1080 mm	1080 mm	1080 mm
R_{F}	855 mm	620 mm	620 mm	620 mm	620 mm
FOM	227 mm	414 mm	216 mm	414 mm	216 mm
Number of detector pixels	1024^2	1024^2	1024^2	1024^2	1024^2
Pixel size	0.388 mm	0.388 mm	0.388 mm	0.388 mm	0.388 mm
Number of voxels	$414 \times 414 \times 542$	512^3	512^3	512^3	512^3
Voxel size	0.6 mm	0.82 mm	0.82 mm	0.82 mm	0.82 mm
Steps (360°)	720	720	720	720	720
Scintillator thickness	0.6 mm	0.6 mm	0.6 mm	0.6 mm	0.6 mm
Tube voltage	80 kV	100 kV	100 kV	120 kV	120 kV
Prefilter thickness	6 mm	6 mm	6 mm	6 mm	6 mm

Table 3.1: Parameters for the simulations shown in section 3.2.1. The simulated scintillator material was caesium iodide and the prefilter material aluminum.

parameters and partly different acquisition geometries were used, which are shown in table 3.1. As is clear from this table, different scan trajectories were tested for the thorax and abdomen: In each case, one simulation was performed for a shifted detector scan in which the field of measurement (FOM) covers the complete patient and one simulation was performed with a centered detector which has a reduced FOM and thus results in truncated data. For the CT measurement of the head, only the centered detector acquisition geometry was simulated, since the FOM is sufficiently large to completely cover the head.

The simulation of the head measurement was additionally used for other experiments: It was tested, how well a Monte Carlo simulation is able to correct this dataset on the basis of the uncorrected volume data. This uncorrected volume contains distorted CT values due to the artifacts and therefore the material segmentation and density information needed for the Monte Carlo simulation is negatively affected. Furthermore, another Monte Carlo simulation is performed in which it was deliberately assumed that the tube voltage was 100 kV instead of the actual 80 kV. This experiment thus emulates a Monte Carlo simulation with non-exact parameters, as they could occur, for example, if there was no or incorrect prior knowledge about the actual measurement parameters.

3.1.4 Measured Data

In addition to simulations, ESC was also tested on various measurements from different CT scanners. Both, clinically relevant CBCT scans as well as industrial CBCT data were corrected using the empirical scatter correction. The capabilities of ESC were tested on two datasets for each of the different CT application fields, which are further specified below.

i.) Medical Cone-Beam Computed Tomography Data

A measurement of a semi-anthropomorphic head phantom that was performed on a table-top CBCT device, equipped with a Varian 4030 flat detector and a Hamamatsu microfocus x-ray tube, was used to evaluate the correction capability of ESC for measured medical CBCT data. Table 3.2 provides an overview of the scan parameters. A slit scan of this phantom, measured with the same scan parameters and in the same clamping, serves as almost scatter-free reference data for comparison. Furthermore, another reference dataset was acquired by measuring the phantom on a SOMATOM Definition Flash (Siemens Healthineers, Forchheim, Germany) clinical MSCT device, which similarly to the slit scan is less affected by scatter due to a narrower collimation compared to the CBCT scan and additionally employs large anti-scatter grids to avoid scatter artifacts. The latter measurement was performed using a radiation planning protocol at a tube voltage of 120 kV and a tube current-time product of 215 mAs. The projection data were reconstructed using filtered backprojection.

In order to test ESC on real patient data, CBCT data of a pelvis scan from a Varian Edge radiosurgery system (Varian, Palo Alto, USA) were corrected with ESC. For this patient data, ESC is compared to the built-in scatter correction algorithm from the iTools image reconstruciton toolkit, which corresponds to another kernel-based scatter correction algorithm according to reference [148]. Information regarding the scan parameters for this patient acquisition can be found in table 3.2.

Similarly to the simulations, the ibESC algorithm was tested on these datasets, as well, in order to compare the scatter reduction capability of ESC.

ii.) Industrial Cone-Beam Computed Tomography Data

The two corrections of industrial CBCT measurements that were performed concern on the one hand a measurement of a zinc die-cast plug housing at a TomoScope® L (Werth Messtechnik, Gießen, Germany) industrial CT device equipped with a 300 kV microfocus x-ray tube and on the other hand a measurement of an automotive controller measured at the Werth MultiSpek CBCT system with a 450 kV macrofocus tube. The latter CT device is described in more detail in chapter 4. While the zinc die-cast plug housing is mainly made of a single material zinc with a small plastic insert inside the connector, the automotive controller is a multi-material workpiece consisting of several metals and plastics, which makes it a challenging workpiece for CT measurements. However, the main component of the automotive controller is aluminum. Therefore, in this case, aluminum is the material that is segmented in the ESC process and on

	Head phantom	Pelvis (patient)
CBCT device	table-top	Varian Edge
R_{FD}	1035 mm	1500 mm
R_{F}	895 mm	1000 mm
FOM	238 mm	464 mm
Number of detector pixels	720×512	1020×764
Pixel size	0.388 mm	0.388 mm
Number of voxels	$384 \times 384 \times 384$	$512 \times 512 \times 210$
Voxel size	0.6 mm	1 mm
Steps (360°)	362	884
Tube voltage	120 kV	125 kV
Tube current	3 mA	80 mA
Tube power	360 W	10 000 W
Integration time	180 ms	68 ms
Prefilter thickness	6 mm	unknown
Measurement time	65 s	60 s

Table 3.2: Scan parameters of the head phantom measurement and the pelvis patient scan. The prefilter material for the head phantom scan was aluminum.

which the algorithm optimizes its scatter estimates. Photographs of both workpieces are shown in figure 3.3 and table 3.3 summarizes the scan parameters.

	Zinc die-cast plug housing	automotive controller
CBCT device	Werth TomoScope® L	Werth MultiSpek CT
R_{FD}	1095 mm	1828 mm
R_{F}	276 mm	920 mm
FOM	100 mm	200 mm
Number of detector pixels	1984^2	1984^2
Pixel size	0.2 mm	0.2 mm
Number of voxels	$1387 \times 1387 \times 1811$	$1873 \times 1873 \times 1842$
Voxel size	0.05 mm	0.1 mm
Steps (360°)	1200	3500
Tube voltage	300 kV	450 kV
Tube current	266 µA	1903 µA
Tube power	80 W	855 W
Integration time	500 ms	1000 ms
Prefilter thickness	1 mm	6 mm
Measurement time	600 s	3500 s

Table 3.3: Summary of the acquisition parameters of the CBCT measurements of the industrial workpieces. The prefilter material was tin in both cases.

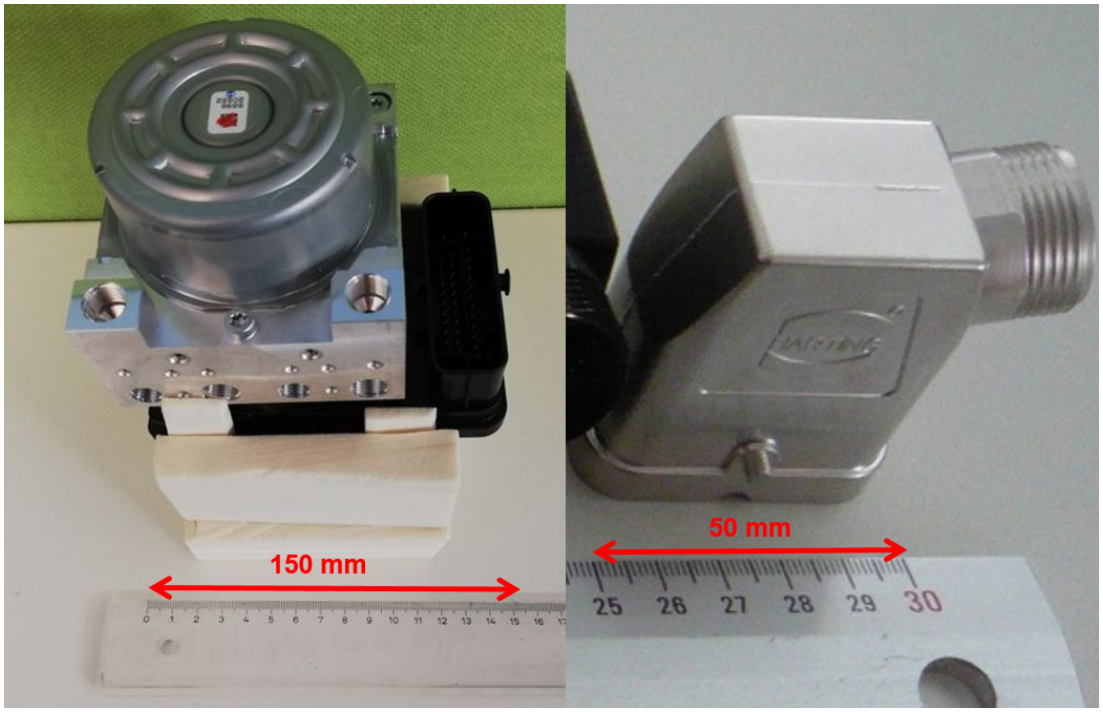

Figure 3.3: Photographs of the industrial workpieces whose tomographies were used to test ESC. Left: controller from the automotive sector. Right: zinc die-cast plug housing.

3.2 Results

3.2.1 Simulation Study

The simulation results in figures 3.4 to 3.7 generally show that ESC can effectively reduce scatter artifacts and improve the image quality for all CT simulations tested here.

For the simulated measurement of the head, the mean absolute error (MAE) to the scatter-free reconstruction can be reduced from 119 HU (uncorrected) to 15 HU in the CT image by applying ESC (cf. Fig. 3.4). This correction quality is close to the Monte Carlo simulation (13 HU) and exceeds the correction capability of both, a distorted (off-kV) Monte Carlo simulation (52 HU), which assumes a tube voltage of 100 kV instead of the actual 80 kV, and an image-based empirical scatter correction (31 HU) according to Meyer et al. [151]. Looking at the mean deviation in volume regions severely distorted by artifacts, this impression is confirmed: The uncorrected volume shows a deviation of more than 200 HU at this position, while ESC reduces this deviation to 12 HU. The correction using an exact Monte Carlo simulation is again closest to the scatter-free values at this location (9 HU), while ibESC has a deviation of 16 HU and the correction using a distorted off-kV Monte Carlo simulation has the largest deviation from the artifact-free volume with 98 HU. Figure 3.5 shows a line profile through the soft tissue region of each of the CT images shown in Fig. 3.4. Again, the observation is confirmed that an ESC correction, as well as a correction by a Monte Carlo simulation with perfect prior knowledge, comes closest to the artifact-free gray value distribution, and the ibESC, as well as the correction by an off-kV Monte Carlo simulation, give inferior results.

Corrections of the thorax and abdomen datasets using ESC and ibESC are shown in Figs. 3.6 and 3.7. Again, it can be seen that the quality of the volume is increased by using ESC and the diagnostic value of the data increases. Anatomical regions, which are not or only with difficulty recognizable without correction, become visible by applying ESC. Corrections using image-based ESC cannot increase the quality of the volume data to the same extent as those using rawdata-based ESC proposed here. Truncated data can also be effectively corrected using ESC. For these data, Monte Carlo simulations generally cannot provide a useful correction because of insufficient information about the total volume [52]. Since the data shown here are all simulated, which means that they can be easily extended over a virtually larger detector, no additional artifacts due to truncation are visible in the reconstructed volumes of the truncated projections.

Compared to the uncorrected data, the MAE with respect to the scatter-free reference CT images can be reduced by a factor of 3.7 to 6.2 by using ESC. At the same time, ibESC only achieves a reduction of the deviations by a factor of 1.3 to 5. Both qualitatively and quantitatively, the correction quality through ESC for the body datasets (abdomen and thorax) is below that for the head CT. This is due to the increased scatter-to-primary ratio in the different acquisitions. While this ratio averages to 0.6 for the head CT, it is much higher for the thorax (0.9 and 1.2, respectively) and abdomen CTs (1.6 and 2.1, respectively). This makes the correction difficult because small differences in the

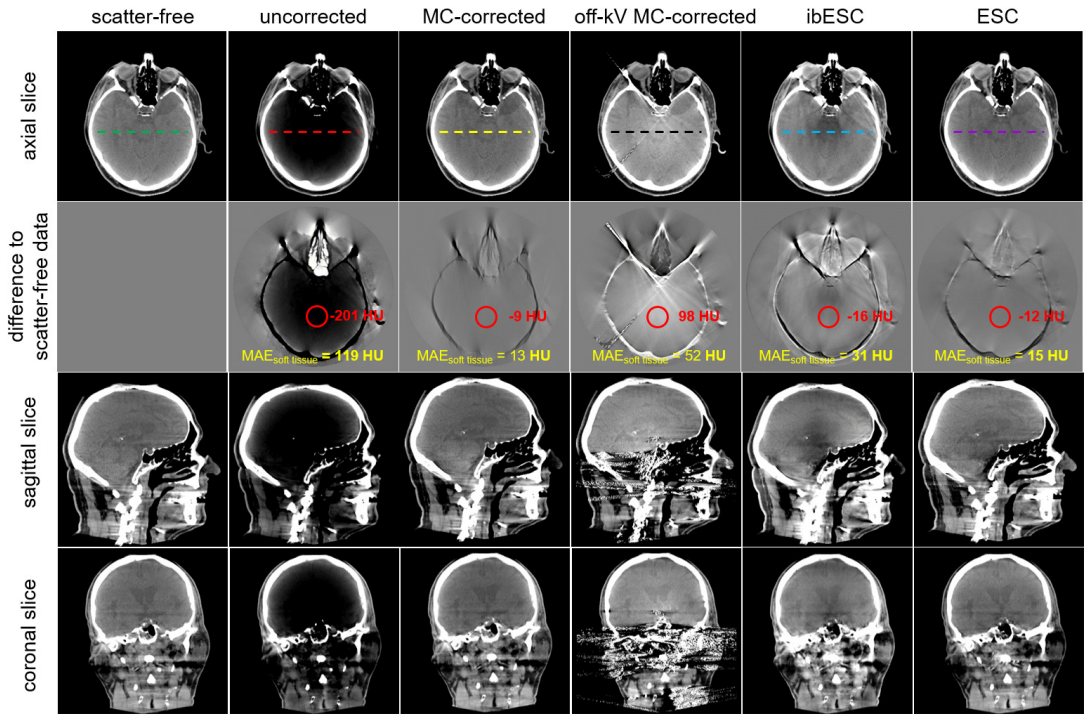

Figure 3.4: Resulting reconstructions for the simulated head CT ($C = 50\,\text{HU}$, $W = 400\,\text{HU}$). The left column shows data where no scatter artifacts are simulated and besides that the uncorrected data are given. The following columns correspond to different scatter corrections being applied: a correction using a Monte Carlo simulation with correct parameter settings, a correction using a distorted Monte Carlo simulation (off-kV), an ibESC, and the here proposed ESC. For each axial slice a dotted line is given, which corresponds to the the area from which the line profile shown in Fig. 3.5 is sampled. The second row shows difference images with respect to the scatter-free data ($C = 0\,\text{HU}$, $W = 400\,\text{HU}$). In these difference images the mean absolute error in soft-tissue regions is depicted in yellow, whilst the mean deviation in a region of interest (red circle) is given in red. Rows three and four show sagittal and coronal reformations of the volume ($C = 50\,\text{HU}$, $W = 400\,\text{HU}$).

scatter estimates to the actual scatter distribution tend to have a large impact on the correction result. In addition, this results in a poorer quality of the initial uncorrected volume and thus the initial segmentation of the soft tissue, in whose area the empirical scatter correction tries to optimize the CT values, becomes less accurate. Nevertheless, the correction results are satisfactory even in these cases.

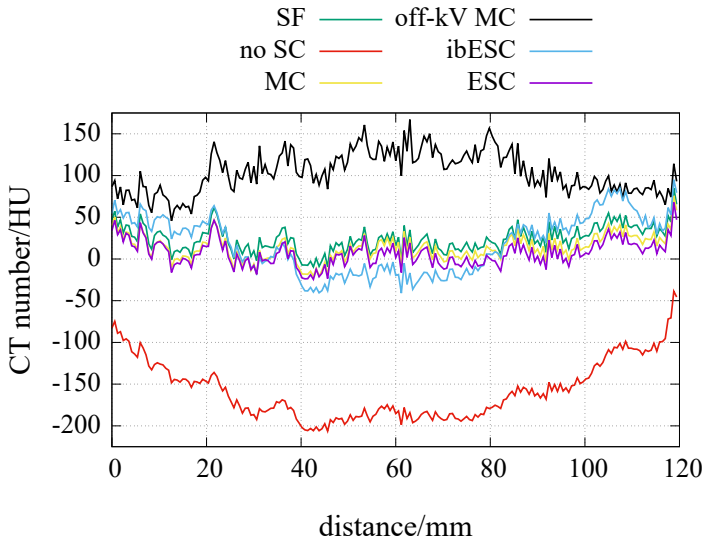

Figure 3.5: Line profiles of the different axial volume slices shown in Fig. 3.4. The abbreviation SF stands for scatter-free data and no SC means no scatter correction.

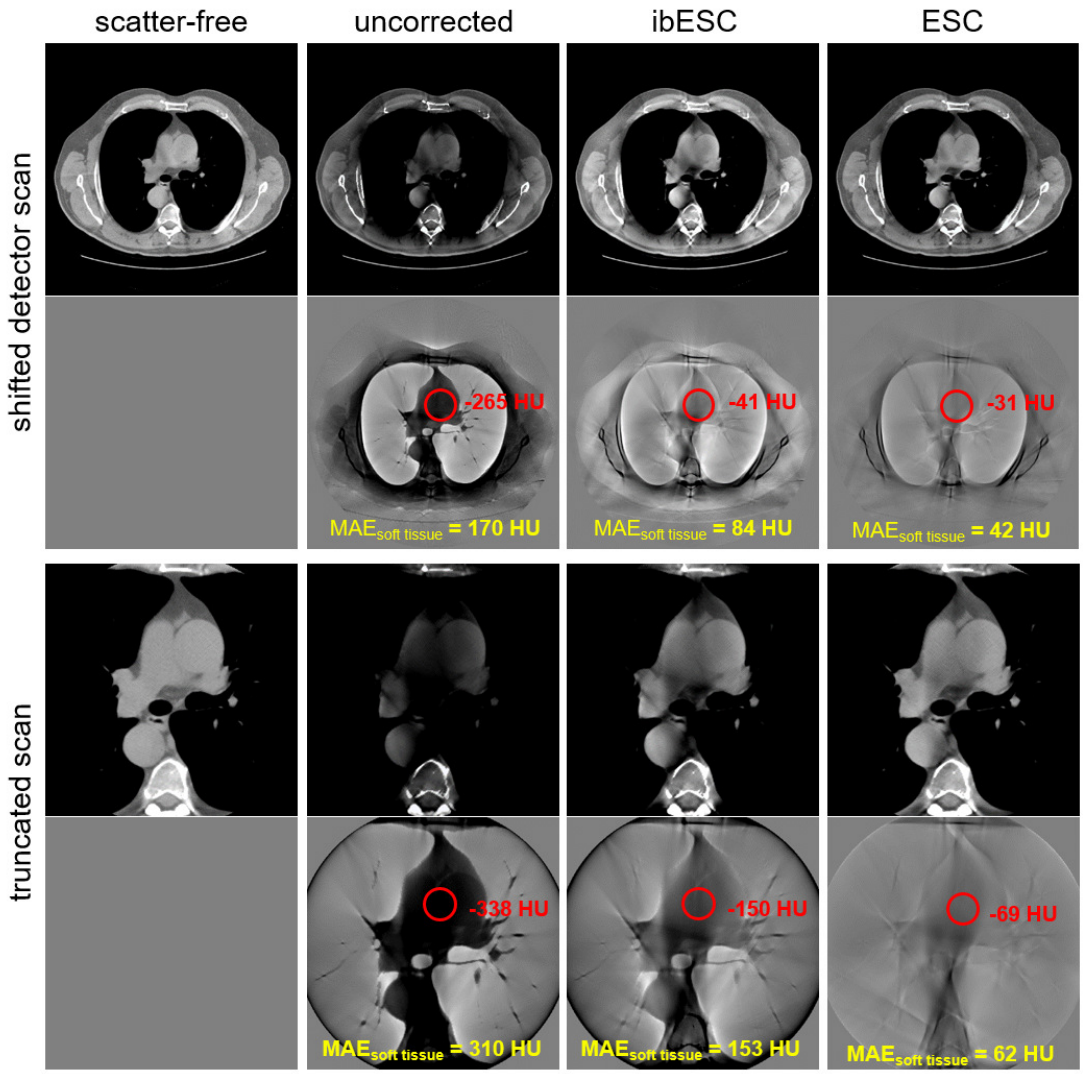

Figure 3.6: CT images (top, $C = 50\,\mathrm{HU}$, $W = 700\,\mathrm{HU}$) and difference images (bottom, $C = 0\,\mathrm{HU}$, $W = 700\,\mathrm{HU}$) for the thorax scans. The upper images show the datasets for the shifted detector scan and the lower images show those of the truncated scans. From left to right scatter-free, uncorrected, ibESC-corrected and ESC-corrected data are shown.

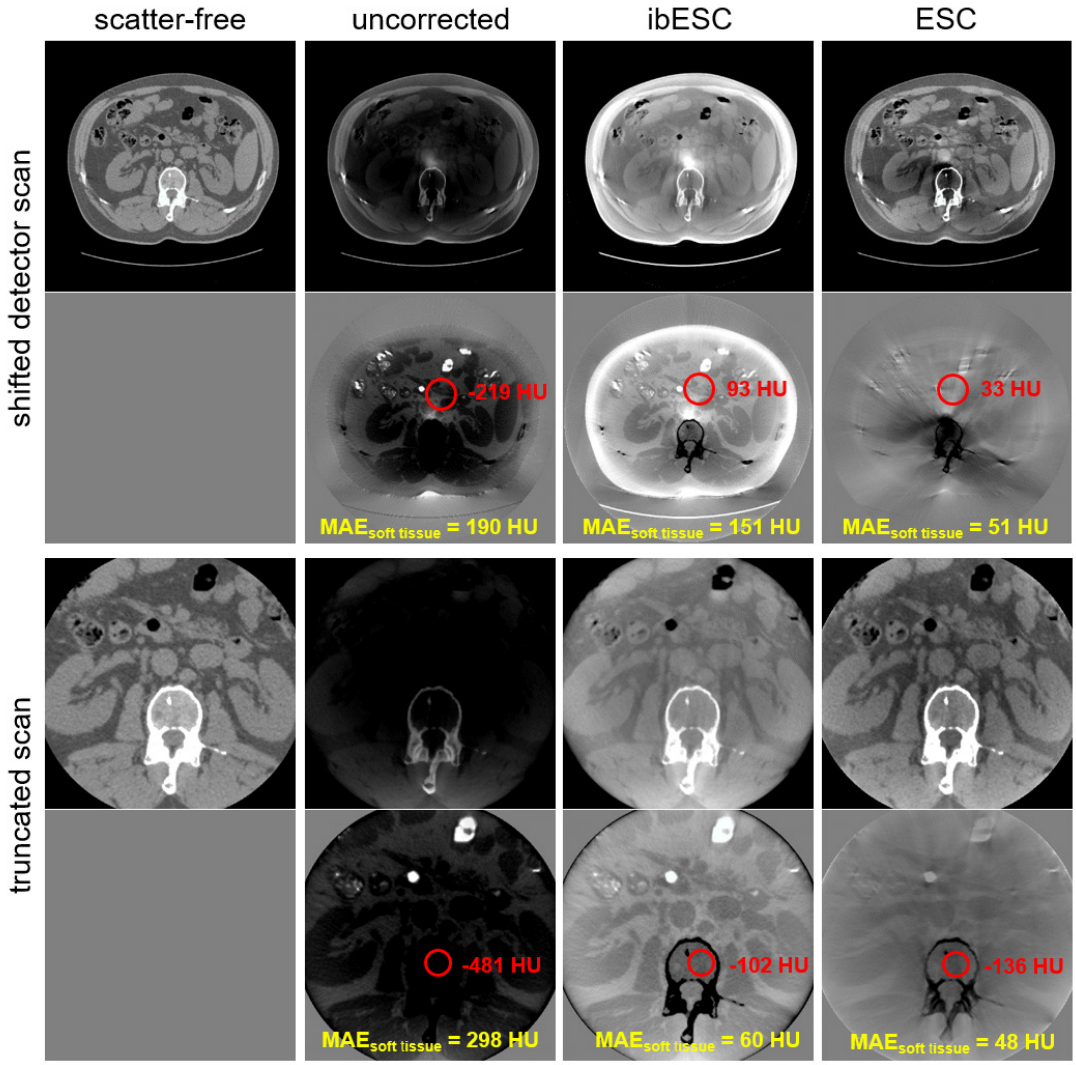

Figure 3.7: Results for the simulated abdomen CTs. For each CT image ($C = 50\,\mathrm{HU}$, $W = 700\,\mathrm{HU}$), a corresponding difference image ($C = 0\,\mathrm{HU}$, $W = 700\,\mathrm{HU}$) with respect to the scatter-free data is given below it. The upper images display the results of the shifted detector scan and the lower images those of the truncated scan. As in Fig. 3.6, scatter-free data, uncorrected data, ibESC, and ESC data are shown.

3.2.2 Measured Data

i.) Medical Cone-Beam Computed Tomography Data

The corrections of measured medical CBCT data using ESC are shown in Figs. 3.8 and 3.9 and as can be seen, ESC leads to a visible improvement in image quality for measurements, as well.

For the head phantom scan shown in Fig. 3.8, the mean absolute error to the slit scan in soft tissue areas can be reduced from 208 HU in the uncorrected case to 47 HU by ESC. A correction with ibESC reduces this deviation only to 55 HU. The evaluation of the MAE was performed here on a volume slightly smoothed with a Gaussian filter with standard deviation $\sigma = 1.2\,\mathrm{mm}$. This is to minimize the effect of image noise on this evaluation, which is very pronounced for the slit scan at more than 100 HU, and to make the effect of the scatter artifact correction more apparent. In highly distorted regions, the mean difference of CT values after using ESC is even only 35 HU with respect to the slit scan, instead of 289 HU in the uncorrected case. These deviations were evaluated within the circular ROI in the difference images from Fig. 3.8. Here, too, the advantage of the empirical scatter correction method presented here compared to the ibESC of Meyer et al. becomes clear, which shows a much higher deviation in this region (-70 HU). Nevertheless, both corrections, ESC and ibESC, increase the image quality considerably. This can be seen, for example, in the structures marked with yellow arrows in Fig. 3.8, which are barely visible in the uncorrected volume and become clearly visible by the corrections. Qualitatively, the corrected volumes agree well with the reference volume of the phantom measured on the clinical MSCT scanner, which has nearly no scatter artifacts as well as a high signal-to-noise ratio due to the use of a high-power x-ray tube and a curved detector with large anti-scatter grids. Because of larger detector pixels of $600\,\mu\mathrm{m} \times 600\,\mu\mathrm{m}$ in this scanner, the spatial resolution of the MSCT volume is lower than that of the CBCT measurements, however.

At this point, it should be noted that there is a steel rod in the head phantom, which is clearly visible in the sagittal volume slice in Fig. 3.8. This experiment thus shows that ESC can also be used in the presence of highly absorbing materials such as metals and associated local low intensity values and high scatter-to-primary ratios, as will be shown again in the following for the industrial CBCT data and is of particular importance in this context.

The results for a scatter correction of measured patient data are shown in Fig. 3.9. Both ESC and ibESC can achieve a good correction result and improve the image quality compared to the uncorrected data. However, also on the patient data ESC provides better correction results than ibESC, which is especially noticeable by more homogeneous gray values in the same tissue structures. Regions both in the center of the patient and in the outer areas are strongly affected by scatter artifacts, which is noticeable by strong cupping in the uncorrected volume. These artifacts can be corrected, particularly by ESC and the reference correction method of Star-Lack et al. [148] to a large extent. The reference correction method [148] optimized for this CT device provides the most homogeneous gray value distribution here and thus the best

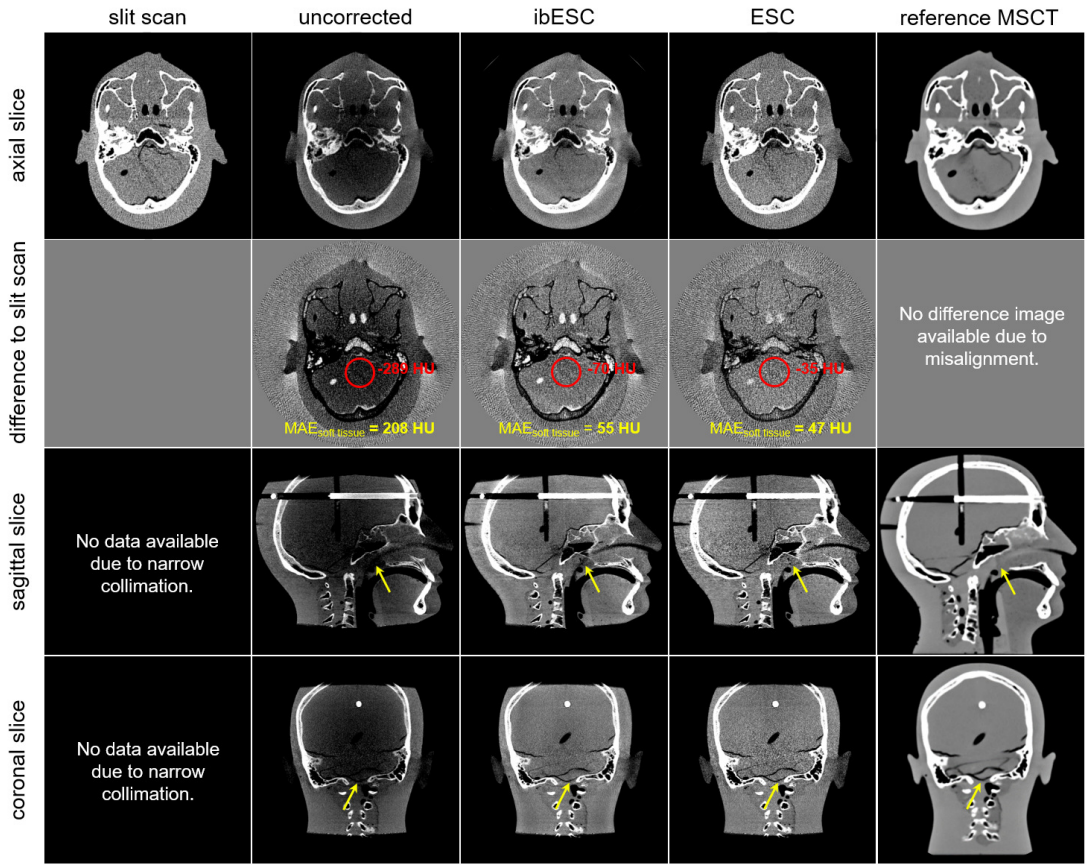

Figure 3.8: Here, CT images of the head phantom are given for a slit scan on a table-top CBCT, an uncorrected CBCT scan, the CBCT scan corrected with ibESC and ESC, and a MSCT scan of this phantom. The top row shows an axial slice of the volume and the second row a difference image for this slice with respect to the almost scatter-free slit scan. In the difference images information regarding the MAE and mean deviations in the ROI depicted by the red circle are given. Rows three and four show sagittal and coronal slices of the volume with yellow arrows highlighting some structures that are only visible by applying a scatter correction on the CBCT data. $C = 0\,\mathrm{HU}$, $W = 700\,\mathrm{HU}$.

results. In the coronal and sagittal volume slices, it can be seen that tumor markers are embedded in the area of the seminal vesicles. While in the uncorrected CT image the anatomical structures near the tumor markers are barely visible in a typical soft tissue window setting, the corrections can guarantee the visibility of these areas and thus simplify or enable diagnosis. The dashed lines in Fig. 3.9 run along the prostate in the axial and along the bladder and seminal vesicle in the sagittal volume slice. Line profiles for these areas are shown in Fig. 3.10. It can be seen that the CT values by

a correction using ESC are close to the optimized solution used by the manufacturer according to reference [148].

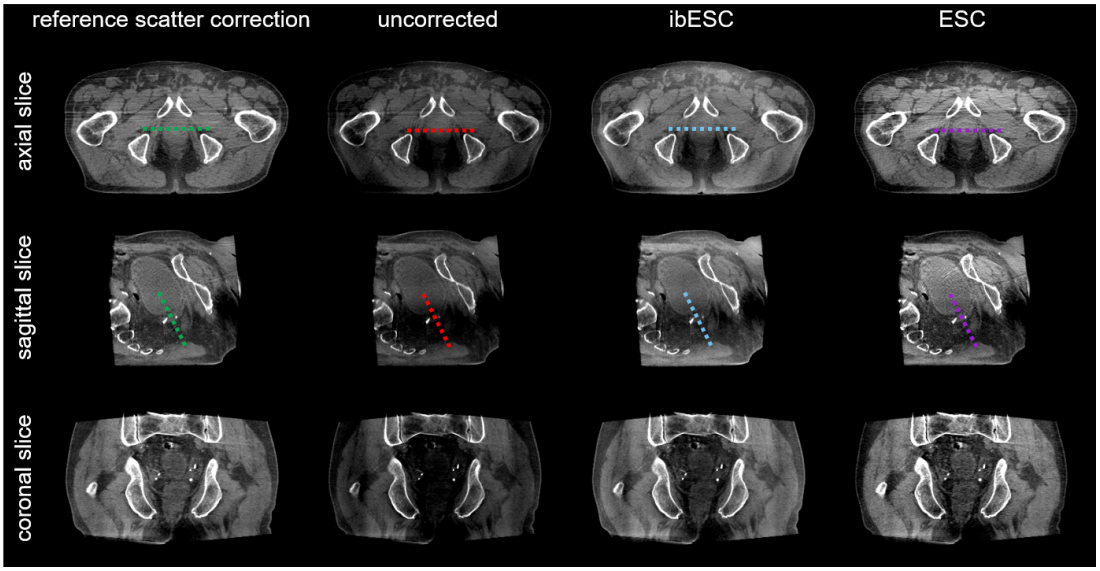

Figure 3.9: This figure shows CT images of the pelvis patient data. From left to right different scatter corrections were applied: a reference scatter correction according to reference [148], no scatter correction, ibESC, and ESC. The top row displays an axial slice, the middle row a sagittal slice, and the bottom row a coronal slice of the respective CT volume. The dashed lines in the axial and sagittal slices correspond to regions along which the line profiles shown in Fig. 3.10 are evaluated. $C = 50\,\mathrm{HU}$, $W = 500\,\mathrm{HU}$.

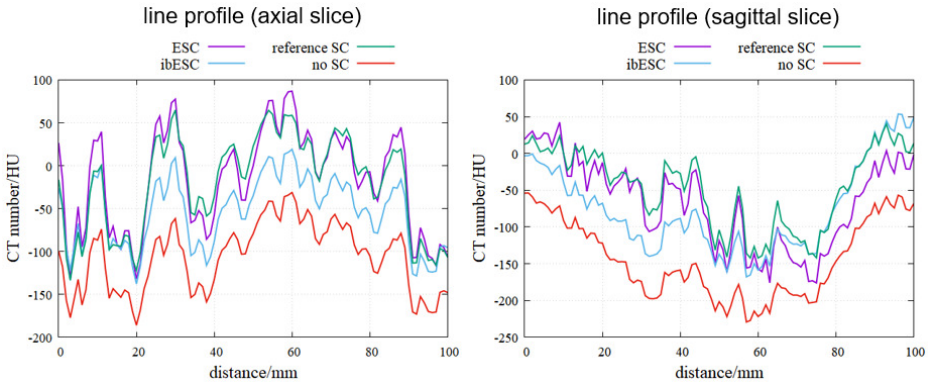

Figure 3.10: Line profiles of the axial and sagittal volume slices shown in Fig. 3.9. The colors of the line profiles match those of the dashed lines in Fig. 3.9 for the respective dataset.

ii.) Industrial Cone-Beam Computed Tomography Data

Also for industrial CBCT datasets, ESC provides improved image quality for the same scatter model as it was used for the medical datasets before. Figure 3.11 shows the correction results for the automotive controller using an example axial volume slice at $z = 71\,\text{mm}$. It can be seen that the gray value distribution within the drilled aluminum block in the center of the object becomes more homogeneous by using ESC. Remaining artifacts, which are visible as dark streaks near strongly absorbing metals, can be caused by beam hardening, for example, and do not necessarily indicate an insufficient ESC correction. Due to the scatter correction, the homogeneity of the gray values increases not only in the aluminum areas but also in areas of other materials. This is particularly evident in the two regions of interest shown by yellow boxes. Transitions between plastic and air can hardly be detected in the uncorrected image due to strong artifacts (cf. red arrows in the figure). With ESC, these transitions are clearly defined and can be evaluated. The volume processed by ESC exhibits an increased noise level, which is also evident in the ROIs. Since in CT mainly the CNR is important, which is increased by ESC in relevant regions of the volume, this increase in noise is acceptable, though.

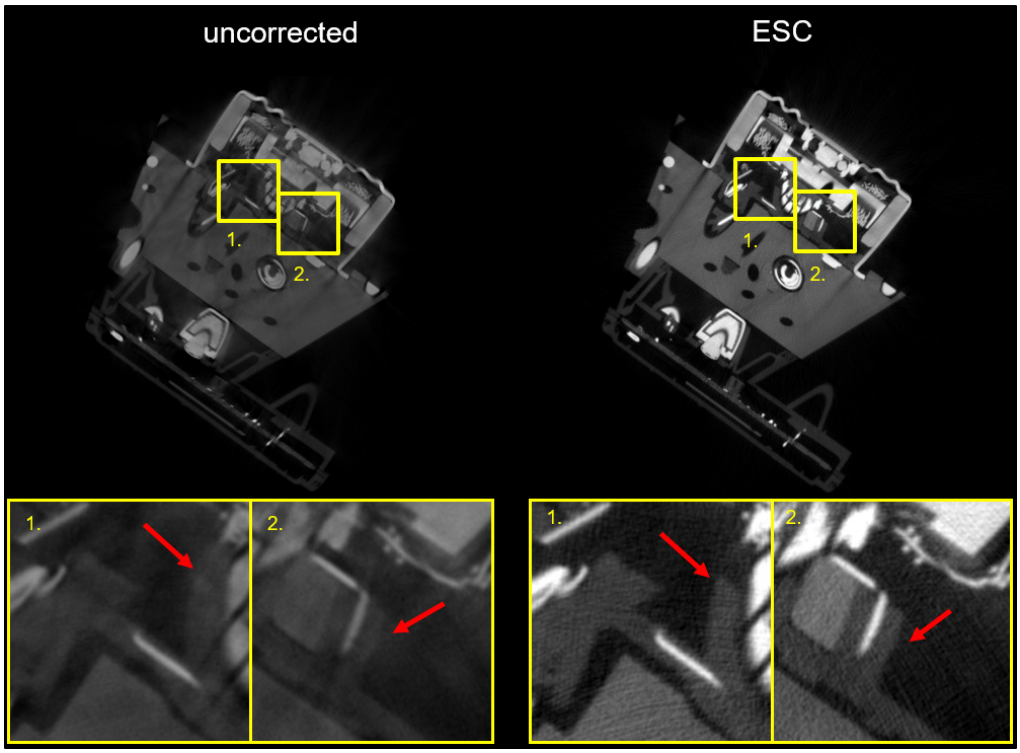

Figure 3.11: CT images ($C = 0.05/\text{mm}$, $W = 0.1/\text{mm}$) of the automotive controller showing the uncorrected volume (left) and a volume corrected with ESC (right). The yellow boxes on the bottom of the figure show ROIs of the respective CT image. Red arrows mark problematic regions of the uncorrected data.

The correction of the zinc die-cast plug housing is shown in Fig. 3.12. In addition to an axial volume slice at $z = 41.5\,\text{mm}$ for the uncorrected volume and the ESC-corrected volume, a surface model of the workpiece calculated from each volume is also shown in this figure. The calculation of the surface models in stereolithography (STL) format from the volume data was done using the marching cubes algorithm [120]. In addition to an increase in image quality in the volume achieved by ESC, which is visible, for instance, in reduced cupping artifacts, various improvements to the surface model become apparent, which are marked in Fig. 3.12 by red arrows with numbering. The reduction of artifacts results in a better segmentability of the volume and thus a more precise localization of the workpiece surface, which in some cases makes structures more clearly visible (1). In addition, faulty segmentations that lead to bulges (2) or even holes (3) in the surface model and thus severely corrupt the surface information, are corrected by ESC.

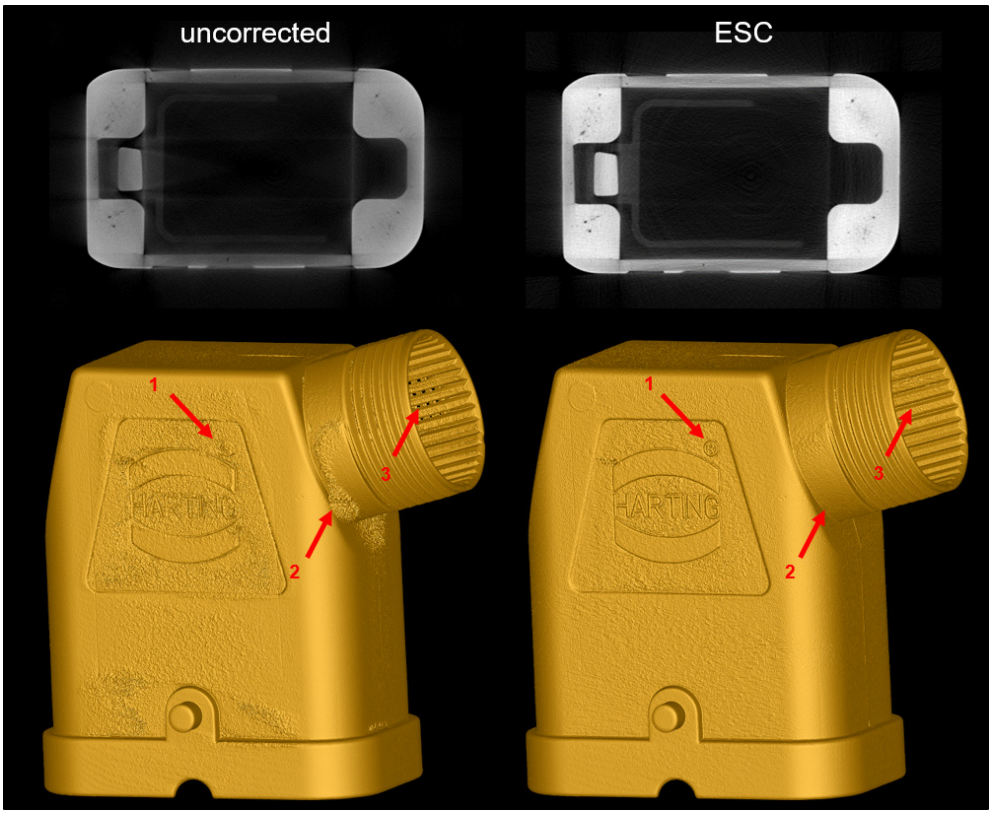

Figure 3.12: This figure shows volume slices (top, $C = 0.09/\text{mm}$, $W = 0.18/\text{mm}$) of the uncorrected zinc die-cast plug measurement (left) and the measurement corrected with the empirical scatter correction (right). Furthermore, surface models of these datasets are given (bottom). Regions where ESC leads to a significant improvement of the surface are marked with numbered red arrows.

3.3 Discussion

The empirical scatter correction represents an useful algorithm for the reduction of systematic measurement deviations due to scattered radiation without the use of prior knowledge. For corrections using ESC, only rawdata and the ability to reconstruct these rawdata are required. The rawdata itself may also be obtained by forward projection of the measured volume, of course. Such a method, which can reduce scatter artifacts without prior knowledge, is particularly advantageous when data from an unknown measurement system or with unknown acquisition parameters must be corrected, the measured object contains unknown materials, or the acquisition geometry provides only reduced information about the measured object, as is the case with truncated measurements (cf. Figs. 3.6 and 3.7). In such cases, analytical methods for scatter corrections, such as Monte Carlo simulations, reach their limits [52].

As the results show, ESC generally increases the image quality for CBCT measurements. This in turn increases the diagnostic value of the volume data in medical applications and can improve the nondestructive testing abilities and metrological evaluability of workpiece analyses using CT. In addition, the accuracy of CT numbers is increased by ESC. However, as the deviation of CT numbers is still comparatively high, ESC cannot be used in clinical routine for dose calculations for radiotherapy. Nevertheless, the improvement of image quality due to ESC can be used for interventional CT and to improve the segmentability of volumes, which is relevant for both, clinical and industrial CT applications. The accuracy of measuring points on the workpiece surface, which is particularly relevant for industrial metrology, can also be increased by ESC (cf. Fig. 3.12). Such an increase in the accuracy of measuring points will most likely also gain importance for the medical application of computed tomography in the future, since accurate surface determinations by means of CT in combination with precise additive manufacturing processes enables the generation of individual prostheses [152].

A comparison of the empirical scatter correction proposed here with the method of Meyer et al. [151] shows that ESC provides better correction results. This indicates that it makes sense to reduce scatter artifacts already in the measured intensities, i.e. the place where they have their physical origin.

Scatter correction algorithms that are optimized for the sample, measurement system, and acquisition parameters still provide the best correction results (cf. Fig. 3.9), so the use of ESC should not be advised if such a solution and adequate prior knowledge is available. However, the ESC algorithm has distinct advantages in the absence of prior knowledge, as is evident from the experiment with the intentionally incorrectly assumed tube voltage for a correction using a Monte Carlo simulation in Fig. 3.4, which leads to inferior correction results.

As ESC aims to optimize the reconstructed volume by subtracting low-frequency basis images from the measured intensities, it is in principle capable of correcting not only scattered radiation caused by the scanned object but also other artifacts that correspond to low-frequency disturbances on the intensities, such as backscatter from the detector or its housing or scatter signals caused by the collimator [131] or prefilter

[132]. For this purpose, the basis images should be able to model these scatter signals accordingly. The scatter model chosen for the ESC basis functions here works well for all considered datasets but may not yet be the optimum. The use of adaptive filters [153] may be an option to further improve the scatter model and hence the correction efficiency of ESC in the future.

A drawback of ESC is that even though the optimization process is performed on a reduced voxel grid with a reduced number of subsampled projections, the runtime is in the order of few minutes and therefore relatively long compared to state of the art learning-based approaches [27], [41] that require a trained model to be available. Furthermore, noise, which is induced by scattered radiation cannot be corrected by ESC, as it is the case for any post-correction approach. This may result in an increase of image noise in the corrected data (cf. Fig. 3.11). In section 6, a method is proposed to counteract such increased noise levels. Another limitation of the empirical scatter correction is that the uncorrected volume needs to be segmentable in order to have a well-defined optimization criterion for the algorithm. If artifacts are very severe, this may not always be the case. However, the segmentation does not need to be very precise from the start. ESC may be used iteratively to improve the segmentation and scatter basis images and therefore the correction efficiency. Even though the artifacts are quite severe in the cases considered in section 3.2, the results shown here are all obtained by a single iteration of ESC and the algorithm is still able to remove most of the scatter artifacts.

Future opportunities for an empirical reduction of systematic measurement deviations in CT and CBCT measurements without specific prior knowledge may be provided by a combination of the ESC algorithm and algorithms for empirical beam hardening corrections [154], [155].

4 Novel Method for the Reduction of Systematic Measurement Deviations and Optimization of the Spatial Resolution by Fusing Measurements Acquired with Two X-Ray Tubes

Having presented a method for reducing systematic measurement deviations due to scattered radiation in the previous chapter, this chapter will focus on the combination of datasets from measurements with different x-ray tube types at different x-ray spectra to an artifact-reduced and spatial resolution-optimized dataset, combining or even improving the advantages of the individual datasets. The method presented in the following will be denoted the frequency split dual energy CT (FSDECT) combination. It resembles established dual energy CT (DECT) data combinations for artifact reduction (see Sec. 2.4.1) and may be considered as an extension to CT systems that employ two x-ray tubes with strongly varying focal spot sizes. In addition to a DECT artifact reduction, the FSDECT method extends this existing approach by a spatial resolution optimization step, where the spatial frequencies of the underlying datasets are changed at different stages of the algorithm, which serves as the motivation for the designation frequency split.

4.1 Material and Methods

4.1.1 MultiSpek: Industrial Cone-Beam Computed Tomography System with Two X-Ray Tubes

Figure 2.1 in chapter 2 shows an exemplary setup for an industrial CBCT system. The MultiSpek CBCT system discussed in this chapter differs from this setup in the following way: instead of a single x-ray source, two x-ray sources, which are mounted horizontally on top of each other, are installed in this CT system (see Fig. 4.1). One of these sources is a 300 kV microfocus x-ray tube with a transmission target whereas the other x-ray source corresponds to a 450 kV macrofocus x-ray tube with a reflection target. As described in section 2.1.1, these tube types significantly differ in their construction type, leading to different maximum tube voltages, maximum tube powers and, related to these traits, different focal spot sizes. Whilst measurements with the macrofocus tube, which allows for high tube powers, tube voltages and strong prefiltration, can be used to obtain CT volumes with a low amount of statistical and systematic measurement deviations, measurements with the microfocus tube have a higher structural resolution and allow for inspections and measurements of smaller structures.

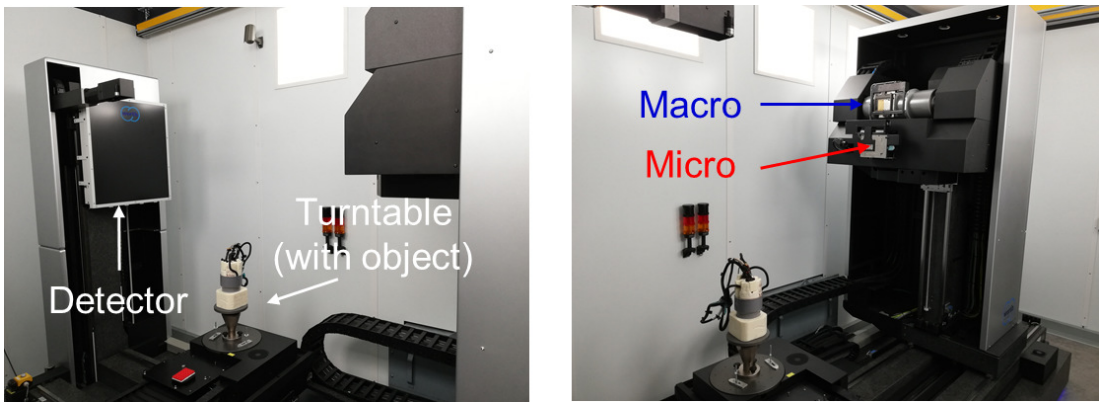

Figure 4.1: Photography of the MultiSpek CBCT system. Left: view of the detector and turntable. Right: view of both x-ray tubes: macrofocus tube (top) and microfocus tube (bottom).

In order to use spectral information for artifact reduction as it was described in section 2.4, the MultiSpek CBCT system offers the opportunity to scan workpieces with different spectra using two different tube designs, which in principle enables high spectral separations even at high photon energies of up to 450 keV. Different spectral datasets using both x-ray tubes are acquired sequentially at the MultiSpek CBCT system, as depicted in Fig. 4.2. The tubes are moved between both measurements such that the focal spot position is at approximately the same position with a sensor offset of only $\mathcal{O}(1\,\mu m)$. It can therefore be assumed that the beam path and scan geometry are approximately the same for each data acquisition. After the sequential measurement with both tubes at different voltages, both rawdatasets are either first corrected for

scatter artifacts with the empirical scatter correction and then reconstructed on the same voxel grid or directly reconstructed on the same voxel grid resulting in the aligned voxel volumes $f_{\text{Micro}}(x, y, z)$ and $f_{\text{Macro}}(x, y, z)$ for the measurements with micro- and macrofocus tube, respectively. Measurements with the micro- or macrofocus tube will from now on be denoted Micro or Macro measurements and the term Micro or Macro volume is used for the resulting volume data $f_{\text{Micro/Macro}}(x, y, z)$.

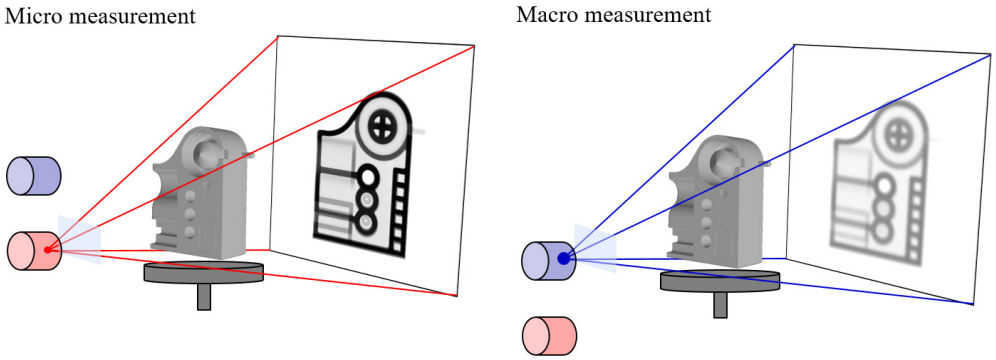

Figure 4.2: Scheme of a sequential measurement at the MultiSpek CBCT system. Left: measurement with the microfocus tube. Right: measurement with the macrofocus tube.

	Macro	Micro
R_{FD}	1828 mm	1828 mm
R_{F}	920 mm	920 mm
FOM	200 mm	200 mm
Number of detector pixels	1984^2	1984^2
Pixel size	0.2 mm	0.2 mm
Number of voxels	$1933 \times 1933 \times 1926$	$1933 \times 1933 \times 1926$
Voxel size	0.1 mm	0.1 mm
Steps (360°)	3500	3500
Tube voltage	450 kV	300 kV
Tube current	1622 µA	266 µA
Tube power	730 W	80 W
Integration time	1000 ms	1000 ms
Prefilter thickness	6 mm	1 mm
Measurement time	3500 s	3500 s

Table 4.1: Scan parameters for the Micro and Macro measurements of the automotive controller shown in section 4.2. The prefilter material was tin in both cases.

The FSDECT algorithm, which is explained in the following section, was tested using measurements of the automotive controller workpiece, which was already introduced in

the previous chapter (see Fig. 3.3). The scan parameters for the measurements of the automotive controller are given in table 4.1 for the Micro and Macro measurements. It can be seen that the Macro measurement employs a very high energetic, hardened spectrum with a tube voltage of 450 kV and a prefiltration of 6 mm of tin. Compared to the Micro measurement, which only has a tube voltage of 300 kV with a prefiltration of 1 mm of tin, the artifacts are expected to be much less pronounced in the Macro volume and the spectra are well separated between both scans.

4.1.2 Data Combination Process

The workflow of the FSDECT data fusion algorithm is depicted in Fig. 4.3. As a first step of the data fusion, the spatial resolution of both volume datasets must be aligned. This step is necessary to avoid a superposition of different frequencies at edges, which would inevitably lead to double edge structures in the merged volume. Once both volumes have the same spatial resolution, they are linearly combined to obtain a artifact-reduced DECT volume using pseudo-monochromatic imaging (cf. Sec. 2.4.1). In the final step, spatial resolution enhancement of the artifact-reduced DECT volume is performed. This is done by selectively transferring high-pass information from the Micro volume to the DECT volume. The frequency split dual energy CT (FSDECT) volume, which is finally obtained by the method presented here, has an increased image quality in terms of artifact content and spatial resolution. Each single step of this data combination process is explained in more detail in the following subsections.

i.) Adjustment of the Spatial Resolution of the Initial Volume Data

Since the MTF of image data is a quantitative measure of the spatial resolution of the data (see Sec. 2.2.1), the spatial resolution of the two volumes obtained by the two measurements using different x-ray tubes is adjusted by matching the MTFs of both volumes.

For this purpose, the MTFs of both volumes are first determined along an edge within an axial volume slice using Eq. (2.41). For the correction of the automotive controller measurements, a straight edge at the outside of the aluminum block component was used for the position to calculate the MTF (cf. Fig. 4.4). Perpendicular line profiles are drawn and averaged along this edge transition. This leads to a low noise ESF. By differentiation and Fourier transformation, the MTF of the volume is obtained for the area under investigation, which serves as a benchmark for the spatial resolution of the entire volume data of the respective measurement.

To equalize the MTF, the spatial frequency of the Micro measurement is reduced in order to match the MTF of the Macro volume. The reduction of the spatial frequencies of the Micro measurement is done by a three-dimensional isotropic Gaussian low-pass filter. The optimal strength of the Gaussian filter (i.e. its standard deviation) is determined using a Nelder-Mead algorithm. In each iteration step of this parameter optimization process, the Micro volume is smoothed in a sufficiently large area around the object edge under investigation and the MTF of the smoothed volume is evaluated. The cost

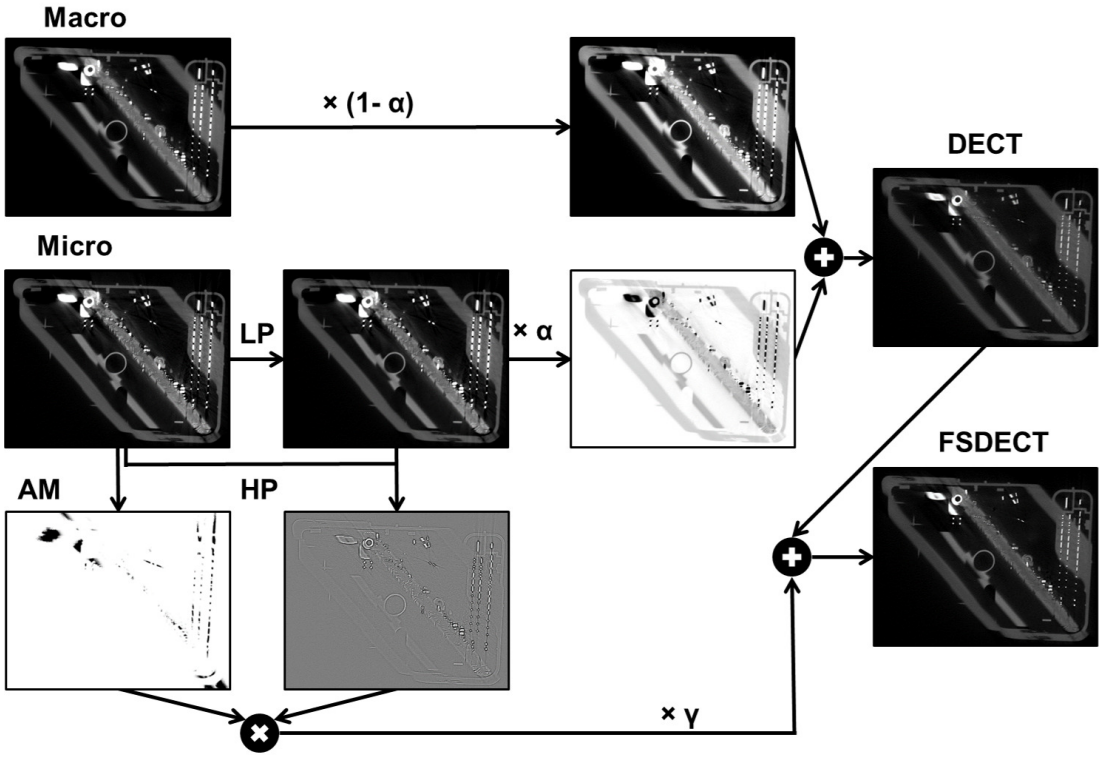

Figure 4.3: Workflow of the FSDECT data fusion process. The abbreviations LP and HP correspond to low- and high-pass filter operations, AM denotes the artifact mask (see Alg. 2) and α is the linear blending variable for the generation of the pseudo-monochromatic DECT volume (cf. Eq. (2.56)).

function corresponds to the absolute deviation of the MTF of the Macro volume to the MTF of the smoothed Micro volume. The optimization problem for determining the standard deviation of the Gaussian low-pass filter σ is hence of the form:

$$\sigma = \underset{\sigma'}{\operatorname{argmin}}\left(\sum_{k} \left|\mathrm{MTF(k)}_{\mathcal{N}(0,\sigma'^2)*f_{\mathrm{Micro}}(x,y,z)} - \mathrm{MTF(k)}_{f_{\mathrm{Macro}}(x,y,z)}\right|\right) \tag{4.1}$$

Fig. 4.4 shows the MTF of the Macro, Micro and smoothed Micro volumes. It can be seen that the MTF adjustment works well with the here proposed method. In principle, dividing the MTF of the Micro volume by that of the Macro volume would yield the desired convolution kernel in frequency space. However, care must be taken with this method, since the MTF of both datasets may have zeros in the high frequency range or may differ only slightly from zero, which leads to an undefined behavior for the thus determined convolution kernel in this frequency band. In such an approach, therefore, another parameter must be inserted to define a cut-off frequency for the division.

Since the same detector and the same generic image processing filters and filtered backprojection algorithms were used on the Micro and Macro datasets, the difference in

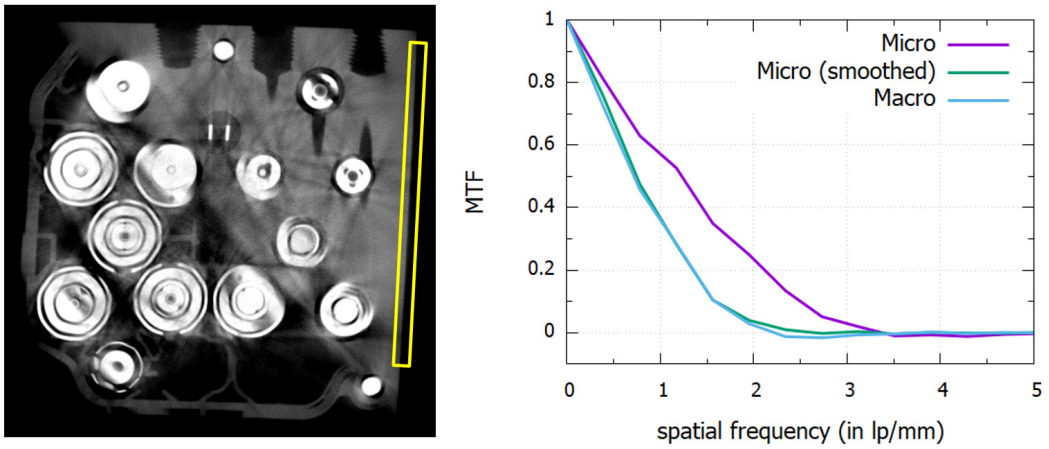

Figure 4.4: Left: Macro volume slice ($C = 0.03/\text{mm}, W = 0.07/\text{mm}$). The yellow box depicts the edge position at which the MTFs are determined. Right: MTF curves of the Macro, Micro and smoothed Micro volumes.

the MTF of the two volume datasets that needs to be adjusted is mainly due to the different size and, potentially, intensity profiles of the focal spots. A different size and intensity profile of the focal spot generally leads to a different blurring of the measured x-ray intensities. Even though this modulation of the x-ray intensities may be modeled quite accurately by a Gaussian [127], it is known that focal spot shapes may differ from a Gaussian [156]–[158] which may lead to anisotropic behaviours in reconstructed volumes [159]. Also the size of the focal spot and the wear on the target can change the size and shape of the focal spot. Thus, a physically correct modeling of the resolution adjustment of both datasets would use a convolution of the x-ray intensities of the Micro dataset with a non-predefined convolution kernel to address possible differences in focal spot size and shape. The here proposed use of an isotropic 3D Gaussian low-pass filter on the reconstructed volume, therefore, corresponds to an approximation for the resolution adjustment. Nevertheless, the volumes processed with the here proposed method do not exhibit any noticeable problems such as double edges, and the MTF of the Macro and processed Micro volumes strongly resemble each other. Therefore, and due to the possibility of a performant implementation of the separable isotropic Gaussian filter and the associated simplified optimization criterion (see Eq. (4.1)), this approximation method is used here.

ii.) Dual Energy Computed Tomography Combination

If two spectral volume datasets are available at the same spatial resolution on the same voxel grid, pseudo-monochromatic images (cf. Sec. 2.4.1) with a reduced amount of systematic measurement deviations can be calculated. Given the processed Micro volume, the DECT data combination here is obtained by a modification of equation (2.56):

$$f_{\mathrm{DECT}}(x,y,z) = \alpha\,(\mathcal{N}(0,\,\sigma'^2) * f_{\mathrm{Micro}}(x,y,z)) + (1-\alpha)\,f_{\mathrm{Macro}}(x,y,z) \tag{4.2}$$

In order to receive a fusion volume $f_{\mathrm{DECT}}(x,y,z)$ with the lowest possible artifact content, the blending factor α must be chosen accordingly. One possibility to quantify the artifact content is to calculate the mean squared deviation of the voxels of a specific material from a reference gray value, similarly to what is done for the parameter optimization in ESC. A high deviation of the gray values with respect to that reference value indicates a high amount of artifacts. The reference gray value corresponds to the mean gray value of the material of interest or the main material in the workpiece. This gray value is here obtained by segmenting the volume using Otsu's method (cf. Sec. 2.1.6) and evaluating the mean gray value of the segmented voxels. To keep this reference gray value in the fusion volume independent of the blending factor and to simplify following processing steps, a conversion of the attenuation values from the Micro and Macro volume to generalized Hounsfield units is performed. As described in section 2.1.5, the Hounsfield unit is the predominant unit of CT attenuation coefficients in clinical applications and usually describes a rescaling of the attenuation coefficients such that water is at a value of 0 HU and air is at a value of -1000 HU. Since aluminum corresponds to the main material in the example workpiece under consideration, the automotive controller, the gray values are here rescaled on the basis of the aluminum gray values. For other workpieces, the gray values can of course be rescaled with respect to other materials. According to Eq. (2.30), the rescaling of f_{Micro} and f_{Macro} is thus done in such a way that both volumes contain 0 HU for the average gray value of the reference material μ_{Ref} and -1000 HU for the gray value of air.

It is now easy to see that Eq. (4.2) for the fusion volume also produces an average gray value of 0 HU in the reference material and -1000 HU in air, independent of the choice of α. The parameter optimization for α then reads

$$\alpha = \underset{\alpha}{\mathrm{argmin}}\Big(\sum_{x,y,z} M(x,y,z)\,(\alpha\,\mathrm{CT}_{\mathrm{Micro}}(x,y,z)+(1-\alpha)\,\mathrm{CT}_{\mathrm{Macro}}(x,y,z)-\mathrm{CT}_{\mathrm{Ref}}(x,y,z))^2\Big)\,, \tag{4.3}$$

where $M(x,y,z)$ corresponds to a binary mask obtained by the previous segmentation of the main material, which equals one for voxels within the thresholds determined by this segmentation and zero elsewhere, and $\mathrm{CT}_{\mathrm{Ref}}(x,y,z) = 0\,\mathrm{HU}$. This equation can then easily and precisely be solved for α. Descriptively explained, the volume combination is thus performed in such a way that the CT values of the DECT volume within the reference material segmentation are as close as possible around the target value 0 HU because this then corresponds to a volume where artifact-related CT value deviations within the same material are reduced.

It should be noted here that for the algorithm to be applied automatically, the automatic segmentation of the reference material must work sufficiently well. This may be difficult, for example, if strong artifacts are present in the data. For this reason, the segmentation is performed on the Macro volume, which already has a lower artifact

content than the Micro volume and superior spatial resolution is not needed at this point. Furthermore, the algorithm can in principle be used iteratively to recalculate the segmentation after each iteration on the fusion volume and thus improve it. Another possibility is to adjust the blending factor by visual inspection. Since it is only one optimization parameter, the optimal choice of α can easily be chosen on a reference CT image of the fusion volume. For the results shown in section 4.2, visual inspection was used to optimize the automatically determined parameters.

iii.) Optimization of the Spatial Resolution of the Fusion Volume

As a final step of the FSDECT data combination, the spatial resolution of the DECT volume is optimized (cf. Fig. 4.3). This is done by a partial transfer of high frequencies from the high-resolution Micro volume to the fusion volume. Such and similar procedures in CT, in which frequency information of different images is selectively transferred to another image, are often referred to as a frequency split techniques. The high frequencies from the Micro volume are obtained by a high-pass filtering operation $\mathrm{HP}_{\mathrm{Micro}}$, which here corresponds to the residual of the previously performed low-pass operation $\mathrm{LP}_{\mathrm{Micro}}$:

$$\begin{aligned} \mathrm{HP}_{\mathrm{Micro}} &= 1 - \mathrm{LP}_{\mathrm{Micro}} \\ f_{\mathrm{Micro,\ HP}}(x,y,z) &= f_{\mathrm{Micro}}(x,y,z) - \mathcal{N}(0,\,\sigma'^2) * f_{\mathrm{Micro}}(x,y,z) \end{aligned} \tag{4.4}$$

The high-pass filtered Micro volume $f_{\mathrm{Micro,\ HP}}(x,y,z)$ contains information about its edge sharpness and structural details, which are intended to be preserved in the FSDECT volume. However, in addition to this useful image information, which improves the structural resolution, both the noise of the Micro volume, as well as high-frequency artifacts of the Micro volume, are located in these high spatial frequencies. This on the one hand leads to a noise increase in the combination volume, and on the other hand allows a carryover of artifacts already removed in the DECT volume.

At this point, nothing can be done about the increased noise without losing structural resolution at the same time and, similar to the noise increase due to the DECT combination (cf. Eq. (2.57)), it must be accepted for the time being as a negative side effect of the fusion. However, the transfer of high-frequency artifacts can be at least partially prevented: It is possible to determine a portion of these artifacts and suppress it in the high-passed volume $f_{\mathrm{Micro,\ HP}}(x,y,z)$ before its transfer to the fusion volume.

For this purpose, an artifact mask (AM) is calculated from the unfiltered Micro volume, which has values close to or equal to zero at positions with high-frequency artifacts and values close to or equal to one otherwise. Determining an artifact mask is generally not a trivial operation. In this work, the AM shall be restricted to suppress those artifacts that, due to a combination of scattered radiation, beam hardening, and nonlinear partial volume effects, result in attenuation values that become lower than zero and are thus unphysical. Such artifacts are often found in CT between strong absorbers (e.g. metals), where they show up as high-frequency dark streak artifacts in the volume. With this assumption, a generation rule for this mask is relatively easy to

define and was performed here as described in algorithm 2 and is summarized in the following:

First, a threshold $\mathrm{CT_A}$ is set, below which a gray value is considered artifact-induced, and all voxels with CT values $\mathrm{CT} \leq \mathrm{CT_A}$ are deposited in a binary image in which they have the value zero and all other voxels have the value one. The artifact threshold was set here at $\mathrm{CT_A} = -1315\,\mathrm{HU}$, which excludes air ($-1000\,\mathrm{HU}$) and contains most of the artifact-induced streaking. To remove noise-induced misallocations of voxels from the mask as well as to force smooth transitions, the binary image is smoothed. This is done here with a three-dimensional isotropic Gaussian filter whose standard deviation corresponds to that of the filter found via Eq. (4.1). Next, by logarithmization, clipping and taking the square root, non-linear operations are performed on the artifact mask to steepen it and give more weight to the artifact edges. The artifact mask thus generated is multiplied onto the high-pass filtered Micro volume and reduces the carryover of high frequencies in image regions with high-frequency artifacts (see Fig. 4.3). However, it should be noted again at this point that this is a simplification to filter out high-frequency artifacts. High-frequency artifacts that are not adequately suppressed in the mask, e.g. those with CT values greater than $\mathrm{CT_A}$, could still be transmitted.

.

Algorithm 2 Pseudocode for the artifact mask generation.

1: if($\mathrm{CT_{Micro}}(x,y,z) \leq \mathrm{CT_A}$) $\mathrm{AM_{binary}}(x,y,z) = 0$, else $\mathrm{AM_{binary}}(x,y,z) = 1$
2: $\mathrm{AM}(x,y,z) = \mathcal{N}(0,\,\sigma^2) * \mathrm{AM_{binary}}(x,y,z)$
3: if($\mathrm{AM}(x,y,z) > 0$) $\mathrm{AM}(x,y,z) = -\ln(\mathrm{AM}(x,y,z))$, else $\mathrm{AM}(x,y,z) = 1$
4: if($\mathrm{AM}(x,y,z) > 1$) $\mathrm{AM}(x,y,z) = 1$
5: $\mathrm{AM}(x,y,z) = \sqrt{\mathrm{AM}(x,y,z)}$
6: invert artifact mask: $\mathrm{AM}(x,y,z) = -\mathrm{AM}(x,y,z) + 1$

The spatial resolution-optimized and artifact-reduced FSDECT volume is finally obtained by adding the high-pass information from Eq. (4.4) to the DECT volume, weighted by the artifact mask and a linear factor:

$$f_{\mathrm{FSDECT}}(x,y,z) = f_{\mathrm{DECT}}(x,y,z) + \gamma\,\mathrm{AM}(x,y,z)\,f_{\mathrm{Micro,\,HP}}(x,y,z) \tag{4.5}$$

The parameter γ corresponds here to a linear weighting factor that prevents overshoots at edges due to the contrast differences of Micro and DECT volumes. When volumes are rescaled to Housfield units, transitions from reference material to air are at one contrast level anyway, allowing a factor $\gamma = 1$. If other material transitions are of interest, the factor must be adjusted to the corresponding contrast levels C between the considered materials:

$$\gamma = C_{\mathrm{DECT}}/C_{\mathrm{Micro}} \tag{4.6}$$

4.2 Results

The results for the FSDECT data combination of the automotive controller measurements are shown in Fig. 4.5. Beam hardening and scatter artifacts are particularly visible as gray value inhomogeneities in areas of the same material, which should actually have similar densities, as well (e.g. the aluminum block of the automotive controller). On three exemplary volume slices it can be seen that the artifact content is the highest in the Micro volume and is already significantly decreased for the Macro volume, as it was expected. The DECT data fusion reduces the artifact content of the CT images even further. The artifacts are not completely vanished, as some very dense structures still lead to a certain shading of the gray values but the overall image quality is significantly improved compared to the Micro and Macro volumes. By applying the frequency split technique, small details from the Micro volume, which cannot be detected in the Macro and DECT volumes, can be restored in the FSDECT volume. Furthermore, the sharpness of edges is increased in the FSDECT volume, resembling the sharpness of the Micro volume. This improvement of spatial resolution is especially apparent in the small ROIs which are given for each CT image in boxes besides the full-slice overview image. In terms of artifact content, the FSDECT volume is in no way inferior to the DECT volume.

For each of the CT images shown in Fig. 4.5, a respective CT image is shown where ESC was used to remove scatter artifacts. DECT and FSDECT volumes with ESC correspond in this case to combinations of Micro and Macro volumes where each of the two volumes is scatter-corrected by ESC prior to the combination. It can be seen that by applying the empirical scatter correction to the Macro volume, most of the artifacts can already be eliminated. However, beam hardening artifacts, such as those occurring in regions with metal pins in Fig. 4.7, for instance, are still present and require correction with DECT or FSDECT. In general the FSDECT volume with ESC provides the least systematic measurement deviations and thus the best image quality regarding scatter and beam hardening artifacts and spatial resolution.

The improved spatial resolution in the FSDECT volume can also be measured. Figure 4.6 shows an evaluation of the MTF of the DECT and FSDECT volumes in addition to those shown in Fig. 4.4. As expected, the DECT MTF curve aligns well with those of the Macro and smoothed Micro volumes whilst the FSDECT MTF curve closely resembles that one of the Micro volume. The MTF = 10 % values are at 2.59 lp/mm, 1.55 lp/mm, 1.55 lp/mm, 1.85 lp/mm, and 2.63 lp/mm for the Micro, Macro, smoothed Micro, DECT, and FSDECT volumes, respectively.

One obvious drawback of the methods presented here is the accumulation of image noise, which can be observed in the corrected volumes from Fig. 4.5. The empirical scatter correction approximates the scatter signal by low frequency basis images. Noise induced by scattered radiation cannot be eliminated by ESC, which is also the case for all other state of the art software-based scatter correction methods [27], [34]–[41]. One would need to prevent scatter artifacts in first place, e.g. by one- or two-dimensional antiscatter grids (ASGs) [53]–[56], [160], [161], in order to avoid the noise induced by scatter in the data and to achieve higher signal-to-noise-ratios. By subtracting a smooth

	image noise without ESC	image noise with ESC	CNR without ESC	CNR with ESC
Micro	45 HU	76 HU	7.3	8.1
Macro	30 HU	43 HU	10.7	14.7
DECT	62 HU	76 HU	7.5	8.5
FSDECT	63 HU	79 HU	7.4	8.1

Table 4.2: Image noise evaluated in an ROI in the aluminum block of the automotive controller volumes shown in Fig. 4.5 and CNR evaluated between aluminum and air in the same data.

scatter estimate from the rawdata, the noise level therefore automatically increases. This is why ESC and other software-based scatter corrections lead to a noise increase, which can be observed in Fig. 4.5. On the other hand, contrasts are generally increased by effective scatter corrections, which leads to favorable contrast-to-noise-ratios, after all. However, along line integrals of high attenuation with large scatter-to-primary ratios one may find directed noise artifacts that are particularly noticeable and may lead to biases when measures are taken (cf. ROI 2 of the ESC-corrected Micro volume in the bottom row of Fig. 4.5). As shown in Eq. (2.57), the DECT combination of the data increases image noise, as well. Unlike ESC, this method also results in reduced CNRs. Since the noise resides in the high spatial frequencies of an image, the frequency split further increases image noise by transferring these high frequencies to the DECT volume (cf. Fig. 4.3). In summary, an increase in image noise is obtained at every step of the correction (scatter correction, DECT combination, and frequency split). Table 4.2 shows a quantitative evaluation of the image noise and CNR between aluminum and air, which confirms this theoretical consideration and the qualitative impression from Fig. 4.5. The image noise in this table was evaluated in a homogeneous ROI within the aluminum block of the automotive controller at z-position $z = 96\,\mathrm{mm}$ (cf. Fig. 4.5) and an air region close to the workpiece surface was analyzed to calculate the aluminum-air CNR. In order to exclude the influences of artifacts or other CT value inhomogeneities in this noise quantification, an adjacent axial slice ($+0.5\,\mathrm{mm} = +5$ slices) was subtracted from the considered axial slice and the noise in the difference image was rescaled by the factor $1/\sqrt{2}$.

Fig. 4.7 emphasizes the necessity of the artifact mask: in a region of an electronic connector, where the automotive controller has dense metal pins and low-density Polybutylenterephthalat (PBT) plastic parts, beam hardening artifacts lead to high frequency streak artifacts. These artifacts can be eliminated by DECT but they reappear in FSDECT, when no artifact mask is used. If an artifact mask is used, however, a transfer of these high frequency artifacts is strongly reduced. All data shown in this figure are scatter corrected using ESC.

The blending factor for the volume combinations shown in Figs. 4.5 to 4.7 was set to $\alpha = -0.74$ for the combinations without prior scatter correction and to $\alpha = -0.6$ for those with ESC.

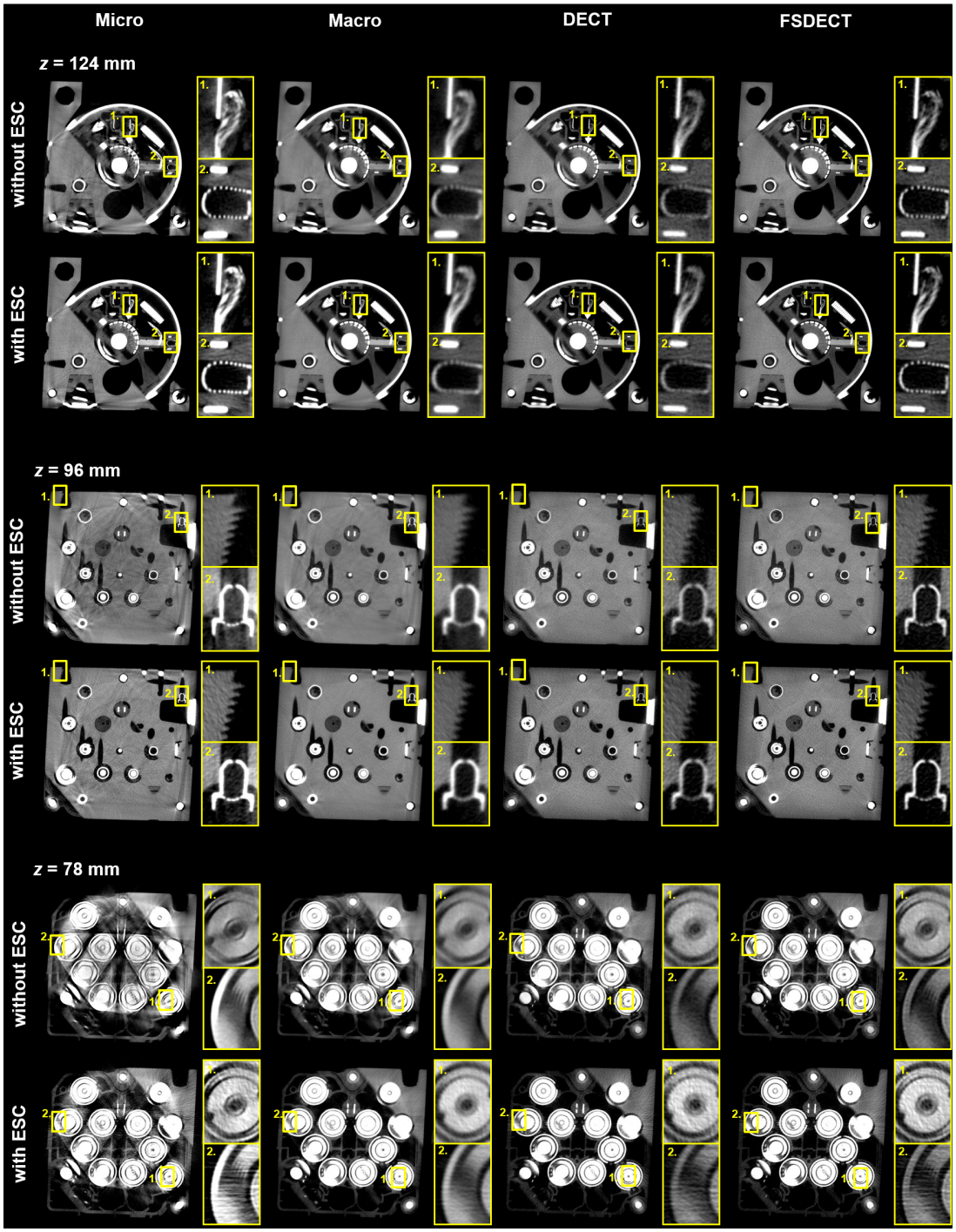

Figure 4.5: Three exemplary volume slices ($C = 0\,\text{HU}$, $W = 1500\,\text{HU}$) for the Micro, Macro, DECT, and FSDECT data for a measurement of an automotive controller at the MultiSpek CBCT system with the scan parameters from table 4.1. The yellow boxes depict regions of interests, which are shown in a close-up beside each volume slice. Each slice is given for two scenarios: once without any prior scatter correction and once with ESC.

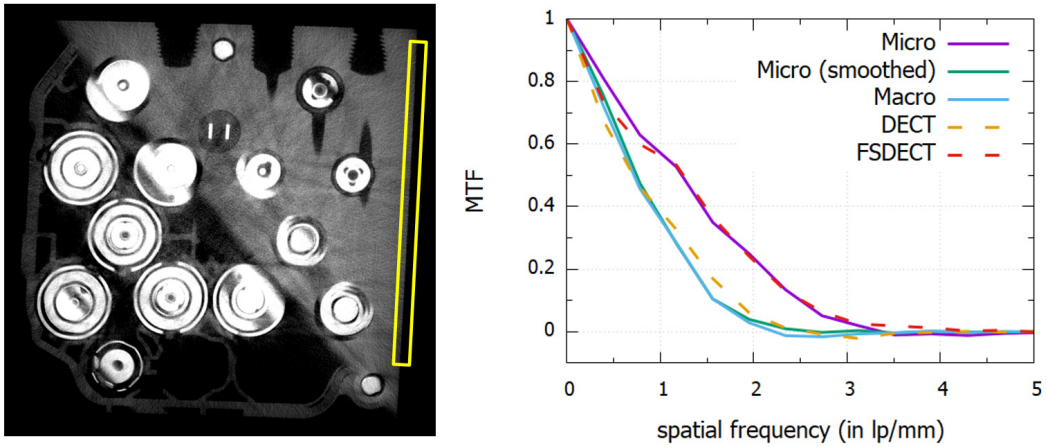

Figure 4.6: Left: FSDECT volume slice ($C = 150\,\text{HU}$, $W = 1700\,\text{HU}$). The yellow box depicts the edge position at which the MTFs are determined. Right: MTF curves of the Macro, Micro, smoothed Micro, DECT and FSDECT volumes.

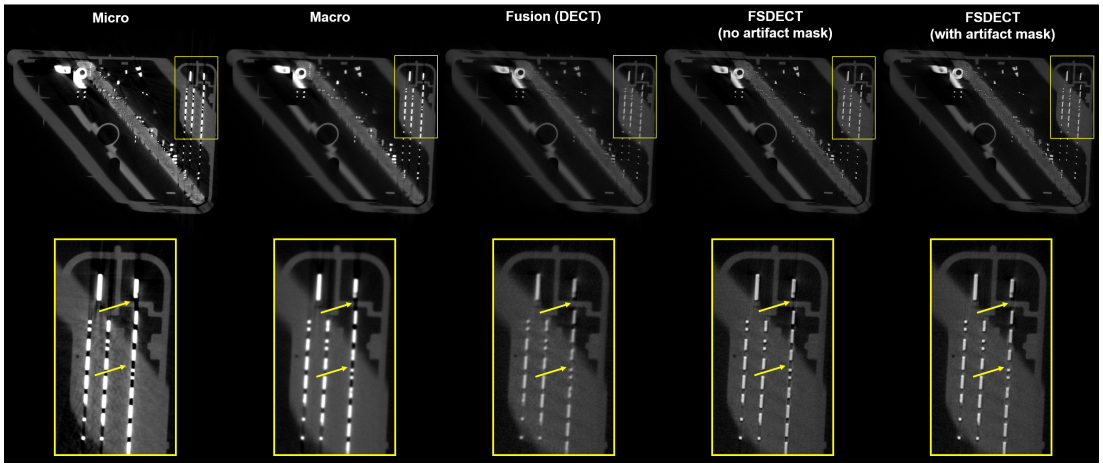

Figure 4.7: Top: exemplary axial volumes slice at $z = 54\,\text{mm}$ of the Micro, Macro, DECT, FSDECT without artifact mask, and FSDECT with artifact mask volumes (left to right). Bottom: ROIs of the connector area in this slice for the different volumes. The yellow arrows mark areas of interest. $C = 0\,\text{HU}$, $W = 2000\,\text{HU}$.

4.3 Discussion

The results show that by using ESC and an FSDECT data combination even severe scatter and beam hardening artifacts can be corrected. Furthermore, the frequency split technique increases the spatial resolution of the corrected fusion volume up to a level of that of the Micro volume (cf. Fig. 4.6). As a result, the methods presented in this work for reducing systematic measurement deviations in CT systems that employ two x-ray tubes of different designs offer a way to inspect previously inadequate workpieces, such as the automotive controller, by CT scans and to determine precise dimensions on them. This is particularly evident in Fig. 6.6 in chapter 6 of this work, where it is shown that automatic surface determinations and measurements of inner drilling holes of the automotive controller, which are of particular interest to the manufacturer from a metrological point of view, are only possible using the image quality improvement procedures described here.

A limitation of the FSDECT approach shown here is that a CT system with two x-ray tubes of different designs, such as the MultiSpek CBCT, is required to fully exploit the benefits of each measurement with a different x-ray tube. Such a CT system is therefore associated with higher costs. However, for the correction of non-aligned volume data, one can imagine an alternative variant of the presented FSDECT algorithm, in which a rigid volume registration takes place before the actual FSDECT data combination. This allows a workpiece to be measured on two different CT devices with micro- and macrofocus x-ray tubes at different spectra, and these measurements can then be combined after the rigid registration of the volume data using the methods described here to reduce systematic measurement deviations whilst maintaining the spatial resolution of the high-resolution dataset. The advantage of this method is that while CT devices with two x-ray tubes, such as the MultiSpek CBCT device, correspond to rather exotic industrial CT setups, different CT devices with different x-ray tube types and tube voltages may already be available in some production halls. Furthermore, the here proposed algorithm may be useful for dual energy CT measurements at a single source CT system, as well. DECT measurements in industrial CT setups are typically performed by sequential measurements of the same workpiece at different tube voltages and prefiltration. Until now, it has been the responsibility of the user to ensure that there is little difference in the resolution of the datasets acquired in this way, to allow artifact-reducing combinations of the spectral datasets. This is typically achieved by adjusting the tube power for both measurements, or explicitly increasing the focal spot size by increasing the defocus current at the x-ray tube [129] of the measurement with smaller focal spot, so that the focal spot size is approximately the same for both measurements. With the FSDECT algorithm, neither an adjustment of the tube power nor the defocusing of the focal spot of a measurement is necessary. The advantages of this method are therefore on the one hand that the tube power of a measurement, mostly the measurement with high photon energies and strong prefiltration, does not have to be reduced, which results in a shorter measurement time at the same SNR, or that the resolution of the measurement is not degraded by a focal spot defocusing, but is determined by the measurement with the smaller focal spot size.

The algorithm proposed here to improve the structural resolution due to different focal spot sizes of two CT measurements cannot be directly applied to medical applications, since high power x-ray tubes with constant focal spot size are typically used in clinical CT and interventional CBCT. However, it is conceivable to use the FSDECT algorithm to adjust the structural resolution of volume data where a dataset has reduced spatial resolution due to increased detector binning. The methodology from section 4.1.2 can be used analogously for this purpose. This plays a particular role for novel dual source MSCT systems that include a photon counting as well as an energy integrating detector, or two photon counting detectors that have greatly reduced pixel sizes compared to energy integrating detectors (cf. Sec. 5.3.1). For a dual source MSCT with one photon counting detector and one energy integrating detector, FSDECT can be used to obtain an artifact-reduced combination volume with the spatial resolution of the PCD. In systems with two PCDs, one of the detectors may take unbinned data to obtain the maximum spatial resolution, while the other detector takes binned data to be able to use a higher number of energy thresholds, for example. FSDECT then makes it possible to combine the spectral data recorded in this way to a volume with a reduced amount of artifacts that has a spatial resolution similar to that of the unbinned data. The further spectral information obtained at the binned detector can then be used for noise reduction, for example.

The above mentioned benefits of reduced systematic measurement deviations at high spatial resolution come at a cost of lowered signal-to-noise ratios and an associated loss of contrast-to-noise ratios, however. One simple way to improve the signal-to-noise ratio in the artifact corrected volumes without changing the experimental setup would be to increase scan times. However, this is unwanted for obvious reasons. Also other scan parameters might be chosen to increase the SNR. For instance increasing the tube power or reducing the prefilter thickness would result in higher photon fluxes and therefore improve the statistics. However, these are no viable options, as well. Taking a look at table 4.1, one sees that the microfocus tube already operates at a tube power of 80 W, which corresponds to the maximum power of the used microfocus x-ray tube. A reduction of the prefilter thickness or choosing a less dense prefilter material would have a negative impact on the amount of artifacts. As all signals have to be within the dynamic range of the detector, meaning that x-rays exposed to a strong attenuation must yield a sufficient signal whilst x-rays which only pass air must still yield a measureable signal, an optimal choice of scan parameters is often not obvious and should be determined by simulations [162], [163] or experiments. Therefore, another post-processing solution to reduce the image noise in the artifact reduced datasets is pursued in this work. Such a method and the corresponding results are discussed in chapter 6 in further detail.

Another possibility to reduce the statistical measurement deviations could be the use of a direct converting detector. It is known from clinical CT applications that photon-counting computed tomography (PCCT) may have favourable properties concerning signal-to-noise and contrast-to-noise ratios [60], [61]. The feasibility of using spectral data from a PCD for the reduction of systematic measurement deviations and potential benefits compared to energy integrating DECT are explored in the next chapter.

5 Potential Benefits for the Reduction of Systematic Measurement Deviations in X-Ray Computed Tomography by using Photon Counting Detectors

The previous chapter showed how DECT and FSDECT can be used for image quality improvement of spectral CT datasets. In industrial CT applications, workpieces are usually scanned sequentially with different tube voltages and prefilters to obtain such spectral CT datasets. In clinical CT, where dual energy CT has a longer history for material decomposition among other things, other techniques, such as simultaneous dual source operation, tube voltage switching, sandwich detectors, and most recently the development of CT systems equipped with photon counting (PC) detectors are known for dual or multi energy CT acquisitions [164].

The most obvious advantage of using an energy-selective detector to obtain spectral data in industrial CT applications is that the workpiece would not have to be scanned twice with different spectra. This reduces the measurement effort and positioning times of the workpiece can be reduced.

As described in section 2.1.4, PC or direct converting detectors allow measurements of single photons and charge thresholds allow to count photons above a desired energy. Photons with energies between two distinct energy thresholds are assigned to so-called energy bins. The reconstructions of these bin data are called bin images. This chapter addresses the applicability of PCCT data for artifact reduction in industrial applications, which has recently become a growing field of interest [23], [24]. For this purpose, the use of energy thresholds to reduce systematic measurement deviations in the reconstructed volume is investigated through simulations and experiments. In addition, the combination of bin images using pseudo-monochromatic imaging techniques for artifact reduction will be examined.

5.1 Basic Idea

As is known from section 2.3.2, beam hardening artifacts are related to the energy-dependent, nonlinear behavior of the attenuation coefficients, as well as the polychromatic nature of the x-ray spectrum. A reduction of the spectral width of the x-ray spectrum, as well as a shift of the center energy of the spectrum towards higher energies, where the energy-dependent variation of the attenuation coefficients is relatively small, thus lead to a reduction of beam hardening artifacts. This effect is usually achieved by filtering the spectrum with physical prefilters (cf. Fig. 2.5). Energy-selective detectors provide an alternative possibility: by setting energy thresholds, high energy photons can be selectively reconstructed to shift the center energy of the detected spectrum and reduce its energy range. Accordingly, for PCCT measurements, one could imagine using energy thresholds instead of physical prefilters, which also absorb a portion of the high-energy photons and thus negatively affect the signal-to-noise ratios. The potential benefits of such an approach over strong prefiltration are therefore evaluated in a simulation study, which is explained in the following section in more detail.

In CBCT setups with broad collimation and without anti-scatter grids, setting an energy threshold can additionally be useful to reduce the number of detected scattered photons. In theory photons lose energy in the process of Compton scattering (cf. Sec. 2.1.2), so that fewer photons from scattering interactions feature in the high-threshold data. Studies have shown that the reduction of scatter signals may be as high as 20% in CBCT scans with a PC dector compared to an energy-integrating (EI) detector by simply using a threshold for the data acquisition [24]. Since prefilters are usually placed in front of the object in CT scans, they cannot reduce the scatter intensities and may even lead to scatter signals themselves [132]. Therefore, this simple approach of setting an energy threshold to selectively measure high-energy photons targets two distinct types of artifacts.

In principle, narrow energy bins at the PC detector could also lead to a substantial reduction of beam hardening artifacts. This approach for beam hardening reduction is rather impractical, though, as only few photons would fall into a narrow energy bin. Moreover, due to the limited spectral separation of the PC detector, which will be discussed in the following section in more detail, photons contributing to a narrow energy bin are not as monochromatic as one would naively assume.

Since the data in different energy bins have different spectral characteristics, it is expected that by a DECT combination (Eq. (2.56)) of two bin images, a reduction of artifacts can also be achieved for PCCT. An experimental verification of this is shown in section 5.3.3.

5.2 Simulation Study

To evaluate the potential benefits of direct converting detectors for reducing systematic and statistical measurement deviations, detector signals are simulated for PC and EI detectors and are evaluated in terms of beam hardening artifacts and signal-to-noise ratios.

In order to model the spectral separation of the photon counting detector, the semirealistic detector model (SRDM) of Faby et al. [102] was used to simulate the bin sensitivity of the detector. The bin sensitivity one obtains from this model describes the fraction of the original spectrum that is detected in an energy bin of the PC detector. The spectrum that is detected by a PC detector in energy bin i is therefore given by

$$w_i(E) = w_\mathrm{t}(E)\,\kappa(E)\,b_i(E) \tag{5.1}$$

where $w_\mathrm{t}(E)$ denotes the emitted tube spectrum, which was simulated with the model of Tucker et al. [81] in the following, $b_i(E)$ is the bin sensitivity of energy bin i at a given energy E and $\kappa(E)$ the prefiltration known from Eq. (2.12). Compared to equation (2.18), the detector efficiency $\eta(E)$ is missing here. The reason for this is that the detector efficiency is included in the bin sensitivities of the SRDM.

The SRDM takes into account several effects that degrade the spectral properties of a PC detector (cf. Sec. 2.1.4), in particular charge sharing, K-escape, and Compton scattering. These effects lead to disturbances of the spectral information and as a consequence may reduce the amount of photon flux observed in the high energy bin, which corresponds to the data of interest for the here proposed artifact correction method. Counting rate dependent effects (pulse pileup) are not accounted for by this model, however.

Figure 5.1 shows the bin sensitivities and a 140 kV spectrum for such a PC detector model. These bin sensitivities and the corresponding realistic bin spectra are obtained for a 1.6 mm CdTe sensor, a pixel size of 225 µm, a bias voltage of 500 V, and with energy thresholds at 20 and 90 keV, respectively. It should be noted that due to charge sharing the bin sensitivity may exceed unity. The resulting realistic bin spectra from the SRDM are compared to idealized bin spectra in which all spectral distortions are neglected. It can be seen that the low-energy bin for the realistic spectrum also contains a large fraction of high-energy photons beyond the energy threshold of 90 keV. In the high-energy bin, the realistic simulation produces a lower photon intensity compared to an ideally energy-resolving detector, but the covered spectral range is nearly the same for the realistic and ideal detector. The investigated 140 kV spectrum corresponds to that of an x-ray tube with reflection target with an anode angle of seven degrees. It is prefiltered only by inherent tube components (1 mm aluminum, 0.89 mm titanium, and 0.008 mm tungsten) and a bowtie filter, which is modeled with 1 mm carbon[1]. These values are consistent with those of the experimental CT system that is used for the experimental investigations (see Sec. 5.3) and are therefore used for the simulation study in the following.

[1]This corresponds to the thickness of a typical bowtie filter at its center, which is a good approximation for the spectrum of the measurement in section 5.3, since the investigated object only covers the center of the FOM.

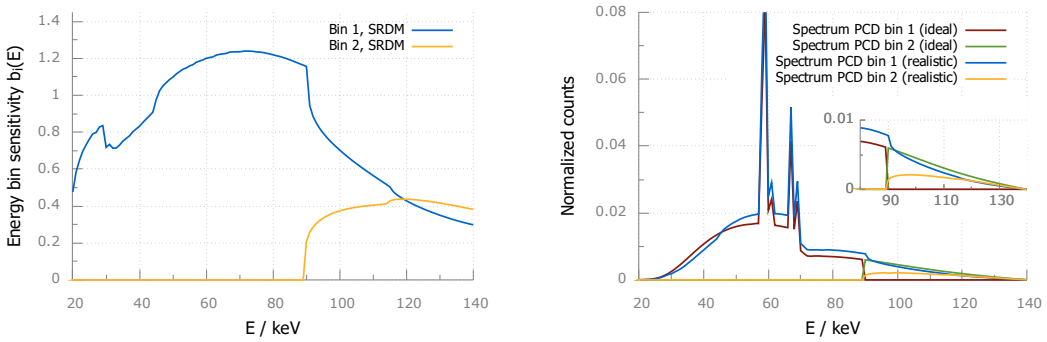

Figure 5.1: Left: Energy-dependent bin sensitivities of a PC detector simulated with the SRDM from reference [102]. The energy bins range from 20 to 90 keV and 90 to 140 keV in this simulation. Right: Four spectra showing the ideal x-ray spectra as recorded by the two bins of the PC detector (red and green), and the spectra recorded by bin 1 and bin 2 of a realistically modelled PC detector (blue and yellow) as calculated with the SRDM bin sensitivities on the left. The inlay shows a close-up of the 80 keV to 140 keV range.

To quantify the expected amount of beam hardening artifacts for simulated spectra such as those from figure 5.1, a measure needs to be defined that indicates the measurement deviations obtained due to the polychromatic x-ray spectrum. A well-suited measure for the monochromaticity of a spectrum and thus the severity of beam hardening artifacts in CT scans is the homogeneity factor (HF). The HF is defined as the division of the first and second half-value layer ($\mathrm{HVL}_{1,2}$) for a certain attenuator a.

$$\mathrm{HF} = \frac{\mathrm{HVL}_1}{\mathrm{HVL}_2} \tag{5.2}$$

The HVL defines the thickness of the material that reduces the measured signal by 50%:

$$\int dE\, w(E)\, e^{-\mu_\mathrm{a}(E) \sum_i \mathrm{HVL}_i} = \frac{1}{2^i} \tag{5.3}$$

In this equation $w(E)$ corresponds to the normalized detected spectrum from equations (2.18) or (5.1). For monochromatic spectra the HF yields one whereas for polychromatic spectra this quantity yields values smaller than one. The smaller the HF, the more beam hardening is present.

In principle, high HF values can, for instance, be achieved by strong prefiltration of the spectrum, or by high energy thresholds. But in practice this is only useful up to a certain degree, because a large part of the emitted x-ray radiation then remains undetected or is already absorbed by the prefilter, which results in poor signal-to-noise ratios in the measurement. Therefore, when considering the HF for a CT measurement, the corresponding SNR must also be taken into account. As the number of detected

photons follows Poisson statistics for PC detectors the variance of measured counts equals the expectation value. The resulting SNR is then given by

$$\mathrm{SNR}_{\mathrm{PC}} = \sqrt{N_0\, A_{\mathrm{Q,PC}}} \tag{5.4}$$

with N_0 denoting the total number of photons and $A_{\mathrm{Q,PC}}$ the quantum efficiency of the PC detector. If the photon signal is integrated rather than counted, as it is the case for EI detectors, an additional factor, the so-called Swank factor S [165], [166] needs to be taken into account:

$$\mathrm{SNR}_{\mathrm{EI}} = \sqrt{N_0\, A_{\mathrm{Q,EI}}\, S} = \sqrt{N_0\, A_{\mathrm{Q,EI}}}\, \frac{\int E\, w(E)\, dE}{\sqrt{\int E^2\, w(E)\, dE}} \tag{5.5}$$

The Swank factor, which yields one for PC detectors (see Eq. (5.4)), is smaller than one for EI detectors and therefore indicates a reduced SNR for EI detectors compared to PC detectors for the same effective spectra and quantum efficiencies. A proof of this is shown in the appendix 8.1.

In order to calculate the SNR for EI and PC detectors in the simulation study here, the same 140 kV spectrum as mentioned above with only inherent prefiltration is used as a basis. A photon number of $N_0 = 50,000$ emitted photons per detector pixel is assumed for the unattenuated spectrum. Signal losses due to a limited detector efficiency or bin sensitivity and optional additional prefiltration are included in the factors $A_{\mathrm{Q,PC}}$, and $A_{\mathrm{Q,EI}}$, respectively.

Figure 5.2 shows plots of SNRs against HFs for different detector types, where for EI detectors additional tin prefiltration of varying thickness was used to increase the HF, whilst for PC detectors energy thresholds are used for this purpose. Similar image quality with respect to beam hardening artifacts are expected at similar HF values and higher SNRs depict a better image quality regarding noise in the respective data. Two detector materials are investigated for EI detectors: a 1.4 mm layer of gadolinium oxysulfide (GOS), which corresponds to a typical material and thickness of an EI detector in MSCT, and a 0.55 mm layer of cesium iodide (CsI), which is a common detector material and thickness for EI flat detectors used for CBCT [167]. Furthermore, a PC detector was simulated with a cadmium telluride (CdTe) semiconductor of 1.6 mm thickness with a pixel size of 225 µm. As mentioned previously, this corresponds to the detector used in the experimental investigations in the following section. In order to generalize the results with respect to different semiconductor thicknesses, data points for sensor thicknesses of 0.75 mm and 2 mm were added for energy thresholds of 70, 80, and 90 keV. This roughly corresponds to the range of CdTe thicknesses used for PC flat detectors [168]. Four different sample materials, iron, copper, aluminium, and water are examined in this simulation. The prefilter thicknesses were adjusted such that the HF of the EI detector data points (CsI and GOS) correspond to those of the PC detector data points (1.6 mm CdTe) at the different energy thresholds for iron as the sample material under investigation and the thus-obtained prefilter thicknesses are then consistently used also for the other materials. The plots in Fig. 5.2 show that even though the

prefilter thicknesses are adjusted for iron samples, the HF values are similar for EI and PC simulations with these prefilter thicknesses and energy thresholds for the other sample materials, as well.

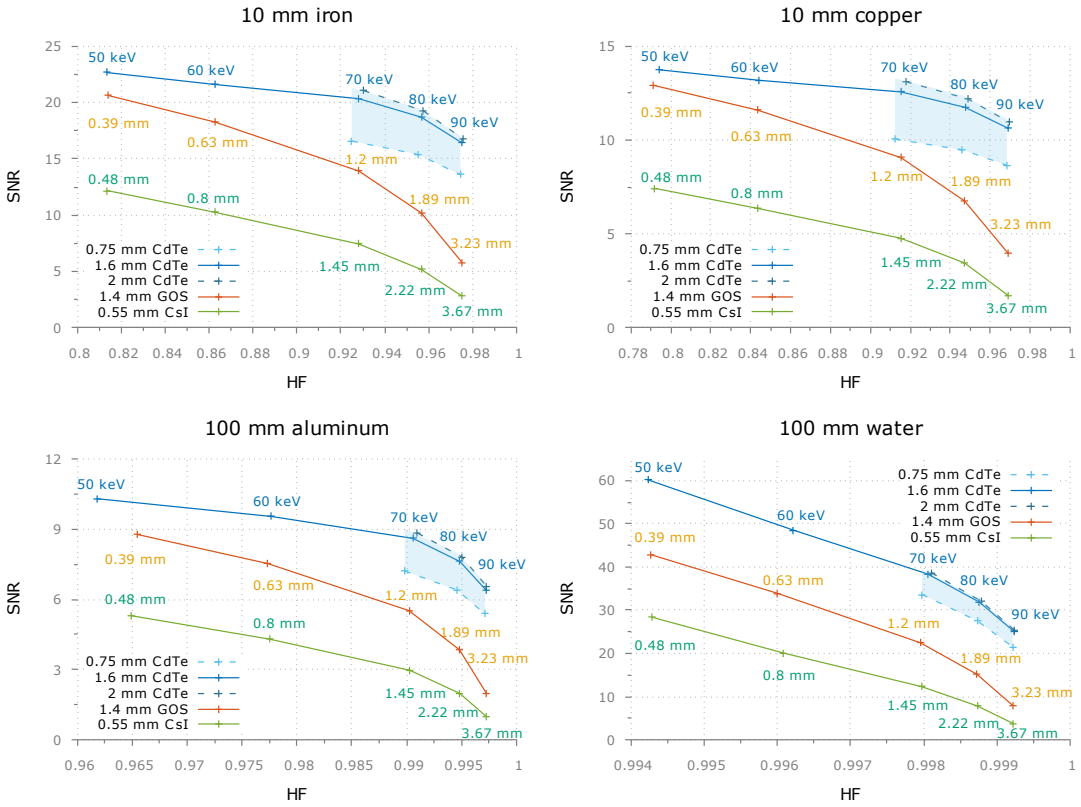

Figure 5.2: The four different plots in this figure show simulated comparisons of signal-to-noise ratios (SNR) and the homogeneity factor (HF) for different detectors and energy thresholds or prefilters. Four different attenuators are considered: iron (10 mm), copper (10 mm), aluminum (100 mm), and water (100 mm). The orange curves correspond to simulations with an EI detector with a 1.4 mm layer of GOS and the green curves depict the results for an EI detector with a 0.55 mm CsI scintillator. Tin prefilters of different thicknesses, which are given besides each datapoint, are applied to the spectra. The blue curves correspond to simulations with a PC detector with a CdTe semiconductor of different thicknesses (see legend). Instead of physical prefilters, energy thresholds are used to increase the HF for the PC data.

Qualitatively this simulation study shows that it is favorable to use an energy threshold at a PC detector instead of strong prefiltration at EI detectors to reduce beam hardening artifacts because of higher SNRs at similar HFs. This is true for all of the considered materials, even though quantitatively there are small differences. Especially at high

HF values, thus a low amount of beam hardening artifacts, a PC acquisition with energy thresholds outperforms conventional EI acquisitions with strong prefiltration regarding resulting SNRs. For the iron dataset the 1.6 mm CdTe PC detector with a 90 keV energy threshold yields an SNR improvement factor of 2.8 compared to a 1.4 mm GOS detector with 3.23 mm tin prefiltration and 5.8 compared to a 0.55 mm CsI detector with 3.67 mm tin prefiltration. Even though this benefit is reduced for thinner semiconductors, an advantage is still observed for thresholds beyond 70 keV and CdTe layers thicker than 0.75 mm for all materials. Detectors with GOS as scintillator material need less prefiltration to obtain a certain HF value compared to those with CsI scintillators. This is mainly due to higher absorption efficiency of GOS at high photon energies, which is depicted in Fig. 8.1 in the appendix 8.1. For this very reason, GOS detectors generally yield a higher SNR compared to CsI detectors in Fig. 5.2.

The results shown in Fig. 5.2 are based on a consideration of the detected x-ray intensities. To test how the different approaches for beam hardening artifact reduction affect CT volumes, a full CT dataset was simulated for a virtual phantom. The virtual phantom consists of a water cylinder with a diameter of 100 mm in which two iron cylinders with a diameter of 5 mm each are embedded.

For the simulation of the CT measurement, a fan-beam geometry with a focus to detector distance of one meter and a focus to isocenter distance of 750 mm was used. A total of 1200 projections were simulated equidistantly for a circular scan. The size of the detector in lateral direction was simulated as 1024 pixels with a dimension of 0.2 mm each and the voxel size of the reconstructed volume is 0.1 mm.

Polychromatic projection values were computed using equation (2.20) for different spectra and Poisson noise was added to the projection values. The spectra used here correspond to individual selected spectra from Fig. 5.2, again assuming a photon number of $N_0 = 50,000$ photons per detector pixel for the unattenuated emitted spectrum. Figure 5.3 shows the results for the reconstructions of the simulated data. For the EI detectors with 0.55 mm CsI and 1.4 mm GOS scintillator, respectively, results without prefiltering (full spectrum) and results with two different thicknesses of a tin prefilter (hardened spectrum) are shown. For the PC detector with 1.6 mm CdTe, results without energy threshold, as well as results with an energy threshold at 90 keV are shown. The prefilter size of the simulated measurements with EI detectors is chosen so that one time the noise within an ROI in the water cylinder corresponds to that of the scan with the PC detector at a threshold of 90 keV (0.62 and 1 mm tin, respectively) and one time the HF for iron (cf. Fig. 5.2) for the energy-integrating data is aligned with that of the photon-counting data at an energy threshold of 90 keV (3.67 and 3.23 mm tin, respectively). For the difference images, a monochromatic spectrum with a photon energy of 108 keV was used as reference. The noise-free and beam hardening-reduced volume data in the bottom rows of Fig. 5.3 are used to better illustrate remaining beam hardening artifacts for the hardened spectra, which are heavily obscured by noise in the middle row images.

The results in Fig. 5.3 show that CT images with a PC detector and a high energy threshold are superior to those with an EI detector and a thick prefilter, which confirms the theoretical consideration from figure 5.2. Beam hardening artifacts are weaker for

the threshold-based method using PCCT for volume data at similar noise levels. When PC and EI data are matched regarding beam hardening artifacts, the noise is stronger for the images with EI detector and prefilter-based beam hardening reduction. The results predict an increase in image noise by a factor of 3.2 and 6.8 in the water cylinder for the phantom simulated here. Since the signal-to-noise ratio increases with the root of the detected photons (cf. Eq. (5.4)), this corresponds to a measurement time reduction of more than 90% and 97% if the advantage of higher SNR with threshold-based PCCT is exchanged for reduced measurement times.

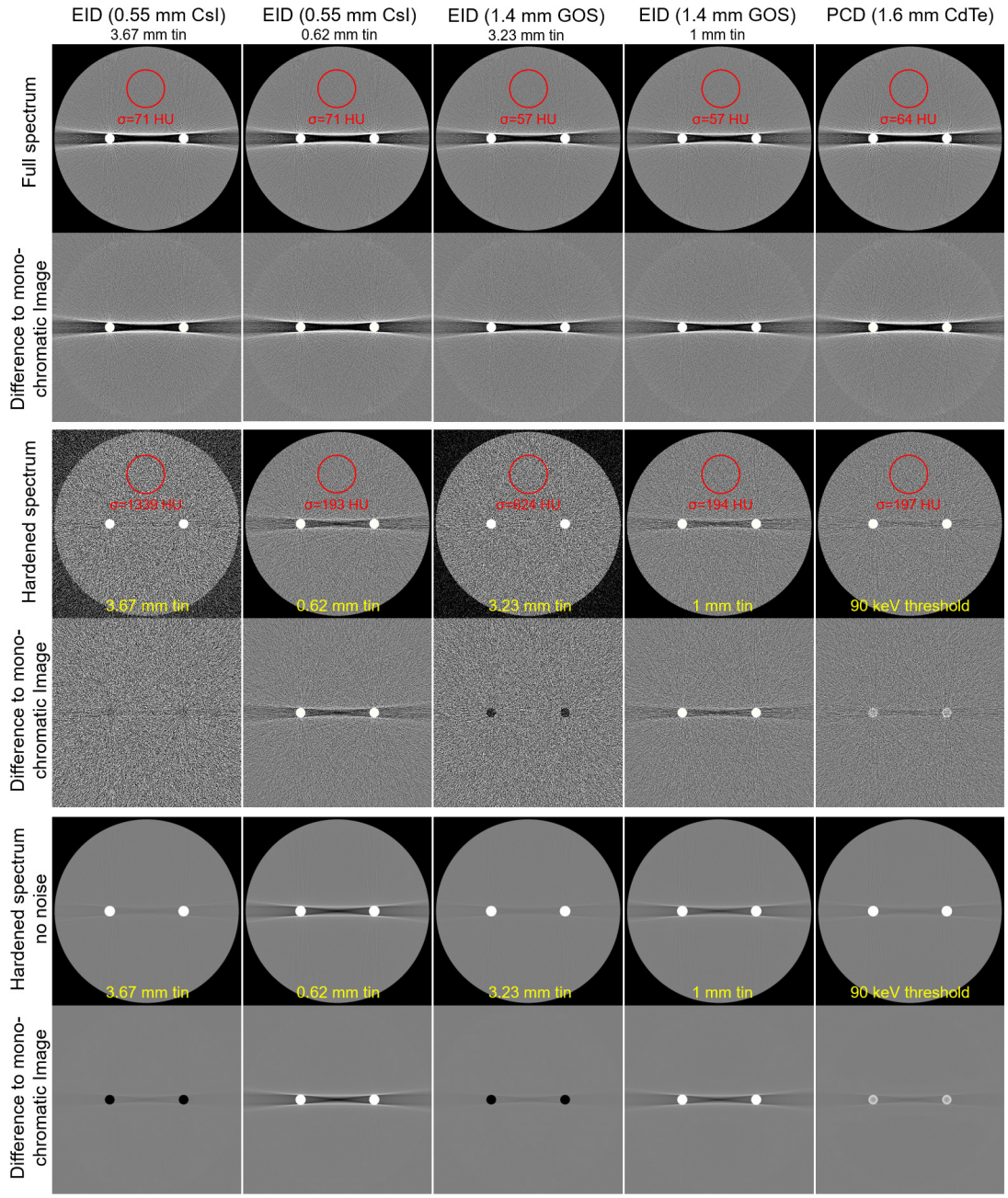

Figure 5.3: Simulated CT images for a water cylinder with two iron inserts and difference images with respect to the monochromatic ground truth. The first four columns depict simulations with EI detectors with different detector materials and prefilters. The last column shows the results for a PC detector. Results with no additional prefiltration or usage of an energy threshold are shown in the first row and results for spectra hardened by prefiltration or an energy threshold are shown in the second row. Image noise is evaluated in a homogeneous water region (red circle) and is displayed in each of these CT images. The CT images in the bottom row depict the same scenario as those in the middle row without simulating noise. $C = 0\,\mathrm{HU}$, $W = 1000\,\mathrm{HU}$.

5.3 Experimental Validation

As the simulation results and theoretical considerations show, energy thresholds on PC detectors can be used in order to efficiently reduce beam hardening artifacts. To verify this experimentally, a household electrical plug was measured at the Siemens SOMATOM CounT experimental PCCT (Siemens Healthineers, Forchheim, Germany). This experimental PCCT will be specified in the following and results for the threshold-based reduction of beam hardening and scatter artifacts are shown in section 5.3.2. Furthermore, spectral information of two energy bin images are used to further reduce artifacts, which is shown in section 5.3.3.

5.3.1 Material and Methods

All measurements shown in the following were performed using a tube voltage of 140 kV. This corresponds to the maximum selectable voltage on the PCCT device. Only inherent prefiltration (1 mm Al, 0.9 mm Ti, 0.008 mm W), a bowtie filter (1 mm C at the center) and a tube current-time product of 200 mAs were used in the following measurements. The rotation time of the gantry was always set to 1 s. As the SOMATOM CounT PCCT is a dual source CT employing one PC detector with a 1.6 mm CdTe semiconductor and one EI detector with a 1.4 mm GOS scintillator, direct comparisons between the technologies are possible. However, the PC detector has a smaller pixel-size (225 µm) compared to the EI detector (600 µm). A more detailed characterization of the SOMATOM CounT photon counting CT used for this study can be found in reference [103].

Every experiment here uses the so-called ultra high resolution (UHR) mode for data acquisition which benefits from the full spatial resolution of the PC detector and allows two energy thresholds to be set. Reconstructions of the EI detector data were performed with filtered backprojection using a B60 kernel, whereas reconstructions of PC detector UHR data were performed with filtered backprojection using a sharper U70 kernel, to take advantage of the smaller pixel size and better spatial resolution. The voxel size is $0.195 \times 0.195 \times 0.25\,\mathrm{mm}^3$ for each reconstruction.

The workpiece used in this experimental study is a standard household electrical plug, which corresponds to a complex multi-material object consisting of steel, copper and plastic elements, among others. To prevent truncation of attenuation coefficients that are significantly lower than air due to strong artifacts, which would negatively affect the effectiveness of the DECT combination of the bin images in section 5.3.3, the plug was measured in a water bath. Figure 5.4 shows photographs of the experimental PCCT system and the workpiece used for the experiments.

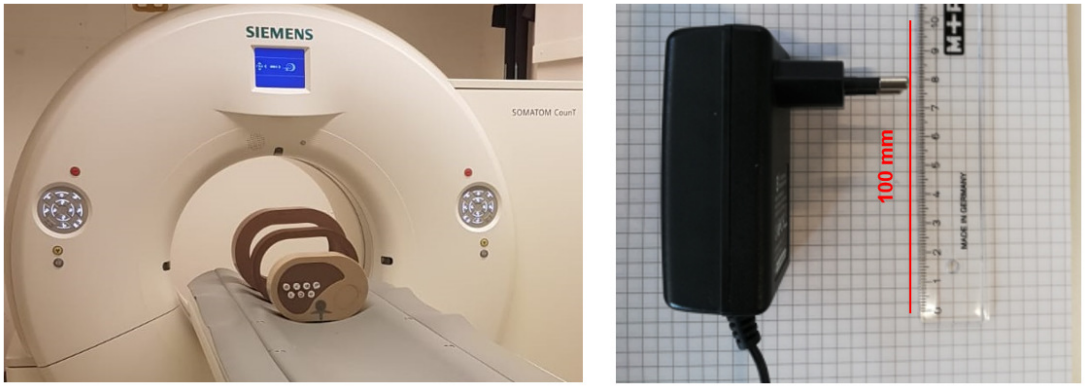

Figure 5.4: Left: Siemens SOMATOM CounT photon counting experimental CT system. Right: household electrical plug used for the experiments in sections 5.3.2 and 5.3.3.

5.3.2 Reduction of Systematic Measurement Deviations by Applying Energy Thresholds

Figure 5.5 shows that the reconstruction of PC detector data contains fewer streak artifacts for higher energy thresholds compared both to lower thresholds and to the reconstruction from an EI detector, which detects photons of all energies. Especially a comparison of the reconstruction with a threshold at 90 keV to the EI detector data shows the effectiveness of this rather simple approach for artifact reduction. On the contrary, the noise level is higher for the individual bins in a PC detector, which is obvious and was expected on the basis of the simulation study, as in total less photons are detected once an energy threshold for the detection is set, assuming that prefiltration is constant in both cases. Unfortunately, experimental verification of the prediction that the SNR for a threshold-based reduction of beam hardening using PCCT is advantageous over physical pre-filtering for EI detector measurements cannot be performed at this point because the experimental CT system does not allow for additional pre-filtering of data acquired with the EI detector. The lower spatial resolution of the EI detector apparent in figure 5.5 is a result of the larger pixel size and the correspondingly chosen smoother reconstruction kernel.

The detector considered in this study is optimized for the clinical use. Hence, anti-scatter grids prevent the detection of most of the scattered photons and a narrow collimation is used. Therefore, the advantage of the lower fraction of measured scattered photons due to higher energy thresholds is probably very small.

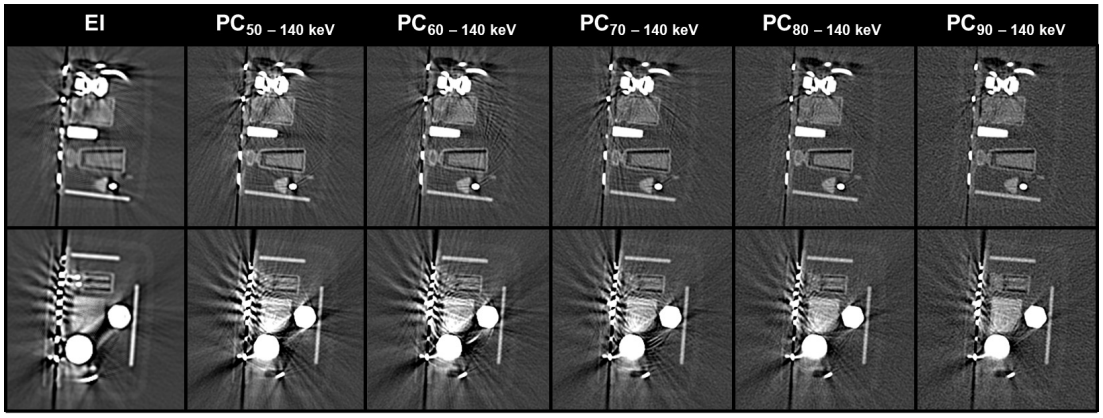

Figure 5.5: Reconstructed volumes of the household electrical plug measurement with an EI detector (left) and a PC detector with different energy thresholds. Top and bottom images correspond to axial slices of the volume at $z = 5.75\,\mathrm{mm}$ (top) and $z = 37.25\,\mathrm{mm}$ (bottom). $C = 1000\,\mathrm{HU}$, $W = 4000\,\mathrm{HU}$.

5.3.3 Reduction of Systematic Measurement Deviations by Dual Energy Combinations of Bin Images

In order to further reduce the beam hardening and scatter artifacts the spectral information of both energy bins provided by a single PCCT scan is used. Similarly to the spectral data of the MultiSpek CBCT system with two x-ray tubes from chapter 4, this can be done by a linear combination of two bin images for PC detector data. In contrast to the MultiSpek CBCT data, an adjustment of the spatial resolution of the spectral datasets is not needed here, since the bin images from the CounT system have a very similar spatial resolution.

A linear combination as given by Eq. (2.56) was performed on the data of the household plug from Fig. 5.5 with the highest spectral separation, which corresponds to energy bins at $T_1 \in [20, 90]$ keV and $T_2 \in [90, 140]$ keV. The results are shown in Fig. 5.6, where a blending factor of $\alpha = -0.26$ was used to obtain the DECT images. The yellow boxes in this figure mark a region of interest for which a close up is shown for each image. It can be observed that besides using high energy thresholds, a linear combination of the acquired bin images results in an additional decrease of beam hardening and scatter-induced streak artifacts.

Again the drawback of pseudo-monochromatic imaging for artifact reduction becomes apparent: the image noise is increased for the combined image compared to both input images. Equation (2.57) for the noise increase approximately holds true here because photon counting CT bin data show only minor correlations [102].

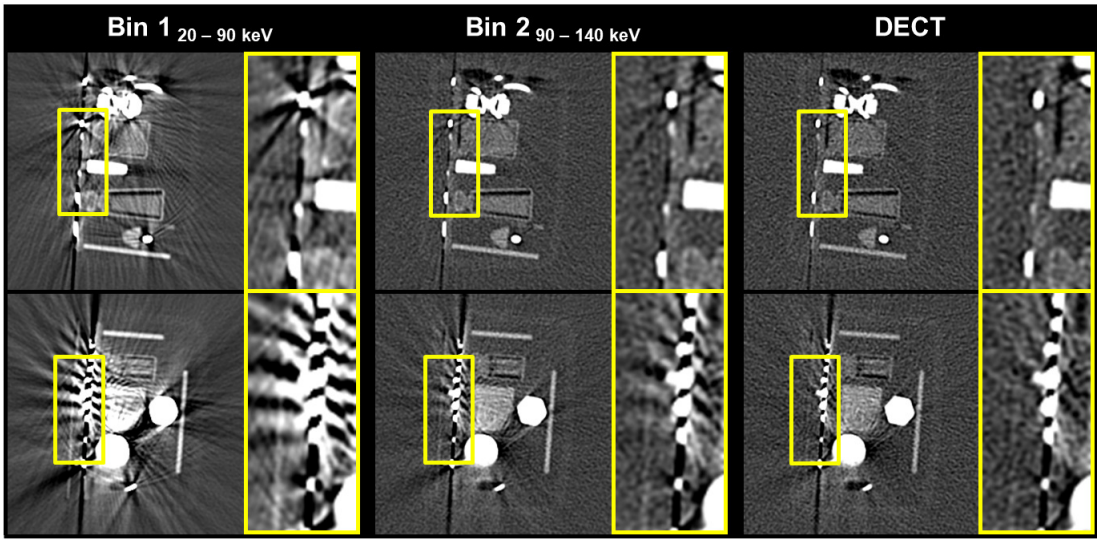

Figure 5.6: The two axial volume slices from Fig. 5.5 (top and bottom) of a low energy bin image (left) and high energy bin image (middle) for the measurement of the household electrical plug for energy thresholds at 20 keV and 90 keV. The CT images on the right show the DECT volume for a blending factor $\alpha = -0.26$. The yellow boxes show enlarged regions of interest. $C = 1000\,\mathrm{HU}$, $W = 4000\,\mathrm{HU}$.

5.4 Discussion

The results from the simulations as well as the measurements generally show the possibility of using energy thresholds at PC detectors to reduce beam hardening artifacts. This could be used in the future to scan workpieces with a reduced amount of systematic measurement deviations without having to resort to strong prefilters. Such a method offers advantages in terms of the expected signal-to-noise ratio at similar artifact levels, as shown by the simulation results. Increased signal-to-noise ratios can then be used either to increase image quality or to reduce measurement times.

The spectral data of the high energy bin can be flawed by pile-up effects, which are not modelled in the here-performed simulations. This could lead to worsened performances regarding beam hardening and scatter artifact reduction of the proposed method in real experiments. However, this is not too much of a problem, as this issue can be reduced by using small pixels as well as by a reduction of the photon flux. Since the tube powers and the associated photon flux for highly accurate industrial CT applications is many times lower than for clinical applications ($\mathcal{O}(100\,\mathrm{W})$ vs. $\mathcal{O}(100\,\mathrm{kW})$), and the pixel sizes for PC flat detectors typically even smaller than those of the experimental CT system considered here, the probability of pile-up effects is correspondingly low.

Effects such as charge sharing or fluorescence, which reduce the spectral resolution of a PC detector and were also included in the simulations, lead to a reduced count rate in high energy bins compared to an ideal scenario. If such effects can be reduced, the count rate in high energy bins would therefore increase, leading to an additional advantage of the here proposed energy threshold-based method for artifact reduction regarding the SNR. Some PC detectors already provide a correction of charge sharing by detecting signal coincidences for neighboring pixels and redistributing the charges accordingly to a single count [105]. This method works well, as long as the photon flux is relatively low, which typically is the case for highly accurate industrial CT applications, as described above.

One question left unanswered by the simulation results is how the spatial resolution behaves for measurements with a PC flat detector compared to measurements with an EI flat detector. Indeed, an increased image quality in terms of reduced systematic or statistical measurement deviations can only be evaluated as an actual advantage if the spatial resolution of the volume information obtained by the CT measurements is comparable. The measurement results on the experimental clinical PCCT device show that due to the smaller pixel size of the PC detector, measurements of CT volumes with higher spatial resolution are possible than it is the case for measurements using the EI detector at this computer tomograph. Flat detectors, as used in CBCT, often have smaller pixel sizes than the curved detectors used in MSCT. In addition, the crystalline structure of the CsI scintillator used in many EI flat detectors acts as a light guide (cf. Sec. 2.1.4), resulting in low crosstalk probabilities of signals onto adjacent pixels. Future investigations should therefore verify the simulation results from the previous section for measurements on PC and EI flat detectors and also test both technologies with respect to the PSF of the obtained signals.

At this point, it must be mentioned that the method of using energy thresholds instead of prefilters is only suitable for industrial CT applications where the radiation dose to the workpiece is irrelevant, which is the case for most workpieces. For patient scans, this method cannot be used because the high proportion of unfiltered low-energy photons would lead to an unacceptable dose increase. A clinically relevant application is given by a combination of prefilters and energy thresholds. It has been shown in reference [169] that an increased metal artifact reduction capability can be achieved at the same dose and with comparable noise levels.

PCCT also offers the possibility to use the obtained spectral data for further artifact reduction. It was experimentally confirmed for the measurement of the household electrical plug that such an artifact reduction can also be achieved for PCCT data using combinations of two energy bin images by pseudo-monochromatic imaging, similar to the procedure in chapter 4. In contrast to the previous chapter, where the fusion volume was corrected almost perfectly (cf. Fig. 4.7), some very strong artifacts cannot be corrected in the data shown in Fig. 5.6. A significant difference from the results in section 4.2 is that the photon energies in this measurement are very low for a measurement task of an industrial workpiece with metal parts. The remaining artifacts observed here may therefore be caused by factors other than beam hardening, such as photon starvation. However, this could not be changed in the experiments since the maximum voltage and maximum energy threshold of the experimental PCCT device were already used. Another problem may be the poorer spectral separation obtained with the PC detector compared to two subsequent measurements at different tube voltages and with different prefilters, which is also known to negatively affect material decomposition in PCCT [164].

As already known, the reduction of systematic measurement deviations by pseudo-monochromatic imaging has a negative effect on the signal-to-noise-ratio of the corrected volume dataset. The next chapter therefore deals with a procedure that counteracts the reduction of the SNR for artifact-reduced DECT combination volumes.

6 Novel Method for the Reduction of Statistical Measurement Deviations in X-Ray Computed Tomography by Guided Bilateral Filtering

As shown in the previous chapters, the reduction of systematic measurement deviations with the proposed methods may be accompanied by a reduction of the signal- and contrast-to-noise ratios in the corrected CT volume data and thus an increase in statistical deviations. In particular, the DECT data fusion proposed in chapters 4 and 5 using pseudo-monochromatic imaging to reduce beam hardening and scatter artifacts leads to an undesirable noise increase in the fusion volume due to that method (cf. Eq. (2.57)). The frequency split technique for improving the spatial resolution of the fusion dataset as proposed in chapter 4 additionally transfers noise that is present in the high frequencies of the high-resolution volume to the fusion volume. Furthermore, software-based post-processing scatter corrections lead to increased image noise (cf. Ch. 3), since unlike the mean scatter signals, the scatter induced noise cannot be removed from the data once measured.

This chapter describes a method to counteract the degraded CNR by the correction methods mentioned above and thus to reduce statistical measurement errors. To solve this problem, the use of a guided bilateral filter (gBF) is proposed here. The function principle of such a guided bilateral filter is described in the following section.

6.1 Material and Methods

6.1.1 Principle of Guided Bilateral Filtering

The guided bilateral filter proposed here is based on the same principle as an usual bilateral filter (BF) (cf. Eq. (6.1)). Such a bilateral filter corresponds to a low-pass filter,

but it consists of two filter kernels and can be used for edge-preserving noise reduction. One of the filter kernels, the so-called domain kernel D, weights the contribution of individual voxels to the filtering result depending on the respective spatial distance to the target voxel and therefore acts like a low-pass filter in the proper sense. The other filter kernel, the so-called range kernel R_1, on the other hand, acts in intensity domain, i.e. on the gray values of the volume, and suppresses the contribution of individual voxels to the filter result in case of large differences in the gray values. This way the range kernel ensures the edge-preserving properties of the bilateral filter.

$$\begin{aligned} f_{\mathrm{BF}}(\boldsymbol{r}) &= \frac{1}{W(\boldsymbol{r})} \sum_{\boldsymbol{\rho}} f_{\alpha_1}(\boldsymbol{\rho})\, R_1(|f_{\alpha_1}(\boldsymbol{\rho}) - f_{\alpha_1}(\boldsymbol{r})|)\, D(|\boldsymbol{\rho} - \boldsymbol{r}|) \\ W(\boldsymbol{r}) &= \sum_{\boldsymbol{\rho}} R_1(|f_{\alpha_1}(\boldsymbol{\rho}) - f_{\alpha_1}(\boldsymbol{r})|)\, D(|\boldsymbol{\rho} - \boldsymbol{r}|) \end{aligned} \tag{6.1}$$

The volume to be filtered is denoted $f_{\alpha_1}(\boldsymbol{\rho})$ in the above equation. The reason for this notation is that in the following the bilateral filter and guided bilateral filter are applied to volumes obtained by alpha blending (cf. Eq. (2.56)).

It is straightforward to understand that the possibilities of using the bilateral filter as an edge-preserving low-pass filter are limited by the CNR of the considered initial volume: the bilateral filter can only effectively suppress noise if the range kernel allows filtering of the peaks of the noise signals. On the other hand, the range kernel must not allow filtering of material transitions. A sufficient distinction between noise peaks and edges is therefore only given for data with relatively high CNR, i.e. relatively low noise peaks with simultaneously relatively high contrast levels.

Volume data, as they result from pseudo-monochromatic volume combinations, show a reduced amount of systematic deviations, caused for example by beam hardening and scattered radiation, but have a deficit regarding their CNR. Therefore, the application of a bilateral filter to such a dataset alone would not provide large improvements with respect to the reduction of statistical, noise-induced measurement deviations at constant structural resolution. Because of this, the use of a guided bilateral filter, defined in the following equation, is proposed here for the correction of such volume data:

$$\begin{aligned} f_{\mathrm{gBF}}(\boldsymbol{r}) &= \frac{1}{W(\boldsymbol{r})} \sum_{\boldsymbol{\rho}} f_{\alpha_1}(\boldsymbol{\rho})\, R_1(|f_{\alpha_1}(\boldsymbol{\rho}) - f_{\alpha_1}(\boldsymbol{r})|)\, R_2(|f_{\alpha_2}(\boldsymbol{\rho}) - f_{\alpha_2}(\boldsymbol{r})|)\, D(|\boldsymbol{\rho} - \boldsymbol{r}|) \\ W(\boldsymbol{r}) &= \sum_{\boldsymbol{\rho}} R_1(|f_{\alpha_1}(\boldsymbol{\rho}) - f_{\alpha_1}(\boldsymbol{r})|)\, R_2(|f_{\alpha_2}(\boldsymbol{\rho}) - f_{\alpha_2}(\boldsymbol{r})|)\, D(|\boldsymbol{\rho} - \boldsymbol{r}|) \end{aligned} \tag{6.2}$$

Compared to the unguided bilateral filter in equation (6.1), it is noticeable that the guided bilateral filter in the above equation includes an additional range kernel R_2 that acts on a different volume data set, called the guiding volume $f_{\alpha_2}(\boldsymbol{\rho})$. The idea of the guided bilateral filter is that the constraint on low-pass filtering at edges or material transitions by the range kernel is mainly determined based on the guiding volume. For this purpose, the guiding volume dataset must be aligned with the dataset to be filtered

and must represent the same measurement object with the same or increased spatial resolution and an increased CNR for the method to be advantageous. Therefore, a CNR optimizing DECT combination of the spectral data is suitable for a guiding volume dataset (cf. Eq. (2.59)). Because such a DECT combination is generated by the same principle as the pseudo-monochromatic volume $f_{\alpha_1}(\boldsymbol{\rho})$ only with a different linear factor, $f_{\alpha_2}(\boldsymbol{\rho})$ is used for the notation of this volume in the guided bilateral filter.

The form of the low-pass filtering performed in Eqs. (6.1) and (6.2) is not fixed for this method. For the results shown in section 6.2, isotropic Gaussian filter kernels were used in each case. Thus, the exact expression of the range and domain kernels of the bilateral filter and guided bilateral filter are given by:

$$\begin{aligned} R_1(|f_{\alpha_1}(\boldsymbol{\rho}) - f_{\alpha_1}(\boldsymbol{r})|) &= e^{-\frac{(f_{\alpha_1}(\boldsymbol{\rho}) - f_{\alpha_1}(\boldsymbol{r}))^2}{2\,\sigma_{r,1}^2}} \\ R_2(|f_{\alpha_2}(\boldsymbol{\rho}) - f_{\alpha_2}(\boldsymbol{r})|) &= e^{-\frac{(f_{\alpha_2}(\boldsymbol{\rho}) - f_{\alpha_2}(\boldsymbol{r}))^2}{2\,\sigma_{r,2}^2}} \\ D(|\boldsymbol{\rho} - \boldsymbol{r}|) &= e^{-\frac{(\boldsymbol{\rho} - \boldsymbol{r})^2}{2\,\sigma_d^2}} \end{aligned} \tag{6.3}$$

The normalization terms of the Gaussian filters can be neglected here, since they cancel out when the bilateral filter is normalized via $1/W$. A possible alternative to Gaussian filter kernels, which could reduce the computation time of the filtering process, would be an averaging filter for instance.

The choice of the filter parameters $\sigma_{r,1}$, $\sigma_{r,2}$ and σ_d generally depends on the CNR of the initial or guiding volume and the desired noise reduction. The domain parameter σ_d must be chosen large enough to achieve the desired noise level. For the parameters $\sigma_{r,1}$ for the bilateral filter or $\sigma_{r,2}$ for the guided bilateral filter, the value in each case must allow maximum noise suppression with simultaneous edge preservation. It is important to note that the range kernel R_1, that evaluates gray value differences on the data to be filtered, is still present in the guided bilateral filter in equation (6.2). This is necessary because the CNR optimizing DECT combination $f_{\alpha_2}(\boldsymbol{\rho})$, unlike the pseudo-monochromatic DECT volume with minimal artifacts $f_{\alpha_1}(\boldsymbol{\rho})$, generally has stronger artifacts and thus contains no or defective edge information in areas strongly affected by artifacts. The range kernel R_1 ensures that edges which are unrecognizable in the guiding volume due to artifacts are not smoothed. However, compared to the range kernel R_1 in Eq. (6.1), a lower constraint criterion, i.e., a higher $\sigma_{r,1}$, can be chosen for the same parameter in Eq. (6.2). This is because the parameter is not being used for edge preservation in the complete volume, which is mainly done by the range kernel of the guiding volume R_2, but has to preserve edges only at locations of strong artifacts of the guiding volume. The implied loss of spatial resolution in such artifact-contaminated areas for low-contrast material transitions in the filtered volume must be accepted here.

Figure 6.1 explains the concept of the bilateral filter and the guided bilateral filter exemplarily by filtering two three-dimensionally represented surfaces. Both surfaces were created from a gray-scale image containing attenuation values in which a sharp object edge was represented with different levels of contrast (0.04/mm high CNR, and

0.02/mm low CNR) and different levels of white noise ($\sigma = 0.005$/mm high CNR, and $\sigma = 0.015$/mm low CNR). This surface is filtered in Fig. 6.1 using a Gaussian low-pass filter, two different bilateral filters, and a guided bilateral filter. The size of the domain kernel was $\sigma_d = 5$ px in each case. The two filterings using bilateral filters differed in the size of the range kernel for the low CNR surface. While $\sigma_{r1} = 0.01$/mm was chosen for the first variant, this value was increased to $\sigma_{r1} = 0.045$/mm for the second bilateral filter. It can be seen that when the bilateral filter is used, appreciable edge-preserving noise reduction can be achieved only for the surface with high CNR. Whilst a low choice of σ_{r1} does not help to substantially reduce the noise in the low CNR surface, as can be seen for the first bilateral filtering result, a higher choice of σ_{r1} (bilateral filter 2) does result in noise reduction, but also in smoothing of the edge, similar to the use of a simple Gaussian low-pass filter. Only the use of a guided bilateral filter leads to a significant noise reduction with simultaneous edge preservation for the low CNR surface. When using the guided bilateral filter for the high CNR surface, the surface itself is used as a guide and not the other one with a poor CNR, which is self-explanatory.

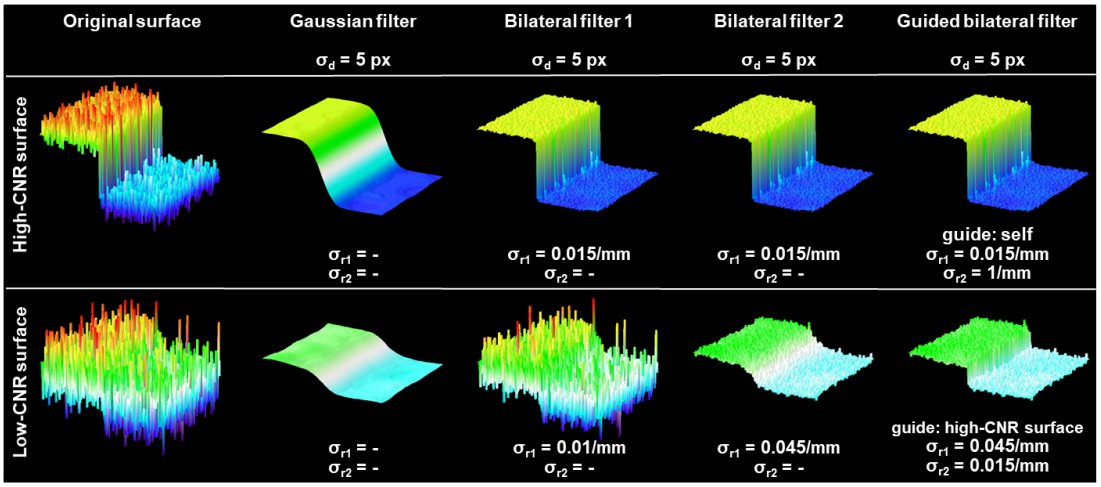

Figure 6.1: Example for the effects of different filters on a surface with a high CNR (top row) and one with a low CNR (bottom row). From left to right the filters used are a Gaussian, bilateral filters with two different σ_{r1} settings for the low CNR surface and a guided bilateral filter.

In summary, the guided bilateral filter represents a possibility to combine the different advantages of two volume datasets regarding artifact content, CNR as well as structural resolution in one volume dataset: The volume resulting from the filtering has a much better CNR at the same artifact content as the artifact-reduced DECT volume. In addition, the edge sharpness of the filtered volume is aligned with that of the guiding volume. Advantages of the edge sharpness of the guiding volume compared to the initial volume can accordingly be transferred to the filtered volume. These traits are shown by the results in the following sections.

6.1.2 Experimental Investigations on Clinical Photon Counting X-Ray Computed Tomography Data

The utilization of a guided bilateral filter for the reduction of statistical measurement deviations was experimentally tested on different datasets and will first be evaluated using spectral data from the Siemens Somatom CounT PCCT. This CT system is already known from chapter 5.

The datasets examined were a head scan from a human postmortem study, which partially shows strong metal artifacts due to dental implants. This postmortem experiment was approved by the local ethics committee (S-021/2020). Furthermore, a pig cadaver with manually inserted hip total endoprostheses (TEPs) was measured. Both datasets were acquired in the UHR mode of the PC detector, just like the workpiece discussed in chapter 5. This mode allows setting two energy thresholds, so two bin images can be generated. A tube voltage of 140 kV was used for both scans and the thresholds of the PC detector were at 20 keV and 90 keV, respectively. The tube current-time product was 300 mAs for both scans. Data were reconstructed using filtered backprojection with a B40f kernel. The voxel sizes of the reconstructed volumes were $dx = dy = 0.54\,\mathrm{mm}$ for each dataset at a slice thickness of $dz = 0.5\,\mathrm{mm}$ for the head dataset and $dz = 0.3\,\mathrm{mm}$ for the pig data. For each of these datasets, a volume with minimum artifact content (cf. Sec. 5.3.3) and one with maximum CNR (cf. Eq. (2.59)) between water-equivalent soft tissue and fat were created by linear blending of the two bin images and the guided bilateral filter was applied as described in the previous section to the volume with minimum artifact content by guidance through the volume with maximum CNR.

As a comparison method for increasing the CNR in the artifact-reduced data, two bilateral filters without guidance were used in each case on the artifact-reduced bin combination, each differing in the magnitude of the range kernel parameter $\sigma_{r,1}$. For one filter, $\sigma_{r,1}$ corresponded to the standard deviation of gray values in soft tissue, i.e., the noise of gray values in that tissue type. For the other filter, $\sigma_{r,1}$ was chosen so that the CNR between soft tissue and fat corresponds to that of the guided bilateral filter. For the guided bilateral filter, $\sigma_{r,2}$ corresponded to the noise of the gray values in soft tissue of the guiding volume and $\sigma_{r,1}$ was chosen depending on the dataset so that no high-contrast material transitions were smoothed. Exact values for the range kernel parameters are given in section 6.2.1. The domain parameter $\sigma_d = 2.16\,\mathrm{mm}$ was the same for all datasets.

6.1.3 Experimental Investigations on Industrial MultiSpek Cone-Beam Computed Tomography Data

To counteract the increased noise level due to the scatter artifact correction via ESC and FSDECT data combination in the MultiSpek CBCT data of the automotive controller workpiece (cf. Fig 4.5), a similar procedure was pursued for this dataset to increase the aluminum-air CNR using a guided bilateral filter.

Because the datasets used here correspond to those in chapter 4, one may refer to sections 4.1.1 and 4.2, respectively, for the acquisition parameters and generation rules

of the FSDECT volume. However, unlike the clinical PCCT datasets, in this case the Micro volume (i.e., $\alpha_2 = 1$) was used as guiding volume instead of a CNR-optimizing volume combination because the Micro volume has a better structural resolution than the Macro volume or a volume generated from both volumes by linear blending after MTF adjustment. The filter parameters of the guided bilateral filtering process for this dataset were $\sigma_{r,1} = 83\,\mathrm{HU}$, $\sigma_{r,2} = 63\,\mathrm{HU}$, and $\sigma_d = 0.3\,\mathrm{mm}$.

In order to evaluate and quantify the corrections applied so far, the workpiece was measured thirteen times at the MultiSpek CT with the same acquisition parameters and the corrections (ESC, FSDECT data fusion, and guided bilateral filter) were applied on each dataset. Then the inner diameter of two drilling holes within the aluminum block of the workpiece were measured. This was done by an automatic segmentation of the drilling hole at three different section planes in the volume and evaluation of the corresponding surface contour via the volume image processing pipeline of the WinWerth® software. Subsequently, a Gaussian best fit cylinder (cf. Sec. 2.1.6) was measured for each drilling hole with the WinWerth® software using the contours at the different section planes and the drilling hole diameters were evaluated. Subsequently, the statistics of the drilling hole diameter measurements were determined for the thirteen repetition measurements. Of particular interest here, in addition to the mean value as well as the standard deviation, is the maximum span of the measured values, the so-called repeatability of that measure. A small value of the repeatability is desirable because this implies small statistical measurement deviations and no strong outliers in the data, e.g. due to systematic errors such as image artifacts, and therefore benchmarks the precision of the measurement. The corresponding volume sections, section plane positions and drilling holes are shown in the results section of this chapter (6.2.2).

6.2 Results

6.2.1 Results for Clinical Photon Counting X-Ray Computed Tomography Data

Figure 6.2 shows for an exemplary axial volume slice the bin images of the two datasets measured at the PCCT, as well as the results of the pseudo-monochromatic volume combination, and the linear blending of the datasets for an optimal soft tissue-fat CNR. It can be seen that in both measurements the high energy bin image already shows a strong reduction of metal artifacts compared to the low energy bin image. Residual metal artifacts can be reduced by pseudo-monochromatic imaging. The CNR maximizing volume, on the other hand, has a very high level of such systematic measurement deviations, as expected. The CNR was determined using ROIs in regions of low artifact levels in the soft and fat tissue of the volume data. A red and yellow circle schematically represent these ROIs in the figure. To reduce the influence of systematic deviations when evaluating image noise in the different ROIs, noise was determined based on the difference of two axial volume slices as it was done in section 4.2. The CNR for the dataset is shown below the respective volume slice, as is the blending factor for the fusion volumes. It can be seen that the CNR between the artifact reducing and the CNR maximizing fusion volumes differs very much. For the head dataset they differ by a factor of about 3 and for the pig dataset even by a factor of about 4.

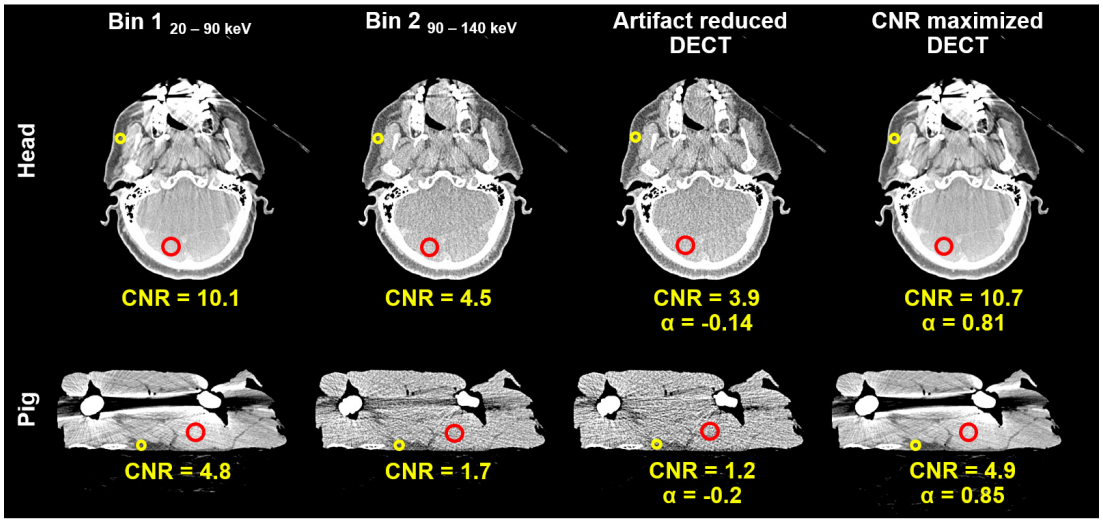

Figure 6.2: Axial volume slices of both PCCT datasets investigated in this chapter (two rows). The first and second column show the two bin images, and columns three and four show DECT data combinations for artifact reduction and CNR optimization, respectively. The red and yellow circles depict ROIs for CNR calculations. CNR and blending factors are given beneath the images. $C = 0\,\mathrm{HU}$, $W = 300\,\mathrm{HU}$.

The results for bilateral and guided bilateral filtering of these datasets are shown in Figs. 6.3 and 6.4. Both of these figures show two distinct axial slices of the volumes, as well as coronal and sagittal reformations of the volume. For the axial slices certain ROIs are shown in detail in order to highlight the advantages of guided bilateral filtering.

From the first axial slice from Fig. 6.3 it can be concluded that the proposed guided bilateral filter (gBF) that uses the CNR-maximizing volume as guiding volume is able to significantly reduce image noise without reintroducing artifacts from the CNR-maximized volume, e.g. by blurring along the streaking artifact caused by the metallic dental implants. A critical region where this could occur is highlighted by a red arrow in the ROI of that specific CT image. This observation is also confirmed by the coronal and sagittal volume slices. Whilst the artifact-reduced bin combination that is filtered with a bilateral filter with a small range parameter of $\sigma_{r,1} = 25\,\mathrm{HU}$ (BF 1) only shows a limited noise reduction, the same volume filtered with a bilateral filter with a large range parameter $\sigma_{r,1} = 55\,\mathrm{HU}$ (BF 2) does feature a significant decrease of the noise level. However, structural details are lost by this filtering process, as can be seen at the structures highlighted with red arrows in the ROI of the second axial slice. Furthermore, transitions of soft tissue and fat tissue appear rugged and unrealistic in these images. This is due to the high image noise in the artifact reduced bin combination volume. Only if the artifact-reduced bin combination is smoothed with the guided bilateral filter ($\sigma_{r,1} = 100\,\mathrm{HU}$, $\sigma_{r,2} = 10\,\mathrm{HU}$) the resulting volume yields low noise levels at a high spatial resolution with a low artifact content.

Similar observations as for the head data can be made for the pig dataset. In this measurement, the hip TEPs lead to stronger metal artifacts than the dental implants from the human corpse. Furthermore, the CNR of the volumes is lower than in the previous case. Nevertheless, the axial slices and the corresponding ROIs in Fig. 6.4 show that using a guided bilateral filter ($\sigma_{r,1} = 200\,\mathrm{HU}$, $\sigma_{r,2} = 20\,\mathrm{HU}$) leads to the best image quality in terms of CNR, amount of metal artifacts, and spatial resolution. Findings for the bilateral filters without guide ($\sigma_{r,1} = 45\,\mathrm{HU}$ (BF 1) and $\sigma_{r,1} = 130\,\mathrm{HU}$ (BF 2)) resemble those observed for Fig. 6.3.

In order to quantify these results, the CNR between soft tissue and fat tissue is calculated for each of the volumes shown in Figs. 6.3 and 6.4 and the results are given in table 6.1. The quantitative results show that while the CNR is increased by a factor of roughly five for the head dataset and seven for the pig dataset when using a guided bilateral filter, it can only be increased by a factor of less than two for the unguided bilateral filter that does not smooth structural information (bilateral filter 1). The unguided bilateral filter with stronger range parameter settings (bilateral filter 2) leads to the same CNR improvements as the guided bilateral filter, as it was tuned to do so, but also blurs details, which is shown in the CT images.

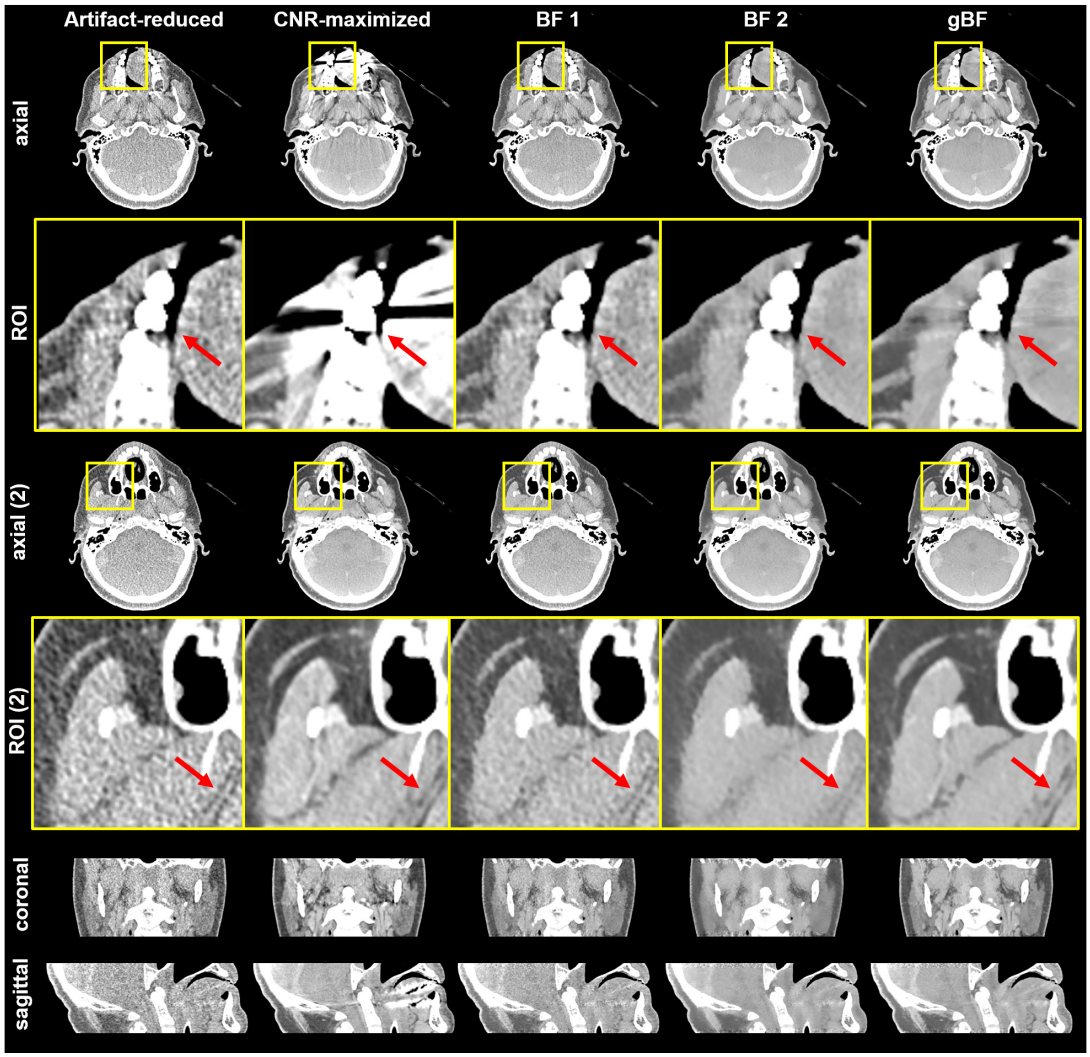

Figure 6.3: Five different CT volumes ($C = 0\,\text{HU}$, $W = 300\,\text{HU}$) of the head CT are shown in five columns: the artifact-reduced pseudo-monochromatic volume (left), the CNR-maximizing DECT volume (middle left), the artifact-reduced pseudo-monochromatic volume filtered with a bilateral filter with a low range parameter (BF 1, middle) and with a high range parameter (BF 2, middle right), and the artifact-reduced pseudo-monochromatic volume filtered with a guided bilateral filter (gBF, right) with the CNR-maximizing DECT volume serving as guiding volume. The different rows show two distinct axial slices and corresponding ROIs of the areas marked by the yellow boxes and coronal as well as sagittal reformations of the volumes. Structures of special interest are marked with red arrows in the different ROIs.

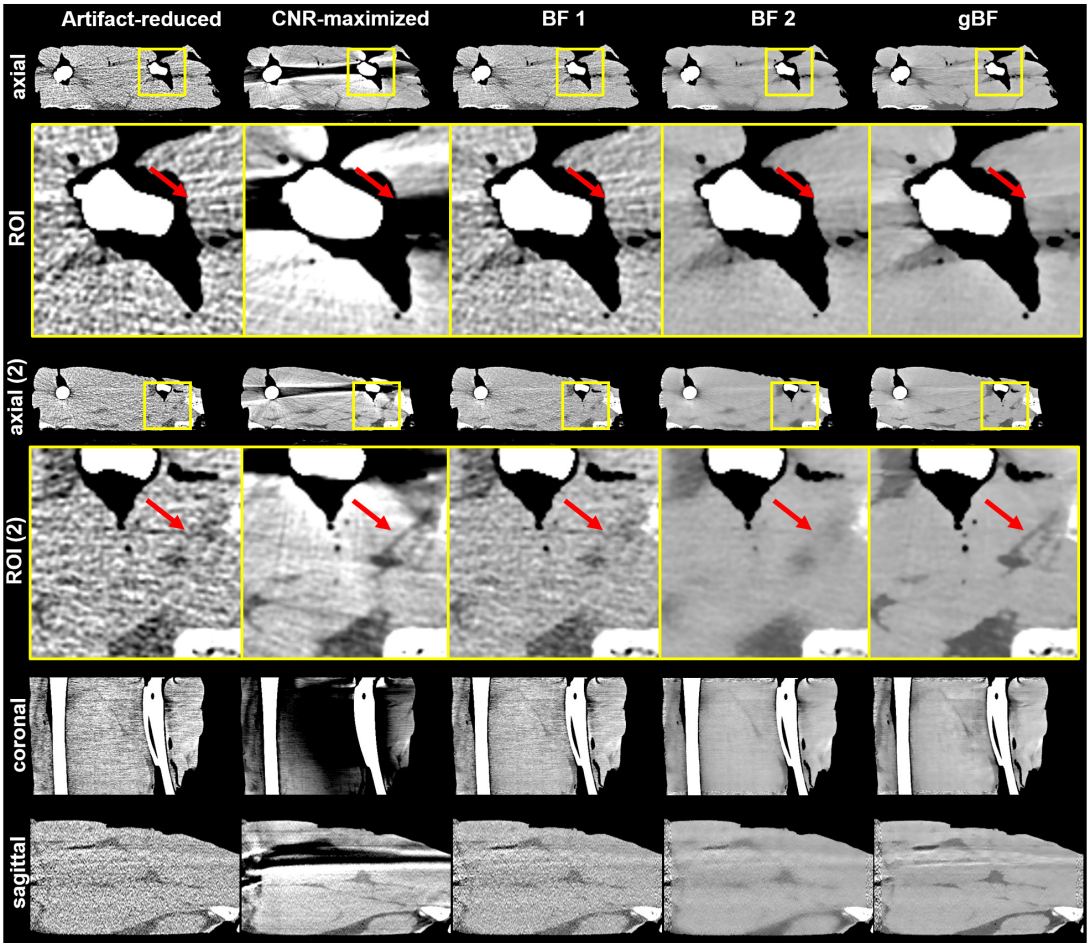

Figure 6.4: In a similar arrangement to Fig. 6.3, the results for the processed pig CT are shown in this figure. $C = 0\,\mathrm{HU}$, $W = 300\,\mathrm{HU}$.

	CNR in head data	CNR in pig data
Low energy bin image	10.1	4.8
High energy bin image	4.5	1.7
Artifact-reduced DECT	3.9	1.2
CNR-maximized DECT	10.7	4.9
Bilateral filter 1	7.6	2.2
Bilateral filter 2	18.3	8.7
Guided bilateral filter	18.3	8.8

Table 6.1: Evaluation of the CNR between soft tissue and fat tissue for the different volumes shown in Figs. 6.3 and 6.4 for the two PCCT datasets.

6.2.2 Results for Industrial MultiSpek Cone-Beam Computed Tomography Data

For the analysis of the automotive controller, which was measured at the MultiSpek CBCT system, the scatter-corrected (ESC) FSDECT data (cf. Fig. 4.5) was specifically chosen for noise reduction with guided bilateral filtering here and further evaluation in the next section because it has a high spatial resolution and contains the lowest amount of systematic measurement deviations due to the applied artifact corrections but also a high amount of statistical deviations, i.e. a high level of noise (cf. table 4.2). Results for applying a guided bilateral filter to this data, using the high-resolution Micro volume as guiding volume, are shown in Fig. 6.5.

It can be observed that by applying the guided bilateral filter the image noise is significantly decreased at constant contrast levels between the different materials, resulting in an increase of the CNR. The close-ups of small structures and edge transitions furthermore show that the structural resolution of the volume remains unaffected and is not smoothed by this filtering process. Evaluating the image noise in the same aluminum region that was used for the analysis in table 4.2, yields a noise level of 28 HU after guided bilateral filtering, which corresponds to a decrease by a factor of roughly 3 compared to the unfiltered data (noise = 79 HU). As the noise reduction in air regions is almost the same, the same factor is found for the improvement of aluminium-air CNR. This can be exploited for measurements at such aluminium-air transitions, which will be discussed in the following.

i.) Measurement of Drilling Holes: Repeatability Study

It was shown that the correction algorithms applied to the Micro and Macro measurements in section 4.2 reduce systematic errors appearing as image artifacts and qualitatively improve the image quality, which may be useful for inspection tasks of such CT volumes. Furthermore, statistical deviations of these data can be reduced and CNRs maximized using a guided bilateral filter, as proposed in this chapter. If a CT measurement is to be used for metrological purposes, it must first be possible to automatically segment geometry elements within the measured CT volume. To what extent the proposed reduction methods of systematic and statistical measurement deviations have an influence on this will now be investigated on the basis of diameter measurements of internal drilling holes in the aluminum block of the automotive controller workpiece.

Figure 6.6 displays the volumes of a Micro and Macro measurement, the resulting FSDECT combination volume, and the FSDECT combination volume with prior scatter correction (ESC) with and without post-processing it with a guided bilateral filter (gBF). For each of the volumes three axial slices are shown, corresponding to the slices at which the drilling hole measurements are taken. Other than the volumes shown in Figs. 6.5 and 4.5, the volumes in Fig. 6.6 were first aligned in the WinWerth® software before evaluating axial slices in order to have circular geometry elements for the drilling holes in each analyzed volume slice. This is why the z-positions are here denoted as z' in contrast to z in Fig. 6.5, for instance. As the images are directly generated with the

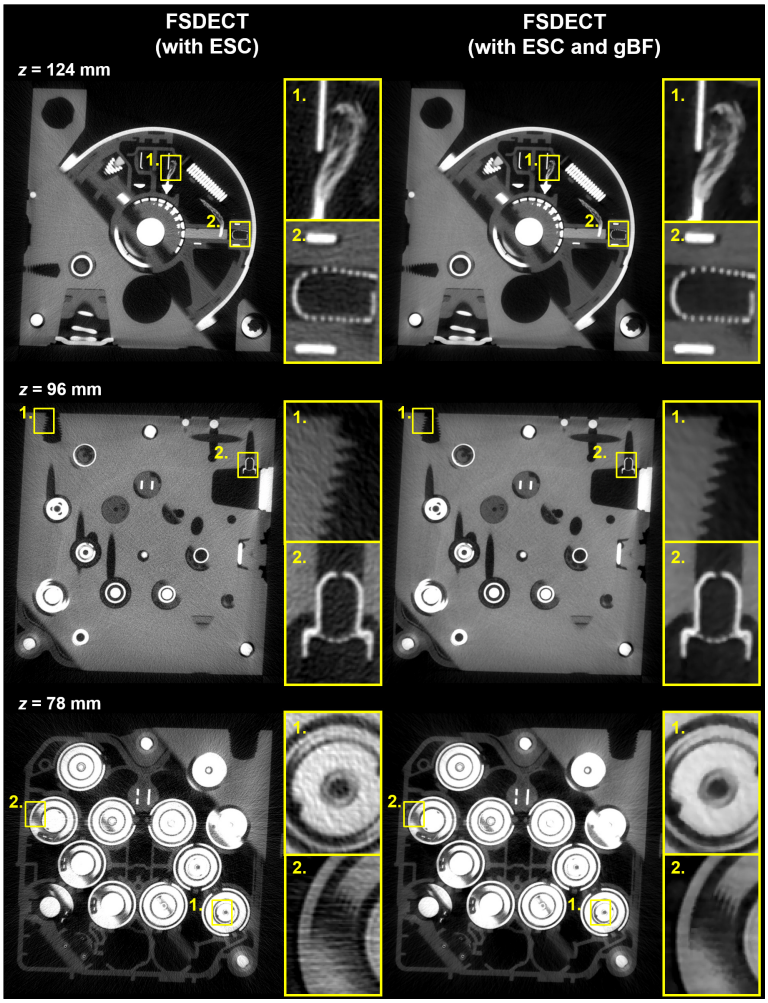

Figure 6.5: Three exemplary axial volume slices ($C = 0\,\mathrm{HU}$, $W = 2000\,\mathrm{HU}$) of the ESC-corrected FSDECT volume of the automotive controller from the MultiSpek-CT measurements (left) and the same data processed with a guided bilateral filter (right). Analogously to Fig. 4.5, two close-ups of certain ROIs marked by yellow boxes are given for each axial slice besides the respective image.

WinWerth® software, the display window in this figure also differs from those known from Figs. 6.5 and 4.5. Instead of a conversion to Hounsfield units (cf. Eq. (2.30)), the software automatically displays the gray values such that the minimal attenuation value of the entire volume is displayed completely black and the maximum one completely white (min./max. window). Even though this displaying style does not allow for a direct quantitative comparison e.g. of the aluminum region, it provides an additional impression of the superior image quality of the processed volume data compared to Micro and Macro volumes regarding the homogeneity of the gray values. The two

drilling holes whose diameters are evaluated in the following are highlighted with yellow boxes in the volume slices and additionally displayed in a separate close-up image. The blue lines in these close-up images show the resulting aluminum surface contour for an automated evaluation with the volume image processing pipeline of the WinWerth® software. Whenever artifacts induce an interruption of that contour, which prevents an automated measurement of a circle geometry element for this contour and therefore precludes an automatic measurement of the drilling hole's diameter, such a position is marked with a red arrow. Contours which are not interrupted and allow an automatic evaluation are marked with green arrows. It can be seen that for the Micro volume not a single contour fulfils the image quality requirements for an automated measurement of the drilling holes. Because the Macro volume contains less artifacts than the Micro volume, three out of six contours are evaluable. By using FSDECT all contours can automatically be evaluated for both drilling holes at each z-Position. However, some remaining artifacts still affect the contour location negatively by predominantly shifting it towards the inside of the drilling hole. When a cylinder is evaluated by a Gaussian fit on such contours, as it was done in the following, this must result in systematic deviations towards smaller diameters. The problem is solved for the FSDECT volume with prior empirical scatter correction. These volumes contain the least amount of systematic deviations due to artifacts and therefore the automated segmentation of the drilling holes no longer poses any particular challenge. By post-processing the FSDECT+ESC volume with a guided bilateral filter the image quality is further improved compared to the unfiltered data by reducing the noise level.

In Fig. 6.7 the results for the drilling hole diameter evaluations are plotted for the thirteen measurements of the automotive controller. The plot on the top left shows an evaluation of the FSDECT volume data. Obviously image artifacts are insufficiently corrected for this data because two outliers severely distort the results for the left drilling hole. The measures for the data that are scatter-corrected with the empirical scatter correction prior to the FSDECT fusion (FSDECT+ESC), as well as those for these volumes that are post-processed by a guided bilateral filter (FSDECT+ESC+gBF), do not show such outliers (cf. top right and bottom left plot in Fig. 6.7). A boxplot for the data points is shown in the lower right plot in Fig. 6.7. For this plot the two outlier data points of the FSDECT data were neglected. This plot emphasizes the differences of the evaluation results: The FSDECT data without scatter correction and noise reduction yield much smaller results for the drilling hole diameters with a median value of 11.07 mm for the left hole and 11.206 mm for the right hole than the data with scatter correction which yield 11.409 mm for the left, and 11.412 mm for the right hole, respectively, and the data with scatter correction and guided bilateral filtering which give 11.412 mm and 11.422 mm (cf. table 6.2). Also the range of the measures is evidently much larger. Comparing FSDECT+ESC volumes with and without guided bilateral filtering a slight trend towards larger diameters and a smaller range of the data can be observed for the case when filtering is performed. These effects are rather small ($\mathcal{O}(1\,\mu m)$), however. All analyses show a positive offset for the drilling hole diameter of the right drilling hole compared to the left. This offset is most pronounced for the FSDECT data. Table 6.2 shows characteristics of the statistical analysis for

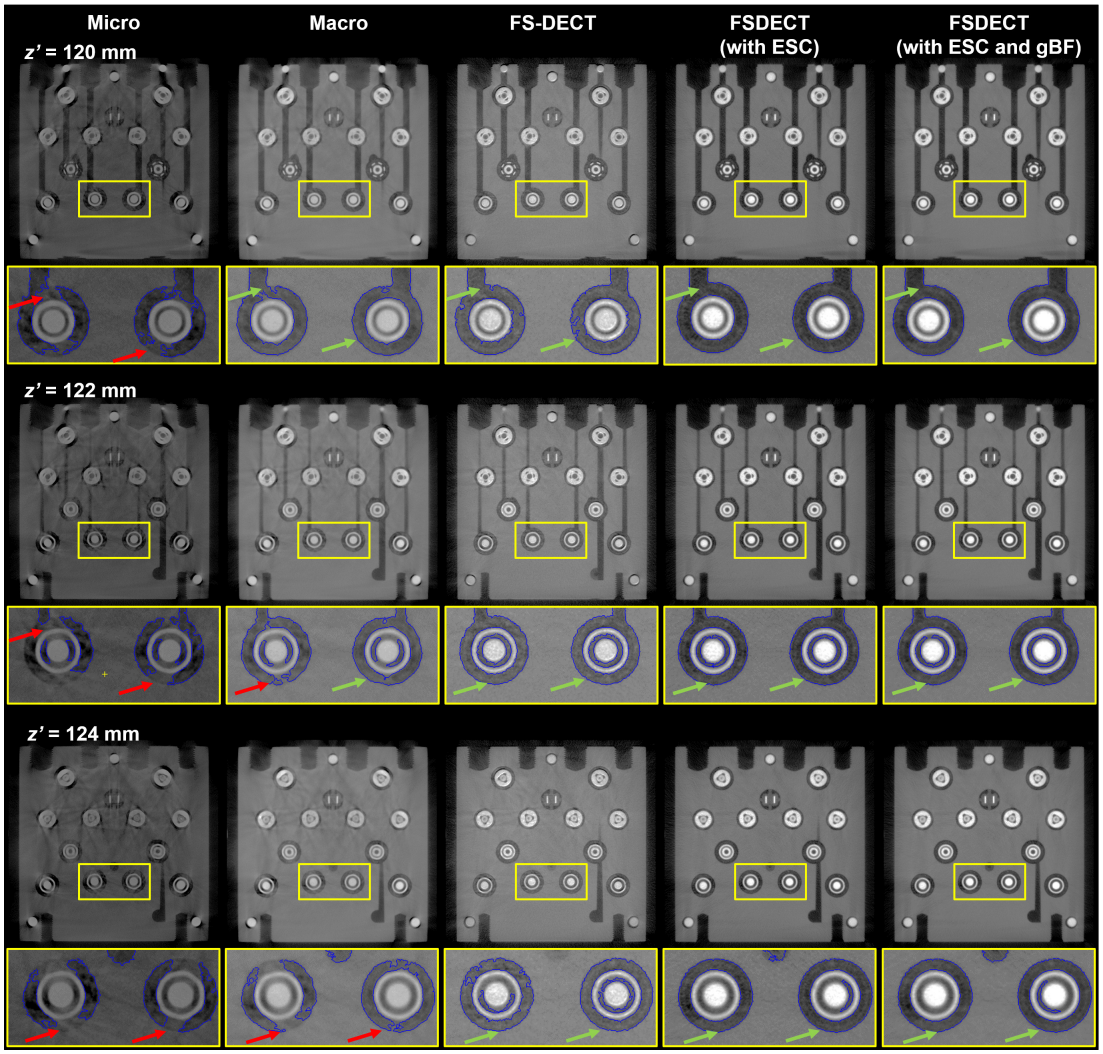

Figure 6.6: CT volumes of the automotive controller workpiece measured at the MultiSpek CBCT system. From left to right the Micro, Macro, FSDECT, FSDECT with prior ESC, and FSDECT with prior ESC and subsequent guided bilateral filtering volumes are displayed. Three axial slices are shown for each dataset and close-ups show ROIs of the evaluated drilling holes marked with yellow boxes in the overview CT image. The blue lines in these ROIs depict automatically generated surface contours. Red arrows are used to indicate disruptions in those contours and green arrows point out that the contours are continuous and thus automatically evaluable. The display window corresponds to a min./max. window.

all datasets without any removal of outliers. The observations that could be made through the plots are confirmed. For the FSDECT data, the sample mean and standard

deviation for the diameter of the left drilling hole is (11.078 ± 0.284) mm and that of the right drilling hole is (11.212 ± 0.030) mm. The repeatability is 912 µm for the left hole and 99 µm for the right hole. A drastic improvement of the repeatability can be obtained, when ESC is performed prior to the FSDECT fusion. Then the repeatability amounts to only 21 µm for the left hole and 19 µm for the right hole at a diameter of (11.408 ± 0.006) mm (left) and (11.414 ± 0.006) mm (right), respectively. If a guided bilateral filter is additionally used, similar drilling hole diameters are measured (11.411 ± 0.006) mm (left) and (11.419 ± 0.005) mm (right) with slightly reduced variances and with a small improvement of the repeatability at now 21 µm (left) and 15 µm (right).

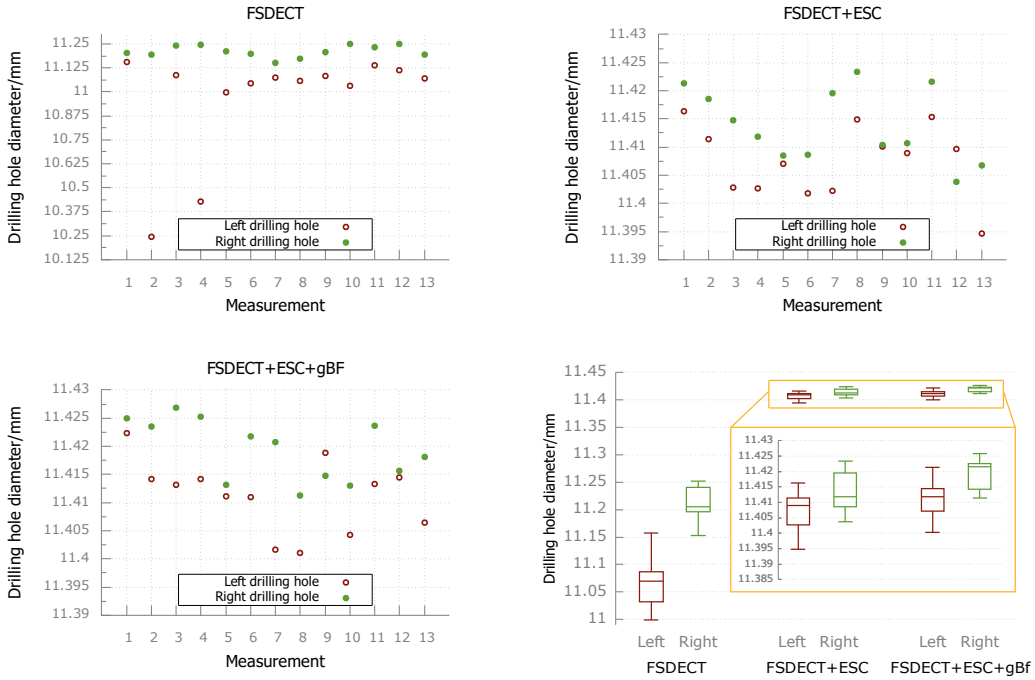

Figure 6.7: The two upper plots and the plot at the bottom left show the measured diameters of the two drilling holes (cf. Fig. 6.6) for the thirteen repeatability study measurements, with data for FSDECT volumes shown in the top left, data for FSDECT with ESC (FSDECT+ESC) shown to the right, and data for FSDECT with ESC and guided bilateral filter (FSDECT+ESC+gBF) shown at the bottom left. The bottom right plot shows the statistics for each dataset as a boxplot. A rescaling of the y-axis shows the FSDECT+ESC and FSDECT+ESC+gBF boxplots in more detail within the orange box that is depicted in this figure.

FSDECT	left hole diameter	right hole diameter
mean	11.078 mm	11.212 mm
standard deviation	0.284 mm	0.030 mm
median	11.070 mm	11.206 mm
minimum	10.245 mm	11.153 mm
maximum	11.157 mm	11.252 mm
repeatability (max-min)	0.912 mm	0.099 mm

FSDECT+ESC	left hole diameter	right hole diameter
mean	11.408 mm	11.414 mm
standard deviation	0.006 mm	0.006 mm
median	11.409 mm	11.412 mm
minimum	11.395 mm	11.404 mm
maximum	11.416 mm	11.423 mm
repeatability (max-min)	0.021 mm	0.019 mm

FSDECT+ESC+gBF	left hole diameter	right hole diameter
mean	11.411 mm	11.419 mm
standard deviation	0.006 mm	0.005 mm
median	11.412 mm	11.422 mm
minimum	11.400 mm	11.411 mm
maximum	11.421 mm	11.426 mm
repeatability (max-min)	0.021 mm	0.015 mm

Table 6.2: Statistical characteristics of the data from the repeatability study from Fig. 6.7.

6.3 Discussion

The results show that a guided bilateral filter is an effective method to counteract the noise increase observed in artifact reduction algorithms that are based on spectral volume combinations. For the datasets analyzed here, the guided bilateral filter leads to a CNR improvement of up to a factor of seven.

Regardless if the spectral data are acquired in a PCCT setup or by sequential scans with different spectra, such as in the MultiSpek CBCT measurements, the method can be used to reduce the impact of noise while edges and the low amount of systematic measurement deviations, e.g. beam hardening and scatter artifacts, are conserved. Due to a lower level of noise or a higher structural resolution, a guiding volume may also be richer in small structural details than the noisy data. This advantage is transferred to the volume processed with the proposed filter algorithm, as well (cf. Fig. 6.3).

Besides the image quality improvements, the reduction of statistical measurement deviations with a guided bilateral filter also influences the evaluation of measurements, as it was shown for the analysis of the drilling hole diameters of the automotive controller. Neither the Micro, nor the Macro measurements can themselves be used to take these measures due to severe artifacts. Using the FSDECT combination proposed in chapter 4, the drilling hole diameters can be analyzed. Nevertheless, some artifacts are still remaining in this volume and lead to a distortion of the contour location compared to the real material transition position. The artifacts can be almost completely corrected by performing ESC before FSDECT data fusion. The guided bilateral filter can be used to improve the CNR and therefore reduce the statistical deviations, which are relatively high for this volume. It can be seen in Fig. 6.6 that the remaining artifacts in the FSDECT volume predominantly move the contour location to the interior. This systematic deviation must then lead to smaller measures for the diameter of the drilling hole, which is also observed when comparing the resulting drilling hole diameters of the FSDECT volumes to those of the FSDECT+ESC(+gBF) volumes. One could reduce such measurement errors by post-processing the contour with special filters. This is not done here, though, as the primary goal of this work is to optimize the quality of the CT volume such that it can be analyzed automatically without the necessity to optimize the automatic segmentations in the aftermath. The difference in the drilling hole diameters for the left and right drilling hole, which can mainly be observed in the FSDECT data, is probably due to the same effect that the remaining artifacts cause. It can be seen in Fig. 6.6 that the artifacts are more pronounced at the left drilling hole than at the right one. This could be due to less favorable transmission lengths or line integrals in this region. Even though the difference in drilling hole diameters is much smaller for the scatter-corrected FSDECT data with or without guided bilateral filtering, it is still present. However, a statement about an actual difference of the drilling hole diameters cannot be made on this basis. Indeed, the difference of the mean values of both boreholes is only 6 µm (FSDECT+ESC) and 8 µm (FSDECT+ESC+gBF). Compared to the voxel size of 100 µm, this difference is less than one tenth of the voxel size, which is at the resolution limit even for accurate subvoxel evaluation algorithms. It could also be that possibly not all systematic measurement deviations have been

reduced to a sufficient extent. Some CT artifacts (off-focal radiation, detector afterglow, etc.) remained uncorrected in this measurement. Of course, an incomplete correction of the already targeted artifacts cannot fully be excluded, since both the ESC for scatter artifact reduction and the FSDECT combination for the reduction of beam hardening artifacts are only approximate solutions and do not reproduce the exact physical effects realistically. As expected, applying a guided bilateral filter to the data results in improvements regarding the repeatability and the variance of the measured diameters, at least partially. However, the effects are not particularly strong for the right drilling hole and barely measureable for the left drilling hole. The reason for this is that the area of the drilling holes is severely deteriorated by artifacts in the Micro volume, which acts as the guiding volume here. This leads to drastically reduced contrasts in this area. Therefore, the guided bilateral filter only benefits marginally from the guiding volume in this region. Such a situation corresponds to a limitation of the here proposed method. As the amount of artifacts in the guiding volume is lower for the right drilling hole, small improvements of the measurements performed there are observed, nevertheless. Interestingly, the drilling hole diameters are slightly larger on average when using a guided bilateral filter, which indicates another reduction of systematic deviations towards smaller diameters that were already observed for the FSDECT volume. This happens most likely due to averaging effects in these remaining problematic areas and is not an unwanted effect from low-pass filtering these areas. If one would naively apply a simple low-pass filter to the data, this would result in a systematic deviation towards smaller diameters instead of larger diameters as observed with the guided bilateral filter here. Again, it must be said that these effects are small compared to the voxel size.

Another limitation of the guided bilateral filter, similar to the one discussed above, is that edges which are not clearly outlined in neither the source volume nor the guiding volume cannot be preserved. This implies that for instance noisy low contrast structures in the source volume, which are not detectable in the guiding volume, e.g. due to strong artifacts, may be blurred by the filtering process.

Nevertheless, with the proposed correction from chapters 3, 4, and the guided bilateral filter previously inaccessible measures such as the diameters of the inner drilling holes of the automotive controller can now be measured precisely with a repeatability of $\leq 21\,\mu\text{m}$.

At this point it should be mentioned that this method is not limited to CNR optimization in pseudo-monochromatic images, however. In principle any CT volume with high levels of image noise may be improved if a guiding volume with a favorable CNR is available. Therefore, the proposed method could for example be used to directly denoise the high energy bin image in a PCCT measurement or a CT volume that was measured using strong prefiltration, given another dataset with higher CNR can be used as guiding volume, e.g. the low energy bin image, another volume measured without strong prefiltration or a CNR optimizing combination of this spectral data as it was proposed here. Analogously, PCCT data, which were corrected for metal artifacts with a more specialized algorithm, such as the photon-counting normalized metal artifact reduction (PCNMAR) [20], may be denoised with the method proposed

here. Alternatively, the guided bilateral filter can be used to reduce statistical deviations caused by a post-processing software-based scatter artifact correction method, such as ESC. In this case, the non-scatter corrected volume dataset could be used as the guide volume for the filter applied to the scatter corrected dataset to reduce its noise level. When using the guided bilateral filter in this way, however, special attention must be paid to the choice of the range kernel parameters, since the non-scatter corrected volume may well have a worse CNR in critical regions than the scatter corrected volume.

In addition, attention should be drawn here to the other advantages of PCCT for the application of the guided bilateral filter: many photon-counting detectors allow setting more than just two energy thresholds. This makes more spectral bin images available. This can be used in addition to noise reduction, as the CNR of the guiding volume can be further increased by the additional spectral information [170].

7 | Summary and Conclusions

This dissertation demonstrates different methods for the reduction of systematic measurement deviations in CT measurements. The increase of statistical measurement deviations caused by these methods can in turn be reduced in a spatial resolution-preserving way by another developed method. Although the focus of this dissertation is on industrial CT, i.e. CT for coordinate metrology or inspection of workpieces, most of the methods developed can also be applied to medical CT applications, as has been shown in many cases.

The empirical scatter correction shown in chapter 3 represents a method to reduce scatter induced systematic measurement deviations without requiring specific prior knowledge about the CT device, the measurement parameters or the investigated object. Although the idea of an empirical scatter correction is not new per se, the approach chosen here to correct the projection data physically correctly in intensity domain and to determine the correction quality in the reconstructed volume corresponds to a novelty that provides better correction quality compared to a reference empirical scatter correction method that performs the correction purely in image domain. Comparisons to physically exact methods, such as Monte Carlo simulations, show that corrections by means of ESC yield only slightly worse results when prior knowledge is available and significantly better results when the prior knowledge used for the Monte Carlo simulation is faulty or incomplete. ESC is particularly advantageous in industrial CT, since for separate manufacturing and quality assurance processes, workpiece-specific information, such as the exact material properties, are not necessarily readily available for the correction of the CT measurement. Therefore, especially for measurement service providers, ESC is a useful tool for CT scatter corrections.

Particularly noteworthy is a method developed in the context of this dissertation that allows volume data to be fused from a CT device that has two x-ray tubes of different designs. The volume data combined using the FSDECT algorithm presented in chapter 4 show less systematic measurement deviations than both initial volume datasets while the spatial resolution of the FSDECT volume matches that of the initial volume dataset with better spatial resolution. While frequency split techniques are already known and used in CT imaging, for example to improve the CNR of virtual monoenergetic volume datasets [171], the combination of several advantages of datasets acquired with different types of x-ray tubes, namely the better spatial resolution or the lower amount of systematic measurement deviations, using an artifact-reducing combination of spectral data and a subsequent frequency split, has been successfully

demonstrated for the first time in this work. In principle, the method developed here can also be extended to dual source MSCT systems with two identical x-ray tubes and two x-ray detectors with different spatial resolution properties or dual energy CT measurements where the spatial resolution of the spectral datasets differ due to different scan parameters.

In chapter 5 it was shown that spectral data acquired by photon counting detectors are also suitable for reducing systematic measurement deviations using pseudo-monochromatic imaging. Accordingly, the spectral separation of the data is sufficiently good to be able to reduce image artifacts. In addition, it was shown that energy thresholds on energy-selective detectors are suitable for reducing beam hardening artifacts. Simulations suggest that for measurements with an energy-selective detector, where an energy threshold is used to harden the detected spectrum, an advantage over measurements with energy integrating detector and physical prefiltering can be expected with respect to the SNR. This advantage is particularly pronounced for very hard spectra, i.e., high energy thresholds or strong prefilters. Accordingly, an improved SNR of FSDECT fusion data can be expected when photon-counting flat detectors are used instead of the energy integrating flat detectors used in the CBCT system from chapter 4. This SNR improvement for hardened spectra could be a key advantage of photon counting detectors over energy integrating detectors, especially in industrial inline CT measurements, where there are strict requirements for low measurement times and the increased SNR of the proposed method can be traded off for measurement time reduction. Experimental validations of the simulation results for photon-counting flat detectors in terms of measurement time reduction and spatial resolution of the data compared to energy-integrating flat detectors are subject of future investigations.

Both a scatter correction by means of ESC and the FSDECT data fusion methodically may lead to an unintentional increase of statistical measurement deviations. The guided bilateral filter presented in chapter 6 counteracts this disadvantage. With this filter, information from CT datasets with different properties, i.e. a low degree of systematic measurement deviations with a simultaneously high degree of statistical measurement deviations and vice versa, are combined to generate a volume dataset with fused optimal properties. Even though the guided bilateral filter has long been known in image processing [172], [173], this work is the first to exploit the potential of this filter with different combinations of spectral CT data to obtain artifact-reduced, low-noise CT volumes. The CNR in clinically relevant metal artifact-reduced PCCT data could be increased by a factor of up to 7.3 using this method.

With the correction methods developed in this dissertation, uncooperative workpieces such as the automotive controller that could previously not or not fully be evaluated by CT become accessible for CT measurements and associated dimensional inspection and flaw detection. The repeatability for drilling hole measurements on this workpiece could be reduced to $\leq 21\,\mu m$ without the use of contour filters for thirteen CT measurements at the MultiSpek CBCT system. Although ultimately the problem of scatter, beam hardening, or noise artifacts cannot be considered solved with this work, this dissertation expands the broad field of artifact correction methods in CT and provides useful contributions through the presented methods.

8 Appendix

8.1 Supplements to Chapter 5

8.1.1 Signal-to-Noise-Ratio for Energy-Integrating Detectors

It can be shown that if x-ray pulses are integrated rather than counted, as it is the case for EI detectors, the SNR yields [165]:

$$\mathrm{SNR}_{\mathrm{EI}} = \sqrt{N_0\, A_{\mathrm{Q,EI}}\, \frac{M_1^2}{M_0\, M_2}} = \sqrt{N_0\, A_{\mathrm{Q,EI}}\, S}\,. \tag{8.1}$$

In this equation, M_n describes the n-th momentum of the absorbed energy distribution and S corresponds to the Swank factor that was introduced in Eq. (5.5). When assuming a normalized spectrum $w(E)$, this equation can be formulated as

$$\mathrm{SNR}_{\mathrm{EI}} = \sqrt{N_0\, A_{\mathrm{Q,EI}}\, \frac{(\int \epsilon(E)\, w(E)\, dE)^2}{\int w(E)\, dE\, \int \epsilon(E)^2\, w(E)\, dE}} = \sqrt{N_0\, A_{\mathrm{Q,EI}}}\, \frac{\int E\, w(E)\, dE}{\sqrt{\int E^2\, w(E)\, dE}}\,. \tag{8.2}$$

The function $\epsilon(E)$ corresponds to the energy weighting function defined in Eq. (2.16), which is $\epsilon(E) = E$ for EI detectors. Using the Cauchy-Schwarz inequality, it can easily be shown with the substitution $f(E) = \sqrt{w(E)}\,\epsilon(E)$ and $g(E) = \sqrt{w(E)}$ that the Swank factor S is smaller than one for energy-integrating detectors:

$$\begin{aligned} & \left| \int f(E) \cdot g(E)\, dE \right|^2 \leq \left(\int |f(E)|^2\, dE \right) \cdot \left(\int |g(x)|^2\, dE \right) \\ \Leftrightarrow \quad & \left(\int \epsilon(E)\, w(E)\, dE \right)^2 \leq \left(\int \epsilon(E)^2\, w(E)\, dE \right) \cdot \left(\int w(E)\, dE \right) \end{aligned} \tag{8.3}$$

Therefore, the Swank factor indicates a reduced SNR for EI detectors ($\epsilon(E) = E$) compared to PC detectors ($\epsilon(E) = 1$) for the same effective spectra and quantum efficiencies.

8.1.2 Simulated Detector Responses

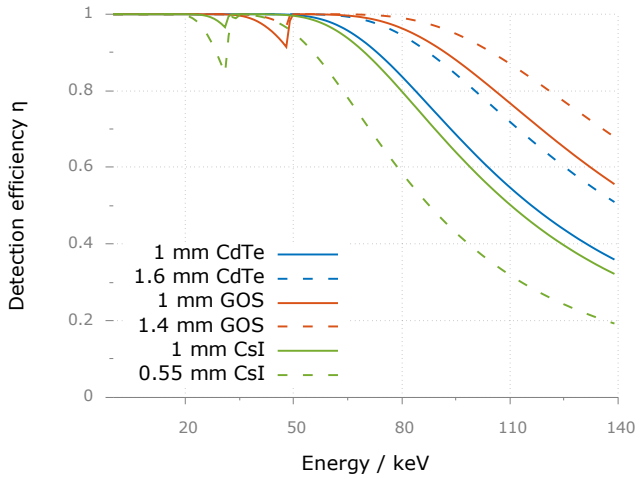

Figure 8.1: This figure shows the detection efficiency $\eta(E)$ for two scintillator materials used in EI detectors (CsI and GOS) and CdTe semiconductors. The detection efficiency was calculated with Eq. 2.14 using data from [95]. The solid lines correspond to detection efficiencies for 1 mm of the respective material and the dashed lines correspond to detection efficiencies for material thicknesses, which are typically used in respective detectors (cf. Sec. 5.2).

Bibliography

[1] W. C. Röntgen, "Über eine neue Art von Strahlen," *Annalen der Physik*, volume 300, number 1, pages 12–17, 1898.

[2] J. Radon, "Über die Bestimmung von Funktionen durch ihre Integralwerte längs gewisser Mannigfaltigkeiten," *Berichte über die Verhandlungen der Königlich-Sächsische Akademie der Wissenschaften zu Leipzig*, volume 69, pages 262–277, 1917.

[3] OECD. "Computed Tomography (CT) Exams." (2018), [Online]. Available: `https://www.oecd-ilibrary.org/content/data/3c994537-en` (visited on 01/31/2022).

[4] J. W. Kress and L. A. Feldkamp, "X-Ray Tomography Applied to NDE of Ceramics," in *Turbo Expo: Power for Land, Sea, and Air*, American Society of Mechanical Engineers, volume 79559, 1983, V005T11A003.

[5] W. B. Gilboy, "X- and γ-ray Tomography in NDE Applications," *Nuclear Instruments and Methods in Physics Research*, volume 221, number 1, pages 193–200, 1984.

[6] L. De Chiffre, S. Carmignato, J.-P. Kruth, R. Schmitt, and A. Weckenmann, "Industrial Applications of Computed Tomography," *CIRP annals*, volume 63, number 2, pages 655–677, 2014.

[7] J. A. Seibert, "Flat–Panel Detectors: How Much Better Are They?" *Pediatric radiology*, volume 36, number 2, pages 173–181, 2006.

[8] L. A. Feldkamp, L. C. Davis, and J. W. Kress, "Practical Cone–Beam Algorithm," *Journal of the Optical Society of America A*, volume 1, number 6, pages 612–619, 1984.

[9] I. Schmidt, "Vollständig und zerstörungsfrei: Zehn Jahre Computertomografie in der Koordinatenmesstechnik," *Quality Engineering*, volume 1, pages 22–15, 2015.

[10] R. Christoph and H. J. Neumann, *Röntgentomografie in der industriellen Messtechnik*. Verlag moderne Industrie, 2011.

[11] S. Moser. "Computertomographie steht noch am Anfang." (2017), [Online]. Available: `https://www.produktion.de/technik/computertomographie-steht-noch-am-anfang-201.html` (visited on 01/31/2022).

[12] J. J. Lifton, A. A. Malcolm, and J. W. McBride, "An Initial Experimental Study on the Influence of Beam hardening in X–Ray CT for Dimensional Metrology," in *5th International Conference on Industrial Computed Tomography-iCT*, 2014.

[13] J. J. Lifton, A. A. Malcolm, and J. W. McBride, "A Simulation–Based Study on the Influence of Beam Hardening in X–ray Computed Tomography for Dimensional Metrology," *Journal of X-ray Science and Technology*, volume 23, number 1, pages 65–82, 2015.

[14] J. Lifton, A. Malcolm, and J. McBride, "An Experimental Study on the Influence of Scatter and Beam Hardening in X–Ray CT for Dimensional Metrology," *Measurement Science and Technology*, volume 27, number 1, page 015 007, 2015.

[15] M. Kachelrieß, *Kapitel 8: Computertomographie. In W. Schlegel, O. Jaekel, and C. Karger: Medizinische Physik*. Springer, 2018.

[16] T. M. Buzug, *Computed Tomography: From Photon Statistics to Modern Cone–Beam CT*. Springer, 2008.

[17] J. F. Barrett and N. Keat, "Artifacts in CT: Recognition and Avoidance," *Radiographics*, volume 24, number 6, pages 1679–1691, 2004.

[18] E. Meyer, R. Raupach, M. Lell, B. Schmidt, and M. Kachelrieß, "Normalized Metal Artifact Reduction (NMAR) in Computed Tomography," *Med. Phys.*, volume 37, number 10, pages 5482–5493, 2010.

[19] E. Meyer, R. Raupach, M. Lell, B. Schmidt, and M. Kachelrieß, "Frequency Split Metal Artifact Reduction (FSMAR) in Computed Tomography," *Med. Phys.*, volume 39, number 4, pages 1904–1916, 2012.

[20] A. Byl, L. Klein, S. Sawall, S. Heinze, H.-P. Schlemmer, and M. Kachelrieß, "Photon Counting Normalized Metal Artifact Reduction (NMAR) in Diagnostic CT," *Med. Phys.*, 2021.

[21] J. Maier, C. Leinweber, S. Sawall, H. Stoschus, F. Ballach, T. Müller, M. Hammer, R. Christoph, and M. Kachelrieß, "Simulation–Based Artifact Correction (SBAC) for Metrological Computed Tomography," *Measurement Science and Technology*, volume 28, number 6, page 065 011, 2017.

[22] K. Schörner, M. Goldammer, and J. Stephan, "Comparison Between Beam–Stop and Beam–Hole Array Scatter Correction Techniques for Industrial X–ray Cone–Beam CT," *Nuclear Instruments and Methods in Physics Research Section B: Beam Interactions with Materials and Atoms*, volume 269, number 3, pages 292–299, 2011.

[23] T. Sellerer, S. Ehn, K. Mechlem, M. Duda, M. Epple, P. B. Noël, and F. Pfeiffer, "Quantitative Dual–Energy Micro–CT with a Photon–Counting Detector for Material Science and Non–Destructive Testing," *Plos one*, volume 14, number 7, e0219659, 2019.

[24] D. Schumacher, R. Sharma, J.-C. Grager, and M. Schrapp, "Scatter and Beam Hardening Reduction in Industrial Computed Tomography Using Photon Counting Detectors," *Measurement Science and Technology*, volume 29, number 7, page 075 101, 2018.

[25] Y. Zhao and M. Li, "Iterative Beam Hardening Correction for Multi–Material Objects," *PloS one*, volume 10, number 12, e0144607, 2015.

[26] L. Brabant, E. Pauwels, M. Dierick, D. Van Loo, M. Boone, and L. Van Hoorebeke, "A Novel Beam Hardening Correction Method Requiring no Prior Knowledge, Incorporated in an Iterative Reconstruction Algorithm," *Ndt & E International*, volume 51, pages 68–73, 2012.

[27] J. Maier, S. Sawall, M. Knaup, and M. Kachelrieß, "Deep Scatter Estimation (DSE): Accurate Real–Time Scatter Estimation for X–Ray CT Using a Deep Convolutional Neural Network," *Journal of Nondestructive Evaluation*, volume 37, number 3, pages 1–9, 2018.

[28] M. Baer and M. Kachelrieß, "Hybrid Scatter Correction for CT Imaging," *Phys. Med. Biol.*, volume 57, number 21, page 6849, 2012.

[29] A. Kostenko, V. Andriiashen, and K. J. Batenburg, "Registration–Based Multi–Orientation Tomography," *Optics Express*, volume 26, number 22, pages 28 982–28 995, 2018.

[30] A. Fischer, T. Lasser, M. Schrapp, J. Stephan, and P. B. Noël, "Object Specific Trajectory Optimization for Industrial X–Ray Computed Tomography," *Scientific reports*, volume 6, number 1, pages 1–9, 2016.

[31] N. Bhatia, D. Tisseur, F. Buyens, and J. M. Létang, "Scattering Correction Using Continuously Thickness–Adapted Kernels," *NDT & E International*, volume 78, pages 52–60, 2016.

[32] H. Gao, L. Zhang, Z. Chen, Y. Xing, and S. Li, "Beam Hardening Correction for Middle–Energy Industrial Computerized Tomography," *IEEE Transactions on Nuclear Science*, volume 53, number 5, pages 2796–2807, 2006.

[33] M. Krumm, S. Kasperl, and M. Franz, "Reducing Non–Linear Artifacts of Multi–Material Objects in Industrial 3D Computed Tomography," *Ndt & E International*, volume 41, number 4, pages 242–251, 2008.

[34] A. Colijn, W. Zbijewski, A. Sasov, and F. Beekman, "Experimental Validation of a Rapid Monte Carlo Based Micro–CT Simulator," *Phys. Med. Biol.*, volume 49, number 18, page 4321, 2004.

[35] G. Jarry, S. A. Graham, D. J. Moseley, D. J. Jaffray, J. H. Siewerdsen, and F. Verhaegen, "Characterization of Scattered Radiation in kV CBCT Images Using Monte Carlo Simulations," *Med. Phys.*, volume 33, number 11, pages 4320–4329, 2006.

[36] G. Poludniowski, P. Evans, V. Hansen, and S. Webb, "An Efficient Monte Carlo–Based Algorithm for Scatter Correction in keV Cone–Beam CT," *Phys. Med. Biol.*, volume 54, number 12, page 3847, 2009.

[37] Y. Kyriakou, T. Riedel, and W. A. Kalender, "Combining Deterministic and Monte Carlo Calculations for Fast Estimation of Scatter Intensities in CT," *Phys. Med. Biol.*, volume 51, number 18, page 4567, 2006.

[38] P. G. Watson, E. Mainegra-Hing, N. Tomic, and J. Seuntjens, "Implementation of an Efficient Monte Carlo Calculation for CBCT Scatter Correction: Phantom Study," *Journal of Applied Clinical Medical Physics*, volume 16, number 4, pages 216–227, 2015.

[39] A. Maslowski, A. Wang, M. Sun, T. Wareing, I. Davis, and J. Star–Lack, "Acuros CTS: A Fast, Linear Boltzmann Transport Equation Solver for Computed Tomography Scatter–Part I: Core Algorithms and Validation," *Med. Phys.*, volume 45, number 5, pages 1899–1913, 2018.

[40] A. Wang, A. Maslowski, P. Messmer, M. Lehmann, A. Strzelecki, E. Yu, P. Paysan, M. Brehm, P. Munro, J. Star–Lack, *et al.*, "Acuros CTS: A Fast, Linear Boltzmann Transport Equation Solver for Computed Tomography Scatter–Part II: System Modeling, Scatter Correction, and Optimization," *Med. Phys.*, volume 45, number 5, pages 1914–1925, 2018.

[41] J. Maier, E. Eulig, T. Vöth, M. Knaup, J. Kuntz, S. Sawall, and M. Kachelrieß, "Real–Time Scatter Estimation for Medical CT Using the Deep Scatter Estimation: Method and Robustness Analysis with Respect to Different Anatomies, Dose Levels, Tube Voltages, and Data Truncation," *Med. Phys.*, volume 46, number 1, pages 238–249, 2019.

[42] Y. Wang, R. Zhang, K. Chen, and Y. Tian, "Scatter Distribution Estimated and Corrected by Using Convolutional Neural Network for Multi–Slice CT System," *SPIE Medical Imaging Proc.*, volume 11595, page 115950L, 2021.

[43] P. Roser, A. Birkhold, A. Preuhs, C. Syben, L. Felsner, E. Hoppe, N. Strobel, M. Korwarschik, R. Fahrig, and A. Maier, "X–Ray Scatter Estimation Using Deep Splines," *arXiv preprint arXiv:2101.09177*, 2021.

[44] G. Landry, D. Hansen, F. Kamp, M. Li, B. Hoyle, J. Weller, K. Parodi, C. Belka, and C. Kurz, "Comparing Unet Training with Three Different Datasets to Correct CBCT Images for Prostate Radiotherapy Dose Calculations," *Phys. Med. Biol.*, volume 64, number 3, page 035 011, 2019.

[45] Y. Nomura, Q. Xu, H. Shirato, S. Shimizu, and L. Xing, "Projection–Domain Scatter Correction for Cone Beam Computed Tomography Using a Residual Convolutional Neural Network," *Med. Phys.*, volume 46, number 7, pages 3142–3155, 2019.

[46] S. Xie, C. Yang, Z. Zhang, and H. Li, "Scatter Artifacts Removal Using Learning–Based Method for CBCT in IGRT System," *IEEE Access*, volume 6, pages 78 031–78 037, 2018.

[47] C. Kurz, M. Maspero, M. H. Savenije, G. Landry, F. Kamp, M. Pinto, M. Li, K. Parodi, C. Belka, and C. A. Van den Berg, "CBCT Correction Using a Cycle-Consistent Generative Adversarial Network and Unpaired Training to Enable Photon and Proton Dose Calculation," *Phys. Med. Biol.*, volume 64, number 22, page 225 004, 2019.

[48] Y. Berker, J. Maier, and M. Kachelrieß, "Deep Scatter Estimation in PET: Fast Scatter Correction Using a Convolutional Neural Network," *IEEE Medical Imaging Conference Program*, pages 1–5, 2018.

[49] J. Harms, Y. Lei, T. Wang, R. Zhang, J. Zhou, X. Tang, W. J. Curran, T. Liu, and X. Yang, "Paired Cycle–GAN–Based Image Correction for Quantitative Cone–Beam Computed Tomography," *Med. Phys.*, volume 46, number 9, pages 3998–4009, 2019.

[50] D. C. Hansen, G. Landry, F. Kamp, M. Li, C. Belka, K. Parodi, and C. Kurz, "ScatterNet: a Convolutional Neural Network for Cone–Beam CT Intensity Correction," *Med. Phys.*, volume 45, number 11, pages 4916–4926, 2018.

[51] M. M. Lell and M. Kachelrieß, "Recent and Upcoming Technological Developments in Computed Tomography: High Speed, Low Dose, Deep Learning, Multienergy," *Investigative Radiology*, volume 55, number 1, pages 8–19, 2020.

[52] N. Waltrich, S. Sawall, J. Maier, J. Kuntz, K. Stannigel, K. Lindenberg, and M. Kachelrieß, "Effect of Detruncation on the Accuracy of Monte Carlo–Based Scatter Estimation in Truncated CBCT," *Med. Phys.*, volume 45, number 8, pages 3574–3590, 2018.

[53] Y. Kyriakou and W. Kalender, "Efficiency of Antiscatter Grids for Flat–Detector CT," *Phys. Med. Biol.*, volume 52, number 20, pages 6275–6293, 2007.

[54] J. Wiegert, M. Bertram, D. Schaefer, N. Conrads, J. Timmer, T. Aach, and G. Rose, "Performance of Standard Fluoroscopy Antiscatter Grids in Flat–Detector–Based Cone–Beam CT," *SPIE Medical Imaging Proc.*, volume 5368, pages 67–78, 2004.

[55] J. H. Siewerdsen, D. Moseley, B. Bakhtiar, S. Richard, and D. A. Jaffray, "The Influence of Antiscatter Grids on Soft–Tissue Detectability in Cone–Beam Computed Tomography with Flat–Panel Detectors: Antiscatter Grids in Cone–Beam CT," *Med. Phys.*, volume 31, number 12, pages 3506–3520, 2004.

[56] S. Schafer, J. Stayman, W. Zbijewski, C. Schmidgunst, G. Kleinszig, and J. Siewerdsen, "Antiscatter Grids in Mobile C–Arm Cone–Beam CT: Effect on Image Quality and Dose," *Med. Phys.*, volume 39, number 1, pages 153–159, 2012.

[57] A. Coleman and M. Sinclair, "A Beam–Hardening Correction Using Dual–Energy Computed Tomography," *Phys. Med. Biol.*, volume 30, number 11, page 1251, 1985.

[58] S. Kuchenbecker, S. Faby, S. Sawall, M. Lell, and M. Kachelrieß, "Dual Energy CT: How Well Can Pseudo–Monochromatic Imaging Reduce Metal Artifacts?" *Med. Phys.*, volume 42, number 2, pages 1023–1036, 2015.

[59] S. Kuchenbecker, "Zweispektrencomputertomographie zur Artefaktkorrektur und Materialquantifizierung," Ph.D. dissertation, Ruprecht-Karls-Universität Heidelberg, 2015.

[60] L. Klein, S. Dorn, C. Amato, S. Heinze, M. Uhrig, H.-P. Schlemmer, M. Kachelrieß, and S. Sawall, "Effects of Detector Sampling on Noise Reduction in Clinical Photon–Counting Whole–Body Computed Tomography," *Investigative Radiology*, volume 55, number 2, pages 111–119, 2020.

[61] C. Amato, L. Klein, E. Wehrse, L. T. Rotkopf, S. Sawall, J. Maier, C. H. Ziener, H.-P. Schlemmer, and M. Kachelrieß, "Potential of Contrast Agents Based on High–Z Elements for Contrast–Enhanced Photon–Counting Computed Tomography," *Med. Phys.*, volume 47, number 12, pages 6179–6190, 2020.

[62] K. Taguchi and J. S. Iwanczyk, "Vision 20/20: Single Photon Counting X–Ray Detectors in Medical Imaging," *Med. Phys.*, volume 40, number 10, page 100 901, 2013.

[63] H. Yang, K. Kim, G. El Fakhri, K. Kang, Y. Xing, and Q. Li, "Dual–Energy CT Reconstruction Using Guided Image Filtering," in *2016 IEEE Nuclear Science Symposium, Medical Imaging Conference and Room-Temperature Semiconductor Detector Workshop (NSS/MIC/RTSD)*, IEEE, 2016, pages 1–4.

[64] C. Cheung, B. Yang, C. Kong, K. Cheung, S. Yu, *et al.*, "Joint Bilateral Filtering for Dual Energy Computed Tomography – A Phantom Study," European Congress of Radiology-ECR 2017, 2017.

[65] M. Manhart, R. Fahrig, J. Hornegger, A. Doerfler, and A. Maier, "Guided Noise Reduction for Spectral CT with Energy–Selective Photon Counting Detectors," in *Proceedings of the Third CT Meeting*, 2014, pages 91–94.

[66] Y. Lu, M. Manhart, O. Taubmann, T. Zobel, Q. Yang, J.-h. Choi, M. Wu, A. Doerfler, R. Fahrig, Q. Ren, *et al.*, "Projection–Based Denoising Method for Photon–Counting Energy–Resolving Detectors," in *Bildverarbeitung für die Medizin 2015*, Springer, 2015, pages 137–142.

[67] Z. Li, S. Leng, L. Yu, A. Manduca, and C. H. McCollough, "An Effective Noise Reduction Method for Multi–Energy CT Images that Exploit Spatio–Spectral Features," *Med. Phys.*, volume 44, number 5, pages 1610–1623, 2017.

[68] K. Müller, M. Ahmad, M. Spahn, J.-H. Choi, S. Reitz, N. Köster, Y. Lu, R. Fahrig, and A. Maier, "Towards Material Decomposition on Large Field–Of–View Flat Panel Photon–Counting Detectors–First In–Vivo Results," in *Proceedings of The Fourth International Conference on Image Formation in X-Ray Computed Tomography*, 2016, pages 479–482.

[69] K. Nikolaou, F. Bamberg, A. Laghi, and G. D. Rubin, *Multislice CT*. Springer, 2019.

[70] O. Brunke, J. Lübbehüsen, F. Hansen, and F. F. Butz, "A new Concept for High-Speed atline and inlineCT for up to 100% Mass Production Process Control," in *16th International Congress of Metrology*, EDP Sciences, 2013, page 06 003.

[71] B. Szallies, *Physik 2 Kurz & Klar*. Auer, 2002.

[72] W. Demtröder, *Experimentalphysik 3 Atome, Moleküle und Festkörper*. Springer, 2010.

[73] H. A. Kramers, "On the Theory of X–ray Absorption and of the Continuous X–Ray Spectrum," *Philosophical Magazine Series 1*, volume 46, number 6, 1923.

[74] C. Fiori, R. Myklebust, K. Heinrich, and H. Yakowitz, "Prediction of Continuum Intensity in Energy–Dispersive X–Ray Microanalysis," *Analytical Chemistry*, volume 48, number 1, pages 172–176, 1976.

[75] H. Krieger, *Strahlungsquellen für Technik und Medizin*. Springer, 2013.

[76] E. Lassner and W. D. Schubert, *Tungsten: Properties, Chemistry, Technology of the Element, Alloys, and Chemical Compounds*. Springer, 1999.

[77] H. Braun, Y. Kyriakou, M. Kachelriess, and W. Kalender, "The Influence of the Heel Effect in Cone–Beam Computed Tomography: Artifacts in Standard and Novel Geometries and their Correction," *Phys. Med. Biol.*, volume 55, number 19, page 6005, 2010.

[78] M. Wang, *Industrial Tomography: Systems and Applications*. Woodhead Publishing Ltd, 2015.

[79] M. Mildner and K. Holm, "Modulare Röntgenröre und Verfahren zu ihrer Herstellung," 1 714 298, EP 1714298, 2003.

[80] D. V. Gopinath and N. Ramamoorthy, *Ionising Radiation and Mankind*. Springer, 2020.

[81] D. M. Tucker, G. T. Barnes, and D. P. Chakraborty, "Semiempirical Model for Generating Tungsten Target X–Ray Spectra," *Med. Phys.*, volume 18, number 2, pages 211–218, 1991.

[82] M. Kachelriess, M. Knaup, C. Penssel, and W. Kalender, "Flying Focal Spot (FFS) in Cone–Beam CT," *IEEE Transactions on Nuclear Science*, volume 53, number 3, pages 1238–1247, 2006.

[83] Y. Kyriakou, M. Kachelrieß, M. Knaup, J. U. Krause, and W. A. Kalender, "Impact of the z–Flying Focal Spot on Resolution and Artifact Behavior for a 64–Slice Spiral CT Scanner," *European Radiology*, volume 16, number 6, pages 1206–1215, 2006.

[84] M. Engelhardt, "Neue Verfahren in der Mikrofokus-Röntgen Radiographie und Computertomographie: Phasenkontrastbildgebung und Abbildung der Brennfleckintensitätsverteilung," Ph.D. dissertation, Technische Universität München, 2008.

[85] X.-R. W. GmbH. “Mikrofokus röntgenröhren – technologie.” (2021), [Online]. Available: https://www.x-ray-worx.com/index.php/mikrofokus-roentgenroehren-produktuebersicht/mikrofokus-technologie (visited on 11/19/2021).

[86] P. Kandlakunta, A. Thomas, Y. Tan, R. Khan, and T. Zhang, “Design and Numerical Simulations of W–Diamond Transmission Target for Distributed X–Ray Sources,” *Biomedical Physics & Engineering Express*, volume 5, number 2, page 025 030, 2019.

[87] W. Demtröder, *Experimentalphysik 2 Elektrizität und Optik*. Springer, 1999.

[88] J. Heintze, *Lehrbuch zur Experimentalphysik Band 5: Quantenphysik: Wellen, Teilchen und Atome*. Springer, 2019.

[89] W. Demtröder, *Experimentalphysik 4 Kern-, Teilchen- und Astrophysik*. Springer, 2010.

[90] W. Heitler, *The Quantum Theory of Radiation: Third Edition*. Dover Publications, Inc., 1984.

[91] O. Klein and Y. Nishina, “Über die Streuung von Strahlung durch freie Elektronen nach der neuen relativistischen Quantendynamik von Dirac,” *Zeitschrift für Physik*, volume 52, number 11, pages 853–868, 1929.

[92] J. Cunnningham and D. Dance, *Chapter 2: Interactions of Radiation with Matter. In Diagnostic Radiology Physics*. International Atomic Energy Agency, 2014.

[93] E. Hussein, *Radiation Mechanics: Principles and Practice*. Elsevier Science, 2007.

[94] M. Baer, “CT Scatter Simulation and CT Scatter Reduction Methods,” Ph.D. dissertation, Friedrich-Alexander-Universität (FAU) Erlangen-Nürnberg, 2012.

[95] D. E. Cullen, J. H. Hubbell, and L. Kissel, “EPDL97: the Evaluated Photo Data Library ’97 Version,” 1997.

[96] H. Krieger, *Strahlungsmessung und Dosimetrie*. Springer Spektrum, 2013.

[97] J. Maier, “Artifact Correction and Real–Time Scatter Estimation for X–Ray Computed Tomography in Industrial Metrology,” Ph.D. dissertation, Combined Faculties for the Natural Sciences and for Mathematics of the Ruperto–Carola University of Heidelberg, 2019, page 171.

[98] J. Rowlands and U. Neitzel, *Chapter 7: Receptors for Projection Radiography. In Diagnostic Radiology Physics*. International Atomic Energy Agency, 2014.

[99] M. Nikl, “Scintillation detectors for X–Rays,” *Measurement Science and Technology*, volume 17, number 4, R37–R54, 2006.

[100] C. Szeles, S. A. Soldner, S. Vydrin, J. Graves, and D. S. Bale, “CdZnTe Semiconductor Detectors for Spectroscopic X–Ray Imaging,” *IEEE Transactions on Nuclear Science*, volume 55, number 1, pages 572–582, 2008.

[101] P. Capper, *Properties of Narrow Gap Cadmium–Based Compounds*. Iet, 1994.

[102] S. Faby, J. Maier, S. Sawall, D. Simons, H.-P. Schlemmer, M. Lell, and M. Kachelrieß, "An Efficient Computational Approach to Model Statistical Correlations in Photon Counting X–Ray Detectors," *Med. Phys.*, volume 43, number 7, pages 3945–3960, 2016.

[103] S. Kappler, T. Hannemann, E. Kraft, B. Kreisler, D. Niederloehner, K. Stierstorfer, and T. Flohr, "First Results From a Hybrid Prototype CT Scanner for Exploring Benefits of Quantum–Counting in Clinical CT," *SPIE Medical Imaging Proc.*, volume 8313, page 83130X, 2012.

[104] C. Xu, M. Danielsson, and H. Bornefalk, "Evaluation of Energy Loss and Charge Sharing in Cadmium Telluride Detectors for Photon–Counting Computed Tomography," *IEEE Transactions on Nuclear Science*, volume 58, number 3, pages 614–625, 2011.

[105] T. Koenig, E. Hamann, S. Procz, R. Ballabriga, A. Cecilia, M. Zuber, X. Llopart, M. Campbell, A. Fauler, T. Baumbach, *et al.*, "Charge Summing in Spectroscopic X–Ray Detectors with High–Z Sensors," *IEEE Transactions on Nuclear Science*, volume 60, number 6, pages 4713–4718, 2013.

[106] W. A. Kalender, *Computed Tomography: Fundamentals, System Technology, Image Quality, Applications*. John Wiley & Sons, 2011.

[107] H. Turbell, "Cone–Beam Reconstruction Using Filtered Backprojection," Ph.D. dissertation, Linköpings universitet, 2001.

[108] J. Wiegert, "Scattered Radiation in Cone–Beam Computed Tomography: Analysis, Quantification and Compensation," Ph.D. dissertation, Rheinisch-Westfälische Technische Hochschule Aachen, 2007.

[109] H. K. Tuy, "An Inversion Formula for Cone–Beam Reconstruction," *SIAM Journal on Applied Mathematics*, volume 43, number 3, pages 546–552, 1983.

[110] H. Handels, *Medizinische Bildverarbeitung: Bildanalyse, Mustererkennung und Visualisierung für die computergestützte ärztliche Diagnostik und Therapie*. Vieweg und Teubner, 2009.

[111] H. Horn and J. Kosche, "Segmentierung von Bilddaten," *Seminarvortrag, Institut für Informationsverarbeitung und Kommunikation, Universität Potsdam*, 2004.

[112] N. Otsu, "A Threshold Selection Method from Gray–Level Histograms," *IEEE Transactions on Systems, Man, and Cybernetics*, volume 9, number 1, pages 62–66, 1979.

[113] S. Beucher and F. Meyer, "The Morphological Approach to Segmentation: the Watershed Transformation," in *Mathematical morphology in image processing*, CRC Press, 2018, pages 433–481.

[114] O. Ronneberger, P. Fischer, and T. Brox, "U–Net: Convolutional Networks for Biomedical Image Segmentation," in *International Conference on Medical image computing and computer-assisted intervention*, Springer, 2015, pages 234–241.

[115] S. Chen, X. Zhong, S. Hu, S. Dorn, M. Kachelrieß, M. Lell, and A. Maier, "Automatic Multi–Organ Segmentation in Dual–Energy CT (DECT) with Dedicated 3D Fully Convolutional DECT Networks," *Med. Phys.*, volume 47, number 2, pages 552–562, 2020.

[116] Y. Lei, Y. Fu, T. Wang, R. L. Qiu, W. J. Curran, T. Liu, and X. Yang, "Deep Learning in Multi–Organ Segmentation," *arXiv preprint arXiv:2001.10619*, 2020.

[117] H. Watanabe, Y. Ariji, M. Fukuda, C. Kuwada, Y. Kise, M. Nozawa, Y. Sugita, and E. Ariji, "Deep Learning Object Detection of Maxillary Cyst–Like Lesions on Panoramic Radiographs: Preliminary Study," *Oral Radiology*, pages 1–7, 2020.

[118] H.-G. Woschni, R. Christoph, and A. Reinsch, "Verfahren zur Bestimmung der Lage einer optisch wirksamen Struktur," *Feingerätetechnik*, volume 33, number 5, 1984.

[119] R. Christoph and H. J. Neumann, *Multisensor–Koordinatenmesstechnik*. Verlag moderne Industrie, 2006.

[120] W. E. Lorensen and H. E. Cline, "Marching Cubes: A High Resolution 3D Surface Construction Algorithm," *ACM SIGGRAPH Computer Graphics*, volume 21, number 4, pages 163–169, 1987.

[121] J. Stopp, R. Christoph, and H. Weise, "Surface Point Determination in Subvoxel Accuracy from Pre–Segmented Multi-Material Volume Data for Metrological Applications," in *10th Conference on Industrial Computed Tomography, Wels, Austria (iCT 2020)*, 2020.

[122] E. Hering and R. Martin, *Optik für Ingenieure und Naturwissenschaftler: Grundlagen und Anwendungen*. Carl Hanser Verlag GmbH Co KG, 2017.

[123] C. B. Claus P. Keferstein Michael Marxer, *Fertigungsmesstechnik: Alles zu Messunsicherheit, konventioneller Messtechnik und Multisensorik*. Springer Vieweg, 2018.

[124] D. G. für Qualität. "Iso-gps: Tolerierungsgrundsätze." (2021), [Online]. Available: `https://www.dgq.de/fachbeitraege/iso-gps-tolerierungsgrundsaetze/` (visited on 12/16/2021).

[125] G. D. Boreman, *Modulation Transfer Function in Optical and Electro-optical Systems*. SPIE press Bellingham, Washington, 2001.

[126] J. M. Blackledge, *Chapter 11 - Optical Image Formation. In Digital Image Processing: Mathematical and Computational Methods*. Woodhead Publishing, 2005.

[127] J. Hiller, M. Maisl, and L. M. Reindl, "Physical Characterization and Performance Evaluation of an X–Ray Micro–Computed Tomography System for Dimensional Metrology Applications," *Measurement Science and Technology*, volume 23, number 8, page 085 404, 2012.

[128] G. Ramachandran and A. Lakshminarayanan, "Three–Dimensional Reconstruction From Radiographs and Electron Micrographs: Application of Convolutions Instead of Fourier Transforms," *Proceedings of the National Academy of Sciences*, volume 68, number 9, pages 2236–2240, 1971.

[129] C. Leinweber, "Untersuchung der spektralen und abbildenden Eigenschaften von Röntgen-Computertomographie-Systemen für die Koordinatenmesstechnik," Ph.D. dissertation, Ruprecht-Karls-Universität Heidelberg, 2018.

[130] Z. Yu, S. Leng, S. Kappler, K. Hahn, Z. Li, A. F. Halaweish, A. Henning, and C. H. McCollough, "Noise Performance of Low–Dose CT: Comparison Between an Energy Integrating Detector and a Photon Counting Detector Using a Whole–Body Research Photon Counting CT Scanner," *Journal of Medical Imaging*, volume 3, number 4, page 043 503, 2016.

[131] A. T. Tao, D. Miller, M. Hindal, and K. A. Fetterly, "Assessment of Scatter Originating from the X–Ray Tube Collimator Assembly of Modern Angiography Systems," *Med. Phys.*, volume 46, number 10, pages 4371–4380, 2019.

[132] Y. Wang, K. Stierstorfer, M. Petersilka, and Y. Tian, "Improved Wedge Scatter Correction for Multi–Slice CT System," in *SPIE Medical Imaging Proc.*, T. G. Schmidt, G.-H. Chen, and H. Bosmans, Eds., International Society for Optics and Photonics, volume 10948, SPIE, 2019, pages 586–592.

[133] A. Miceli, R. Thierry, A. Flisch, U. Sennhauser, F. Casali, and M. Simon, "Monte Carlo Simulations of a High–Resolution X–Ray CT System for Industrial Applications," *Nuclear Instruments and Methods in Physics Research Section A: Accelerators, Spectrometers, Detectors and Associated Equipment*, volume 583, number 2-3, pages 313–323, 2007.

[134] R. E. Alvarez and A. Macovski, "Energy–Selective Reconstructions in X–Ray Computerised Tomography," *Phys. Med. Biol.*, volume 21, number 5, page 733, 1976.

[135] L. Lehmann, R. Alvarez, A. Macovski, W. Brody, N. Pelc, S. J. Riederer, and A. Hall, "Generalized Image Combinations in Dual kVp Digital Radiography," *Med. Phys.*, volume 8, number 5, pages 659–667, 1981.

[136] N. Maaß, S. Sawall, M. Knaup, and M. Kachelrieß, "Empirical Multiple Energy Calibration (EMEC) for Material–Selective CT," in *2011 IEEE Nuclear Science Symposium Conference Record*, IEEE, 2011, pages 4222–4229.

[137] L. Yu, A. N. Primak, X. Liu, and C. H. McCollough, "Image Quality Optimization and Evaluation of Linearly Mixed Images in Dual–Source, Dual–Energy CT," *Med. Phys.*, volume 36, number 3, pages 1019–1024, 2009.

[138] L. Yu, S. Leng, and C. H. McCollough, "Dual–Energy CT–Based Monochromatic Imaging," *American journal of Roentgenology*, volume 199, number 5_supplement, S9–S15, 2012.

[139] A. Primak, J. Ramirez Giraldo, X. Liu, L. Yu, and C. H. McCollough, "Improved Dual–Energy Material Discrimination for Dual–Source CT by Means of Additional Spectral Filtration," *Med. Phys.*, volume 36, number 4, pages 1359–1369, 2009.

[140] J. Nelder and R. Mead, "A Simplex Method for Function Minimization," *Computer Journal*, volume 7, number 4, pages 308–313, 1965.

[141] S. Strandberg, M.-L. Wretling, T. Wredmark, and A. Shalabi, "Reliability of Computed Tomography Measurements in Assessment of Thigh Muscle Cross-sectional Area and Attenuation," *BMC Medical Imaging*, volume 10, number 1, pages 1–8, 2010.

[142] L. A. Love and R. A. Kruger, "Scatter Estimation for a Digital Radiographic System Using Convolution Filtering," *Med. Phys.*, volume 14, number 2, pages 178–185, 1987.

[143] J. A. Seibert and J. M. Boone, "X–Ray Scatter Removal by Deconvolution," *Med. Phys.*, volume 15, number 4, pages 567–575, 1988.

[144] B. Ohnesorge, T. Flohr, and K. Klingenbeck–Regn, "Efficient Object Scatter Correction Algorithm for Third and Fourth Generation CT Scanners," *European Radiology*, volume 9, pages 563–569, 1999.

[145] M. Kachelrieß, "Reduktion von Metallartefakten in der Röntgen–Computer–Tomographie," Ph.D. thesis, Friedrich–Alexander–Universität Erlangen–Nürnberg, 1998.

[146] J. Rinkel, L. Gerfault, F. Esteve, and J. Dinten, "A New Method for X–Ray Scatter Correction: First Assessment on a Cone–Beam CT Experimental Setup," *Phys. Med. Biol.*, volume 52, number 15, page 4633, 2007.

[147] H. Li, R. Mohan, and X. R. Zhu, "Scatter Kernel Estimation with an Edge–Spread Function Method for Cone–Beam Computed Tomography Imaging," *Phys. Med. Biol.*, volume 53, number 23, page 6729, 2008.

[148] J. Star–Lack, M. Sun, A. Kaestner, R. Hassanein, G. Virshup, T. Berkus, and M. Oelhafen, "Efficient Scatter Correction Using Asymmetric Kernels," *SPIE Medical Imaging Proc.*, volume 7258, 72581Z, 2009.

[149] M. Meyer, W. A. Kalender, and Y. Kyriakou, "A Fast and Pragmatic Approach for Scatter Correction in Flat–Detector CT Using Elliptic Modeling and Iterative Optimization," *Phys. Med. Biol.*, volume 55, number 1, page 99, 2009.

[150] M. Baer, "CT Scatter Simulation and CT Scatter Reduction Methods," Ph.D. dissertation, Medical Faculty of the Friedrich–Alexander–University (FAU) Erlangen–Nürnberg, 2012, page 115.

[151] E. Meyer, C. Maaß, M. Baer, R. Raupach, B. Schmidt, and M. Kachelrieß, "Empirical Scatter Correction (ESC): A New CT Scatter Correction Method and Its Application to Metal Artifact Reduction," *IEEE Medical Imaging Conference Record*, pages 2036–2041, 2010.

[152] M. Salmi, J. Tuomi, K.-S. Paloheimo, R. Björkstrand, M. Paloheimo, J. Salo, R. Kontio, K. Mesimäki, and A. A. Mäkitie, "Patient–Specific Reconstruction with 3D Modeling and DMLS Additive Manufacturing," *Rapid Prototyping Journal*, volume 18, number 3, 2012.

[153] M. Sun and J. M. Star-Lack, "Improved Scatter Correction Using Adaptive Scatter Kernel Superposition," *Phys. Med. Biol.*, volume 55, number 22, page 6695, 2010.

[154] Y. Kyriakou, E. Meyer, D. Prell, and M. Kachelrieß, "Empirical Beam Hardening Correction (EBHC) for CT," *Med. Phys.*, volume 37, number 2, pages 5179–5187, 2015.

[155] S. Schüller, S. Sawall, K. Stannigel, M. Hülsbusch, J. Ulrici, E. Hell, and M. Kachelrieß, "Segmentation–Free Empirical Beam Hardening Correction for CT," *Med. Phys.*, volume 42, number 2, pages 794–803, 2015.

[156] G. Di Domenico, P. Cardarelli, A. Contillo, A. Taibi, and M. Gambaccini, "X–Ray Focal Spot Reconstruction by Circular Penumbra Analysis–Application to Digital Radiography Systems," *Med. Phys.*, volume 43, number 1, pages 294–302, 2016.

[157] L. Shi, N. R. Bennett, and A. S. Wang, "Reconstruction of X–Ray Focal Spot Distribution Using a Rotating Edge," volume 11312, 2020, page 113122M.

[158] B. van der Heyden, G. P. Fonseca, M. Podesta, I. Messner, N. Reisz, A. Vaniqui, H. Deutschmann, P. Steininger, and F. Verhaegen, "Modelling of the Focal Spot Intensity Distribution and the Off–Focal Spot Radiation in Kilovoltage X–Ray Tubes for Imaging," *Phys. Med. Biol.*, volume 65, number 2, page 025 002, 2020.

[159] G. Probst, W. Dewulf, Q. Hou, R. Pauwels, G. Probst, and Y. Xiao, "Focal Spot Characterization of an Industrial X–Ray CT Scanner," in *Proceedings of the International Symposium on Digital Industrial Radiology and Computed Tomography*, 2019, page 10.

[160] C. Altunbas, B. Kavanagh, T. Alexeev, and M. Miften, "Transmission Characteristics of a Two Dimensional Antiscatter Grid Prototype for CBCT," *Med. Phys.*, volume 44, number 8, pages 3952–3964, 2017.

[161] T. Alexeev, B. Kavanagh, M. Miften, and C. Altunbas, "Two–Dimensional Antiscatter Grid: A Novel Scatter Rejection Device for Cone–Beam Computed Tomography," *Med. Phys.*, volume 45, number 2, pages 529–534, 2018.

[162] R. Christoph, C. Leinweber, A. Fischer, H. Weise, and M. Kachelrieß, "Validation of a Method for the Optimization of Scan Parameters for Measuring with Computed Tomography," in *9th Conference on Industrial Computed Tomography, Padova, Italy (iCT 2019))*, 2019.

[163] R. Christoph, "Automatische Bestimmung von Einstellparametern für die Koordinatenmessung mittels Röntgentomografie," Ph.D. dissertation, Technische Universität Dresden, 2021.

[164] S. Faby, S. Kuchenbecker, S. Sawall, D. Simons, H.-P. Schlemmer, M. Lell, and M. Kachelrieß, "Performance of Today's Dual Energy CT and Future Multi Energy CT in Virtual Non–Contrast Imaging and in Iodine Quantification: a Simulation Study," *Med. Phys.*, volume 42, number 7, pages 4349–4366, 2015.

[165] R. K. Swank, "Absorption and Noise in X–Ray Phosphors," *Journal of Applied Physics*, volume 44, number 9, pages 4199–4203, 1973.

[166] R. K. Swank, "Measurement of Absorption and Noise in an X–Ray Image Intensifier," *Journal of Applied Physics*, volume 45, number 8, pages 3673–3678, 1974.

[167] M. Lu, A. Wang, E. Shapiro, A. Shiroma, J. Zhang, J. Steiger, and J. Star-Lack, "Dual Energy Imaging with a Dual–Layer Flat Panel Detector," in *SPIE Medical Imaging Proc.*, International Society for Optics and Photonics, volume 10948, 2019, page 1 094 815.

[168] D. C. AB. "Xc-thor." (2021), [Online]. Available: `https://directconversion.com/product/xc-thor/` (visited on 12/09/2021).

[169] W. Zhou, D. J. Bartlett, F. E. Diehn, K. N. Glazebrook, A. L. Kotsenas, R. E. Carter, J. G. Fletcher, C. H. McCollough, and S. Leng, "Reduction of Metal Artifacts and Improvement in Dose Efficiency Using Photon Counting Detector CT and Tin Filtration," *Investigative Radiology*, volume 54, number 4, page 204, 2019.

[170] P. M. Shikhaliev, "Computed Tomography with Energy–Resolved Detection: a Feasibility Study," *Phys. Med. Biol.*, volume 53, number 5, pages 5595–5613, 2008.

[171] K. L. Grant, T. G. Flohr, B. Krauss, M. Sedlmair, C. Thomas, and B. Schmidt, "Assessment of an Advanced Image-Based Technique to Calculate Virtual Monoenergetic Computed Tomographic Images from a Dual-Energy Examination to Improve Contrast-to-Noise Ratio in Examinations using Iodinated Contrast Media," *Investigative Radiology*, volume 49, number 9, pages 586–592, 2014.

[172] G. Petschnigg, R. Szeliski, M. Agrawala, M. Cohen, H. Hoppe, and K. Toyama, "Digital Photography with Flash and No-Flash Image Pairs," *ACM transactions on graphics (TOG)*, volume 23, number 3, pages 664–672, 2004.

[173] E. Eisemann and F. Durand, "Flash Photography Enhancement via Intrinsic Relighting," *ACM transactions on graphics (TOG)*, volume 23, number 3, pages 673–678, 2004.

List of publications

Parts of this thesis have been published in the following journal articles and conference contributions:

Journal Articles

[1] **P. Trapp**, J. Maier, M. Susenburger, S. Sawall, and M. Kachelrieß, "Empirical Scatter Correction (ESC): CBCT Scatter Artifact Reduction without Prior Information," *Med. Phys.*, 2022.

Conference Contributions

[1] **P. Trapp**, J. Maier, M. Susenburger, S. Sawall, and M. Kachelrieß, "Empirical Scatter Correction (ESC): a Universal Scatter Reduction Method for Cone–Beam CT (CBCT) without Prior Knowledge," in *European Congress of Radiology*, 2022.

[2] **P. Trapp**, T. Vöth, C. Amato, S. Sawall, and M. Kachelrieß, "DeepRAR: A CNN–Based Approach for CT and CBCT Ring Artifact Reduction," in *SPIE Medical Imaging Proc.*, 2022.

[3] **P. Trapp**, A. Byl, S. Heinze, H.-P. Schlemmer, S. Sawall, and M. Kachelrieß, "Bin–Combination–Based Noise Reduction for Metal Artifact Reduction in Photon Counting CT," in *European Congress of Radiology*, Winning the award for the best research presentation abstract within the topic Physics in Medical Imaging, 2021.

[4] **P. Trapp**, L. Klein, C. Amato, J. Maier, N. Brierley, R. Christoph, S. Sawall, and M. Kachelrieß, "Benefits of Photon Counting Detectors for Beam Hardening Artifact Reduction in Industrial CT Applications," in *10th Conference on Industrial Computed Tomography (iCT)*, 2020.

Patents

[1] R. Christoph, R. Christoph, H. Stoschus, C. Leinweber, **P. Trapp**, M. Hammer, D. Schröter, L. Eichner, T. Gruhl, and L. J. Stopp, "Vorrichtung und Verfahren zur computertomografischen Messung von Werkstücken mit drehbarem Targetträger," WO2019192860 A1, 2019.

[2] **P. Trapp** and others (requesting non-designation), "Einmessvorrichtung," DE 102020130442 A1, 2021.

[3] **P. Trapp** and others (requesting non-designation), "Vorrichtung und Verfahren zum Betreiben eines Computertomografen mit photonenzählendem Detektor zur Artefaktkorrektur und Messoptimierung in metrologischer Anwendung," DE 102020100913 A1, 2020.

[4] **P. Trapp** and others (requesting non-designation), "Vorrichtung und Verfahren zur computertomografischen Messung von Werkstücken," DE 102019107348 A1, 2019.

Acknowledgments

Zunächst möchte ich mich herzlich bei Prof. Dr. Peter Bachert für die Übernahme des Erstgutachtens und die Unterstützung und Beratung im Rahmen des Thesisberatungskomitees der DKFZ Graduiertenschule bedanken.
In gleichem Maße möchte ich mich bei Prof. Dr. Marc Kachelrieß für die Betreuung meiner Arbeit, die Übernahme des Zweitgutachtens und die Aufnahme in seine Arbeitsgruppe am DKFZ bedanken. Vielen Dank, Marc, für die Zeit, die du immer für mich aufbringen konntest und mir selbst bei Detailfragen helfend zur Seite standest! Deine Ideen und Vorschläge haben den Erfolg dieses Forschungsprojekts erst ermöglicht!
Ein besonderes Dankeschön auch an Dr. Ralf Christoph für die Unterstützung dieses Projekts seitens der Werth Messtechnik GmbH. Danke für Ihre intensive Betreuung dieser Arbeit und die damit verbundenen zahlreichen Besprechungen, die mich sowohl fachlich, als auch methodisch vorangebracht haben.
Vielen Dank auch an meine Kollegen am DKFZ von der Abteilung "Röntgenbildgebung und Computertomographie". Insbesondere möchte ich mich bei den Postdocs unserer Gruppe, Dr. Joscha Maier und Dr. Stefan Sawall bedanken, die mir stets mit guten Ratschlägen, Ideen und Detailwissen weitergeholfen haben. Danke, Markus, für die gute "Tischnachbarschaft" und deine Hilfe bei allen möglichen Problemen. Und natürlich für die Freundschaft, die uns hoffentlich weiterhin gemeinsam von der Neckarwiese bis ins Fußballstadion führt. Carlo, amico italiano, è un piacere conoscerti! Vielen Dank Laura, Tim und Julien, für die gute und hilfsbereite Arbeitsatmosphäre im Büro und die vielen schönen Stunden, die wir gemeinsam am Feierabend oder den Wochenenden verbringen konnten.
Des Weiteren möchte ich mich bei meinen Kollegen der Werth Messtechnik GmbH bedanken. Hier gilt mein besonderer Dank Frederic Ballach, der dieses Forschungsprojekt administriert und mir stets als Kontaktperson zur Verfügung stand, und Dr. Raoul Christoph für hilfreiche Diskussionen zum Forschungsthema. Außerdem möchte ich mich explizit bei Michael Hammer, Tobias Müller, André Machmerth und Alexander Fischer für ihre Hilfestellungen bei Softwareintegration, Messungen, Auswertungen und allgemeinen gerätebezogenen Fragen bedanken.
Danke Dr. Wolfram Stiller für die Teilnahme an meinem Thesisberatungskomitee der DKFZ Graduiertenschule und der damit verbundenen Betreuung dieses Projekts.
Danke Prof. Dr. Johanna Stachel und Prof. Dr. Tilman Plehn für die Übernahme der mündlichen Prüfung.

Außerdem möchte ich meinen Eltern und Großeltern für Ihre Unterstützung danken. Ohne eure Begleitung, insbesondere in den schwierigen Zeiten, und euren bedingungslosen Rückhalt wäre diese Arbeit nicht möglich gewesen.
Zu guter Letzt gilt mein Dank meiner Frau. Danke, Rebekka, dass du mir immer zur Seite stehst und mir so oft den Rücken freigehalten hast. Ich kann mir nicht vorstellen, wie ich diese Arbeit ohne dich zum Abschluss gebracht hätte!

Dieses Projekt wurde durch das BMBF-Förderprogramm Photonik Forschung Deutschland “KMU-innovativ: Photonik” unter dem Kennzeichen 13N14804 gefördert.

I hereby assure, that I composed this work by myself and did not use any other than the listed resources.

P. Trapp

Heidelberg, May 16, 2022